analytical chemistry

REVIEW

pubs.acs.org/ac

X-ray Spectrometry

Kouichi Tsuji* and Kazuhiko Nakano

Department of Applied Chemistry & Bioengineering, Graduate School of Engineering, Osaka City University, 3-3-138 Sugimoto, Sumiyoshi-ku, Osaka, 558-8585, Japan

Yoshio Takahashi

Department of Earth and Planetary Systems Science, Graduate School of Science, Hiroshima University, Higashi-Hiroshima, Hiroshima 739-8526, Japan

Kouichi Hayashi

Institute for Materials Research, Tohoku University, 2-1-1 Katahira, Aoba-ku, Sendai, 980-8577, Japan

Chul-Un Ro

Department of Chemistry, Inha University, 253 Yonghyun-dong, Nam-gu, Incheon, 402-751, Korea

CONTENTS

In this Review, we focus on the most significant and essential progress in X-ray spectrometry (XRS) published during the period from January 2010 to August 2011 covering developments and improvements in X-ray optics, X-ray detectors, new quantification models in X-ray spectra and data evaluation, micro-X-ray fluorescence (micro-XRF) including 3D X-ray fluorescence (3D-XRF), elemental imaging techniques, electron probe microanalysis (EPMA), total reflection X-ray fluorescence (TXRF), particle-induced X-ray emission (PIXE) analysis, and X-ray absorption spectrometry (XAS). Herein, we focus on X-ray spectrometry, and thus, X-ray radiography used for only investigating inside structure images and X-ray diffraction (XRD) is not covered. However, we will introduce articles including combinations of these X-ray imaging techniques and other spectroscopic techniques. In addition, different applications in each subfield of XRS, including sample preparation, standard materials, energy-dispersive XRF (ED-XRF), and wavelength-dispersive XRF (WD-XRF), are described. We attempt to look over the current trends in this analytical field by critically citing selected papers to support the research activity of the community of X-ray scientists.

Since the previous review on XRS in *Analytical Chemistry*, an international group of scientists published two overviews on XRS[1,2] in the *Journal of Analytical Atomic Spectrometry* covering the main fields of XRS analytical spectroscopic methods and instruments. These review articles involve all of the important sections of XRS in nine chapters: reviews, instrumentation, spectrum analysis, matrix correction and calibration, X-ray optics and micro fluorescence, synchrotron radiation (SR), TXRF, portable and mobile X-ray fluorescence (XRF), and online XRF and applications. The section on applications is categorized into geological and industrial minerals, environmental, archeological, cultural heritage, forensic science, etc. These review articles are useful, especially for an overall look at recent XRS research activities.

The second edition of the book, "*Elements of Modern X-ray Physics*", was published.[3] It provides excellent explanations of the basics of X-ray physics, interactions with matter, X-ray sources,

Special Issue: Fundamental and Applied Reviews in Analytical Chemistry

Published: November 10, 2011

refraction and reflection, diffraction, and absorption. To meet recent demands, new chapters on X-ray imaging and noncrystalline diffraction were also included. The proceedings of some international conferences in the XRS field were published. The book, *"Proceedings of the 20th International Congress on X-ray Optics and Microanalysis (ICXOM)"*, which was held in Karlsruhe, Germany, 15−18 September 2009, was published as the AIP Conference Proceedings.[4] Recent progress on X-ray optics which has been used not only for SR sources but also for laboratory X-ray tubes is included. Development of a nano-X-ray beam has been achieved, and thus, X-ray elemental microscopy is getting more attention. We read about recent developments in X-ray optics and its applications to X-ray imaging from the book of 20th ICXOM proceedings. Another publication, *"X-ray Lasers 2010: Proceeding of the 12th International Conference on X-ray Lasers,"* was published by Springer.[5] Three special issues with the proceedings for the articles presented in the European Conference on X-ray Spectrometry (EXRS) that was held in Coimbra, Portugal, in June 2010 were published in the journal *X-ray Spectrometry*.[6] In these special issues, recent advancements of detectors and optics and new developments in X-ray spectrometers are included. The proceedings of PIXE 2010, the 12th International Conference on Particle Induced X- Ray Emission and its Analytical Applications, were published as a special issue of *X-ray Spectrometry*.[7] PIXE 2010 was held in Guildford, UK, in June−July 2010. This special issue includes 22 selected papers that present PIXE research trends. Some of the papers are introduced in the PIXE subsection in this article.

One of the most active research areas in XRS is micro-XRF. Recent developments of X-ray focusing optics and X-ray detectors including two-dimensional X-ray detectors, such as X-ray charge-coupled device (CCD) cameras, enable micro-XRF and X-ray elemental imaging on micro- and nanoscales. A leading research group in this field wrote a review article on microscopic XRF analysis.[8] In the article, recent trends in micro-XRF were discussed, citing about 100 papers. After methodological improvements in spectrum-evaluation software, confocal micro-XRF, and calibration standards were explained; applications of micro-XRF in various samples such as earth science materials, environmental and nuclear materials, cultural heritage materials, biological materials, and industrial materials were introduced.

Although articles dealing with only X-ray structural images are not mentioned in this review article, one significant and instructive review article on the topic will be introduced here. Sakdinawat and Attwood[9] wrote a review article on "*Nanoscale X-ray imaging*". X-ray microscopy optics such as Fresnel zone plates (ZP), Kirkpatrick-Baez (KB) glancing incidence mirrors, and multilayer Laue lenses were discussed. Small errors in optical shape can affect the image resolution of nanoscale focusing lenses, especially KB mirrors. Thus, a precise nanofabrication technique is required for high quality X-ray focusing optics. X-ray imaging techniques based on full-field X-ray microscopy and scanning micro-XRF analysis were also discussed. Finally, applications of nano- and microscale X-ray imaging in material science, biology, environmental science, archeology, paleontology, and cultural heritage studies were reviewed therein.

DETECTION

Normally, high-resolution XRF spectra with a few eVs are obtained by a crystal or multilayer analyzer. However, such crystal spectrometers have the disadvantages of a small solid angle of X-ray detection and energy scanning. For resolving these problems, the microcalorimeter with a low heat capacity is a promising energy dispersive X-ray detector, whose energy resolution is an order of magnitude better than that of conventional semiconductor-based energy dispersive detectors, such as Si or Ge detectors. X-ray absorption fine structure (XAFS) measurements are usually performed using energy dispersive detectors. In this case, the microcalorimeter can be very powerful due to its low detection limits for target elements. Ukibe et al.[10] at the Photon Factory at KEK, Japan, fabricated a superconducting tunnel junction (STJ) detector for the soft X-ray region. They patterned the STJ detector by removing the SiO_2 deposition layer using a lift-off technique to avoid contamination of the top Nb electrode, resulting in almost no artifact photon events. The performance of a 100-pixel array detector showed an energy resolution of about 30 eV for total absorption of Kα lines of oxygen and nitrogen. Since this system is promising from the viewpoint of count rate, such type of detector will be a standard X-ray detector for XAFS at SR facilities. Jach,[11] at the National Institute of Standards and Technology (NIST) in the USA, investigated the analytical performance of microcalorimeters for the detection of X-ray fluorescence lines of light elements such as Al and Mg. He could successfully estimate the intensity ratios of the K$\alpha_{3,4}$ satellites to the K$\alpha_{1,2}$ main lines, where the energy difference between K$\alpha_{3,4}$ and K$\alpha_{1,2}$ is about 10 eV. Although the energy resolution of the microcalorimeter he used was 7 eV, such a satellite measurement would be interesting if the energy resolution could be improved down to 1 eV. For example, radiative Auger X-ray fluorescence satellites include oscillations similar to those in XAFS, and their analyses can, therefore, provide the local structure around the fluorescing elements. Since the intensity of the radiative Auger satellites is 10^{-3}−10^{-4} of the main lines, the use of microcalorimeters will be promising. Microcalorimeters were used for the investigation of plasmas in the ITER Tokamak.[12] Their purpose of the work was to ascertain the core ion temperature from the Doppler broadening of the W^{64+} resonance line at 9.1 keV, and it was claimed that the resolution of 2.5 eV was sufficient. Observations of X-ray lines have been mostly carried out using crystal spectrometers, in which shaped crystals have been used to increase the detection solid angle. However, from the viewpoint of efficient measurements, the use of a microcalorimeter can be appealing.

As represented by roentgenograms, X-ray imaging using X-ray films has played an important role in the history of X-ray applications. X-ray CCDs or other electrically controllable 2D detectors are rapidly replacing X-ray films or imaging plates owing to their quick electronic data transfer capability. Especially, X-ray CCDs have been steadily getting utilized in applications using X-ray free-electron lasers (XFELs), medical applications, X-ray astronomy, and protein crystallography. A group at the Max-Planck Institute in Germany published a series of papers about pnCCD, which is a focal plane detector for the XMM-Newton X-ray astronomy mission of the European Space Agency ESA.[13] The characteristic of the pnCCD is its high stability: after 10 years in space on a highly eccentric orbit, the detector energy resolution showed almost no degradation. This device will be combined with Wolter-I-type X-ray mirror systems. The instrumentation permits the exploration of the X-ray universe in an energy band from 0.3 to 10 keV by spectroscopic measurements with a time resolution of 50 ms for a full image consisting of 384 × 384 pixels. Their main goals are an all-sky survey using this X-ray telescope and investigation of the mysterious

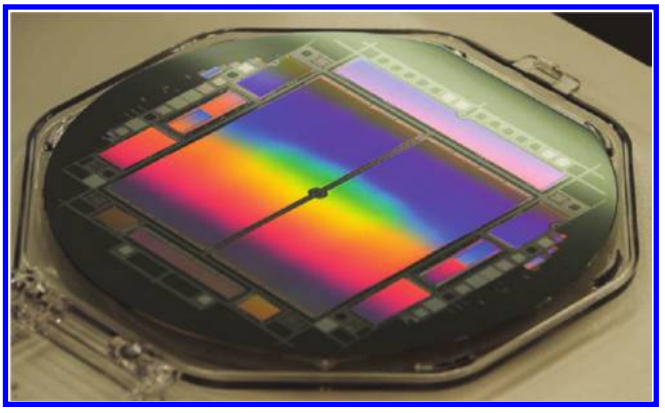

Figure 1. Photograph of a 150 mm wafer with two pnCCDs and a couple of test devices. Each detector half has a sensitive area of approximately 30 cm^2 filled with 1024 × 512 pixels of 75 × 75 μm^2. Reprinted from *Nucl. Instrum. Methods Phys. Res., Sect. A*, Volume 614, Strüder, L.; Epp, S.; Rolles, D.; Hartmann, R.; Holl, P.; Lutz, G.; Soltau, H.; Eckart, R.; Reich, C.; Heinzinger, K.; Thamm, C.; Rudenko, A.; Krasniqi, F.; Kühnel, K.-U.; Bauer, C.; Schröter, C.-D.; Moshammer, R.; Techert, S.; Miessner, D.; Porro, M.; Hälker, O.; Meidinger, N.; Kimmel, N.; Andritschke, R.; Schopper, F.; Weidenspointner, G.; Ziegler, A.; Pietschner, D.; Herrmann, S.; Pietsch, U.; Walenta, A.; Leitenberger, W.; Bostedt, C.; Möller, T.; Rupp, D.; Adolph, M.; Graafsma, H.; Hirsemann, H.; Gärtner, K.; Richter, R.; Foucar, L.; Shoeman, R. L.; Schlichting, I.; Ullrich, J., Large-format, high-speed, X-ray pnCCDs combined with electron and ion imaging spectrometers in a multipurpose chamber for experiments at 4th generation light sources, 483−496, Copyright 2010, with permission from Elsevier.

"Dark Energy". They claimed that its development had reached an important phase. Tomás et al.[14] developed a new micromegas X-ray detector in a CAST (CERN Axion Solar Telescope) experiment. The micromegas X-ray detector is more advanced than conventional micropattern gas detectors in terms of gain stability, efficiency, simplicity, robustness, energy resolution, readout features, and radiopurity. The detector has a background rate as low as 6×10^{-6} counts $keV^{-1}cm^{-2}$ at CAST, and this low-background feature is important in the field of rare event search.

Single-shot X-ray imaging is an important application in X-ray free electron lasers (XFEL) facilities. A characteristic required for quality detectors includes accurate intensity estimation of incoming strong X-rays within 10−100 fs. In addition, the detection of electrons and ions from target samples is of interest when irradiating them with ultraintense X-rays. The Max Planck Advanced Study Group with the Center for Free Electron Laser Science in Germany developed large-format, high-speed X-ray pnCCDs combined with electron and ion imaging spectrometers, of which the photograph is shown in Figure 1.[15] This instrumentation enables a new class of coherent diffraction experiments in which both electron and ion emissions from the target may be monitored simultaneously. Since the opportunities for experiments using XFEL are rigidly limited, the researchers want to collect as much signal as possible for understanding the dynamics of atoms, molecules, and clusters. A group at Cornel University developed a pixel array detector (PAD) for femtosecond radiation experiments.[16] The detector can deal with instantaneous count rates in excess of 10^{17} photons per second per pixel, features a per-pixel programmable two-level gain control, and can distinguish single photon events and also integrate thousands of photons at extremely high count rates, satisfying the requirements of the XFEL experiments. Fast 2D detectors are important in third-generation synchrotron radiation facilities. A 2D photon-counting X-ray detector system with 1.4 kHz frame rate, which is called MAXPIX (multichip area X-ray detector based on a photon-counting PIXel array), has been developed and commissioned on European Synchrotron Radiation Facility (ESRF) beamlines by an ESRF group.[17] The system is equipped with fast photon-counting readout chips. An effective time resolution of 60 ns was achieved using the ESRF pulse modes. This system is promising for time-resolved experiments, such as pump−probe experiments with time resolutions in the 100 ns range. In an X-ray CCD development group in Germany, Schalf et al.[18] made a compact X-ray camera with high energy resolution, that was named as a color X-ray camera (CXC). If a color Laue photograph could be measured from a single crystal, in which all measured spots have X-ray energy information, it would be useful for the structure analysis. The camera was tested at the new synchrotron radiation facility, BESSY II, in Germany. It could simultaneously record 69 696 spectra with an energy resolution of 152 eV for manganese Kα with a spatial resolution of 50 μm over an imaging area of 12.7 × 12.7 mm^2. Elemental X-ray images provided by the CXC were shown for the skull of a red-toothed shrew and a ceramic fragment.

Scintillator-coupled image sensors play an important role in X-ray scattering experiments at synchrotron radiation facilities. Shinohara et al.[19] developed an indirectly illuminated X-ray area detector for X-ray photon correlation spectroscopy. The detector consists of a phosphor screen, an image intensifier, a coupling lens, and either a CCD or CMOS image sensor. They were able to measure speckle patterns with a high signal-to-noise ratio at a single shot in the integrated mode, while X-ray photon correlation spectroscopy (XPCS) measurement could be performed with much fewer photons in the counting mode. By switching modes and sensors, the detector can be applied to many kinds of samples for XPCS measurements. Studies of the characteristics of the scintillators themselves are also important when 2D X-ray detectors are developed. Matsuo and Yagi[20] studied the decay time of YAG:Ce^{3+} using a CMOS camera. The measured decay time was 60 ns. This result showed the possibility of time-resolved X-ray diffraction experiments on this order by combining with a fast image sensor. Freed et al.[21] derived an analytical model for detector blur functions using Monte Carlo simulation, and experiments as accurate models are crucial for performing meaningful optimizations of 3D X-ray breast imaging systems as well as for developing reconstruction algorithms that faithfully reproduce the imaged anatomy. Such a basic study is important for optimizing computed tomography (CT) imaging systems.

Since X-ray events from space are rare, investigation of the polarization of X-rays is important for understanding the dynamic behavior of highly charged ions in space. The Compton polarimeter is one of the applications of a 2D position sensitive detector. Weber et al.[22] developed a 2D position sensitive Si(Li) detector dedicated to Compton polarimetry. They claimed that this polarimeter worked efficiently for X-rays in the energy region from 70 to a few hundred keV. Although conventional gas and pure Ge pixel detector-based polarimeters have existed, the Si(Li)-based polarimeter seems to cover the X-ray energy region for which these polarimeters do not work efficiently. Ryan et al.[23] developed an interesting pixel array detector, named "Maia". This detector is an array of 20 × 20 detectors, each 1 × 1 mm^2 in area, with a central grid of 4 × 4 detectors. They applied the

detector to elemental X-ray imaging of a geological sample. Owing to the center beam path hole in the detector, the detector could be positioned upstream at a distance of 10 mm from a sample. Thus, the solid angle of the detector was very large. This setup is effective for X-ray fluorescence analysis or fluorescence yield XAFS. An avalanche photodiode can detect X-ray photons at a very high count rate of up to 10^{10} cps. Kishimoto et al.[24] developed many kinds of avalanche photodiodes. A 16-channel array detector was developed for the detection of nuclear resonant scattering by the Mössbaur effect. They also made a fast amplifier using hybrid ICs. The time resolution was 0.3 ns with pixelated position sensitivity. This feature is useful for recording a decaying structure of delayed radiation from excited nuclei after prompt elastic scattering.

Energy-discriminating semiconductor detectors like CdZnTe for fast scanning, high-flux applications can significantly improve the multiple-energy imaging potential of systems such as those for medical computed tomography. For these applications, high-flux photon-counting capability on the order of one hundred million photons $mm^{-2}s^{-1}$ or higher is required. Prokesch et al.[25] experimentally investigated the possible correlation between high hole-trap concentrations in wide-bandgap semiconductors and delayed temporal responses of high-flux X-ray detector devices to changing photon fluxes. They derived important information that the detector signal stabilizes immediately upon flux onset by below-bandgap energy light illumination, which reduces concentration of active hole traps, independently of details of the semiconductor's point defect structure, and thus, CdZnTe crystals with high quality have been required. Now, their discovery might resolve this problem. Sato et al.[26] have developed an energy-discriminating X-ray CT system using a CdTe detector for reducing the absorbed dose for patients. The energy resolution of this system is 1.7 keV. They measured a cancerous rabbit ear, where iodine molecules remained. K-edge CT using photons with energy just beyond the K-edge energy of 33.2 keV enhanced the sensitivity for imaging the cancer. Such an energy discriminating X-ray CT will be a new trend in next generation CT systems. One of the obvious problems in energy resolving counting CT systems is the huge X-ray flux present in conventional CT systems. Reducing pixel size is one solution. However, below a pixel pitch of 300 mm, X-ray cross talk (Compton scatter and K-escape) and the effect of charge diffusion between pixels are problematic. In addition, by arranging the detector in several different layers, the count rate can be further reduced. Thus, Herrmann et al.[27] simulated performance of an X-ray detector with a combined Si and Cd(Zn)Te detection layer, where Si was at the top layer as its stopping power for X-rays is less than that of Cd(Zn)Te. Although the structure of the proposed layered device seems to be complex, it is one good solution for high-flux X-ray doses. TlBr is also a promising material for medical imaging detectors because it has a large optical bandgap of 2.68 eV and a high stopping power for X-rays and γ-rays, mainly due to its high atomic number. Destefano and Mulato[28] investigated the structural, optical, and electrical properties of thermally evaporated TlBr films. They found that the main fabrication parameter is the number of depositions needed to increase the film thickness. The thicker samples, which were fabricated using four runs, showed a larger ratio of photo-to-dark signals under medical procedures without losing their optical and electrical features.

As a promising candidate for detector material for the XFEL, $Nd_{0.67}Sr_{0.33}MnO$ has been studied by Yong et al.[29] Colossal magnetoresistive (CMR) manganites, such as $Nd_{0.67}Sr_{0.33}MnO$, have potential for bolometric radiation detection in a wide range of temperatures from room temperature down to ~100 K. The detector employed epitaxial thin films of $Nd_{0.67}Sr_{0.33}MnO$ grown on Si by pulsed laser deposition. The thermal sensor response changed linearly with the energy of an optical calibration laser, which is an alternative of the X-ray pulse of XFEL. Their work is the first practical use of a CMR Manganite bolometer. Chen et al.[30] studied lateral metal−semiconductor−metal structures with a thick amorphous Se layer ranging from 2 to 10 μm. The amorphous Se detector has advantages of superior spatial resolution, low dark current owing to a wide bandgap, and small concentration of deep localized states in the mobility gap. Compared to typical vertical-structured devices, the proposed lateral-structured device does not require high voltage. Furthermore, it was claimed that the absence of electron and hole blocking layers makes its fabrication easy. Li et al.[31] developed a flat-response X-ray detector for the measurement of radiation flux from a hohlraum in a laser facility. Flat response of a detector refers to the characteristic of reproducing constant intensities for any part of the energy range that it covers. Although traditional flat-response X-ray detectors can cover the photon energy range of 0.1−1.5 keV, the newly developed one can obtain a flat response in the photon energy range of 0.1−4 keV. The radiation temperatures inferred from the detector agree well with those from another diagnostic instrument that is large and complex. Kingsley et al.[32] studied interesting X-ray detectors based on organic photovoltaic devices. These devices, known as flexible electronic displays, use organic semiconductors with a large area and are inexpensive, lightweight, and flexible. Their prototype device consisted of a poly(3-hexylthiophene) polymer conjugated with a fullerene derivative phenyl-C61-butyric acid methyl ester and a sheet of the inorganic scintillator Gs_2O_2S:Tb. They studied its radiation hardness because the stability of organic materials is lower than that of inorganic materials and discussed the degradation process. The key feature of the organic X-ray detector is the substantial improvement of radiation stability. The historical development of the thermoelectrically cooled Si-PIN X-ray detectors was reported.[33] A hand-held XRF equipped with a small detector was developed and applied for alloy identification, process control of industrial manufactures, compliance with RoHS (restriction of the use of certain hazardous substances), and art and archeology.

X-RAY OPTICS

A hard X-ray mirror is usually realized using the phenomenon of total external reflection under glancing incidence. Shvyd'ko et al.[34] reported a diamond crystal with high reflectivity and high resolution under Bragg diffraction even at a normal incidence. A commercially available synthetic high-purity (type IIa) crystal grown under a high pressure and high temperature condition was used because it has the highest crystal quality and the lowest density of defects. The size of the crystal was about 8 × 4 mm^2 with a thickness of about 0.4 mm. Bragg reflectivity measurement was performed using monochromatic X-rays of 23.765 keV, which was suitable for C(995) Bragg reflection, at the Advanced Photon Source (APS), Argonne National Laboratory, USA. The experimental energy dependence of the Bragg reflectivity was shown. The experimental results indicated an energy width of 2.9 meV and a peak reflectivity of 0.87. Both values agreed well with the theoretically expected values. Diamond crystals are expected to

be used for the X-ray optics in the next generation of free-electron lasers.[35]

Mimura et al.[36] produced a nano X-ray beam with a width of 7 nm at 20 keV using a well-controlled KB mirror at Spring-8, Japan. The upstream mirror was designed to be a deformable mirror to compensate for the wavefront error that originated from the figure errors of the focusing mirror. A laterally graded Pt/C multilayer film was deposited by magnetron sputtering on the substrate, which was precisely prepared using computer-controlled elastic emission machining and stitching interferometry with an accuracy of 1 nm (peak-to-valley height).[37] X-ray microscopes with nanometer resolution, equivalent to that of electron microscopes, will be realized in the future. By employing the nanometer X-ray beam to XRF, XAS, and other methods, a variety of analytical applications will be feasible in the fields of medicine, biology, and materials science. A comprehensive overview of the curved graded multilayers was published with an emphasis on its application to KB mirrors by the researchers at ESRF.[38] A nano X-ray beam would be useful for high-spatial-resolution XRF imaging. A parabolic mirror was fabricated by the same technique.[39] This mirror produced a focused beam size ($1.3 \times 1.5\ \mu m^2$) for an X-ray energy of 30 keV with a long working distance of 300 mm. This micro X-ray beam was employed for XRF analysis of a freeze-dried section of eggplant root.

Sub-15 nm hard X-ray focusing was achieved by a new total-reflection zone plate (ZP).[40] The material of the ZP pattern was made of Pt (10 nm thick) on a Ti binder layer (5 nm thick) on a flat Si wafer. For an X-ray energy of 10 keV, a focusing size of 14.4 nm was measured at a focal distance of 4.16 mm. The same research group developed tandem-phase ZP optics which was fabricated by NTT-AT Corporation.[41] The zones were made of Ta, and two-phase zone plates were closely arranged in tandem. The ideal diffraction efficiency was expected to be 30% for an X-ray energy of 30 keV, which was about three times higher than that of a single ZP. This ZP produced a micro X-ray beam of $3.7 \times 4.1\ \mu m^2$ at a focal distance of 60.5 mm. The ZP optics was applied to a piece of float glass for scanning XRF microscopy. A zone-doubled ZP was developed for the multi-keV regime (4−12 keV) by an international research group at PSI in Switzerland, the University of Helsinki in Finland, and ESRF in France.[42] This ZP was made of hydrogen silsesquioxane (HSQ) resist and Ir with an outermost zone width down to 20 and 15 nm and aspect ratios higher than 25. A spatial resolution of sub-25 nm was achieved in the multi-keV range.

For the development of recent X-ray focusing optics such as ZP, the micro electro-mechanical system (MEMS) is critically important. Here, MEMS includes technical processes such as Si dry etching and X-ray lithography with the help of ray-tracing simulations. Ezoe et al.[43] showed the possibility of an X-ray fine focus of a diameter of less than 10 μm with an intensity gain of 1000−7000 at 1.49 keV (Al Kα). Parabolic crossed planar polymeric X-ray lenses, which are compound refractive X-ray lenses, were developed using electron and deep X-ray lithography techniques.[44] After the concept and design of the planar crossed lenses were explained in detail, the characteristics of the focusing linear planar lens were described. The focus size was 105 nm for X-rays in the energy range of 5 to 40 keV with an intensity gain of about 407. The compactness of the focusing microstructures will be a great advantage.

A review article on focusing polycapillary optics was recently published by MacDonald.[45] The history, theory, optical characteristics with experimental data, and their analytical applications to conventional micro-XRF, confocal micro-XRF, and X-ray diffraction (XRD) are included in the article. This article is recommended for those who are starting to use polycapillary optics.

Zhou et al.[46] developed a powder XRD instrument using polycapillary optics. Two X-ray sources (Rigaku RU-200 rotating anode and Oxford ultrabright microfocus source) were used in combination with collimating and focusing half optics. The diffraction intensity per sample area, average diffraction peak intensity, and average peak error were evaluated for different experimental arrangements. It was confirmed that the polycapillary focusing lens increased the diffracted intensity. Polycapillary optics was also applied to a diffraction imaging instrument.[47] A Mo anode X-ray generator equipped with a polycapillary half lens was employed for the XRD setup. The authors also used an energy-dispersive imaging detector with a polycapillary angular filter collimator. The imaging detector used was a controlled drift detector (CDD), which enables single-photon counting analysis, producing energy selective images. A polycapillary angular filter (30 μm in diameter for each capillary, 8 mm in active diameter, and 40 mm in length) provided by IfG GmbH was coupled to the detector. Diffraction images were acquired at a diffraction angle of 9° using polychromatic X-rays. The diffraction images of a simple model sample, composed of Nylon and Perspex, were obtained at different energy ranges of 16.5−18.5 keV and 12−14 keV, respectively. If the spatial resolution in the images and the energy selectivity are further improved, this technique will be very useful for XRD imaging.

Au-coated single glass capillaries were evaluated for micro-XRF analysis.[48] The inner walls of single glass capillaries (400 and 700 μm in diameter, 100 mm in length) were coated with Au by electroplating at a thickness of 100 nm. The critical angle for total reflection depends on the density of the material. The critical angle for Au is larger than that for glass. Therefore, the Au-coated capillary can guide many more X-rays from the X-ray source to the point for analysis by total reflection. As a result, the XRF intensity from the sample increased up to 1.5 times compared to the XRF intensity obtained using an uncoated glass capillary. Coating with high-density materials is a useful technique for improving the optical properties of X-rays under glancing incidence.

QUANTIFICATION AND FUNDAMENTAL DATA

Vanadium oxides promote a range of oxidation reactions, and quantitative chemical-state analysis of vanadium species is a subject of considerable interest because the oxidation state is one of key issues in controlling catalysis. High-resolution XRF spectroscopy is a powerful tool for estimating the chemical states of 3d transition metal compounds because of the strong relationship of both the peak width and peak shift of the Kα1 line with the number of unpaired 3d electrons and ligands. However, the use of the chemical shift of the V Kα spectra is not sufficiently reliable for an accurate determination of the oxidation states of vanadium species. The oxidation states of V Kα on Al_2O_3, SiO_2, and TiO_2 were analyzed quantitatively by a least-squares fitting of the full V Kα spectra recorded on a two-crystal XRF spectrometer.[49] Least-squares fitting analysis of the V Kα spectra combined with those of the reference compounds gave accurate and quantitative results, and a normalization procedure was essential for accurate quantitative analyses. The analytical procedure would be more useful if the XRF spectrum can be recorded at a synchrotron facility within a shorter time frame,

particularly in cases when the concentration of the element of interest is low or a highly space-resolved study is required.

The fundamental parameter methods (FPMs) for quantitative XRF require accurate knowledge of the spectrometer parameters, including the spectral distribution of excitation radiation. In the case of micro-XRF with a polycapillary optic in the excitation channel, the spectral distribution is changed due to the transmission properties of the lens. A new calibration procedure based on the fluorescence data of thin standard samples was developed to determine the excitation spectrum, i.e., the product of the X-ray tube spectrum and the transmission of the X-ray optic used, which could determine the polycapillary lens transmission and solid angle of detection of a micro-XRF spectrometer simultaneously.[50] The calibration result was validated by quantitative analyses of certified multielement reference standards. To overcome the difficulties with the spectral deconvolution, either the detector response function should be included in the spectral evaluation routines or the concept should be extended to a comparison of the calculated and measured spectra.

Confocal 3D micro-XRF can examine the 3D distribution of chemical elements in a sample with micrometer spatial resolution and can be useful for investigating heterogeneous, stratified materials like electronics, paint layers, or biological samples. The first application of quantitative 3D micro-XRF analysis of stratified materials using a Monte Carlo program was published.[51] Monte Carlo methods can model complex sample structures (e.g., heterogeneous, layered) under a range of experimental conditions and can account for other interfering effects, which are difficult to handle or cannot be solved analytically, e.g., scattering effects. Their quantification results were good when the method was applied to thin metal foils, bulk Cu metal, and a three-layered sandwich sample. The correlation coefficients between the experimental and simulated X-ray profiles of those samples exceeded 99%. Therefore, the Monte Carlo code was suggested to be a robust tool for the quantitative simulation of scanning confocal 3D micro-XRF experiments on stratified materials.

Minor and trace element analysis by micro-XRF for single crystal and polycrystalline materials are difficult due to diffraction phenomena, which obscure the elemental peaks and distort the spectral background. Sample rotation is commonly used in large area XRF to reduce these effects, but its use in micro-XRF is limited. A new quantitative micro-XRF analytical method based on FPM was reported.[52] This method employed multiple XRF spectra to quantify the element suite of single crystal and polycrystalline samples. The approach was to collect an XRF spectrum with unfiltered excitation at the low energy region, i.e., Na, Mg, Al, and Si, and then collect other portions of the spectrum under more optimized conditions (e.g., with a range of filters to obtain elemental intensities free of diffractive artifacts). By unifying the quantification of several spectra taken under different excitation conditions (each optimized for a particular set of elements), the overall results will be improved.

The concentrations of sulfur and other chemical elements in petroleum coke are the main factor determining the coke end-uses, and rapid and accurate analytical procedures are demanded. Gazulla et al.[53] described a methodology for the analysis of minor and trace elements in petroleum cokes by WD-XRF. To achieve the required detection limits and quantification limits, different stages of the process, ranging from sample preparation to measurement conditions, were optimized with the most critical step in determining the level of trace elements being sample preparation. The developed WD-XRF methodology was rapid and accurate with very low detection limits and measurement uncertainties. The same research group developed a WD-XRF method for determining the chemical composition of clay slurries directly without the need to dry and prepare the samples as fused beads or pellets for WD-XRF measurements.[54] A wide range of ceramic floor and wall tile bodies, which are used to prepare different slurry suspensions, were examined. The effect of the suspension viscosity and suspension solid content on the WD-XRF measurements was not significant, but the influence of the body composition type (floor or wall tile) was considerable. The method developed was claimed to be rapid, reproducible, and accurate.

XRF is applied widely in the analysis of single layers and multiple layer films, individual particles, art and archeological objects, etc. Quantitative analysis of these materials, which are frequently classified as thin or intermediate-thickness samples, requires the application of adequate matrix correction methods that take into account the complex dependence of the analyte fluorescent intensity on the matrix and sample thickness. To quantitatively extract the change in thickness and chemical composition of a InGaAs ternary semiconductor film from a space resolved SR-XRF map, Mino et al.[55] proposed a theoretical influence coefficient algorithm based on the use of only a few reference materials coupled with the FP approach that was optimized for intermediate thickness samples. This approach dealt successfully with the problems normally present in intermediate-thick films, in which the composition and thickness are both unknown. This technique might be useful for improving the growth process and the design of advanced optoelectronic devices.

In theoretical calculations for quantitative X-ray analysis, accurate fundamental atomic data is essential, including data for the mass attenuation coefficients. Sharanabasappa et al.[56] attempted to obtain accurate mass attenuation coefficients of low energy X-rays using a high resolution HPGe detector and radioactive sources. The advantage of the configuration involving an HPGe X-ray detector is its wide energy operational range from 3 to 500 keV and very good energy resolution. As a result, the energies of the photons degraded in energy due to small angle scattering and multiple scattering as well as the Kα and Kβ lines detected by the detector were well resolved. The mass attenuation coefficients obtained in such a configuration corresponded purely to the respective energies only, i.e., Kα, Kβ, and γ-rays. The method was evaluated using aluminum/nickel as the absorber reference material (RM). The results indicated that the "best value" for the mass attenuation coefficients could be obtained for those thicknesses in the transmission (T) range, $0.5 \geq T \geq 0.02$.

Traditionally, ED-XRF has not been used for the final certification of RMs because it is not considered as a reliable technique due to its peak overlapping and risk of incorrect background subtraction, leading to unacceptable uncertainty and bias of the results. Radtke et al.[57] reported that ED-XRF using a synchrotron radiation facility could be used for the certification of RMs. This method was based on a combination of measurements of pure elements or stoichiometric compounds as comparator materials and Monte Carlo simulations which considered all relevant effects such as self-absorption and enhancement. Measurement of the thick samples and thick comparators and simulation of the peak intensity ratios of those measurements proved to be a valuable tool for certifying RMs. The results were excellent from the subμg/g to μg/g level due to

dx.doi.org/10.1021/ac202871b |Anal. Chem. 2012, 84, 636–668

the elimination of the effects of the detector response and modeling of the higher order effects by Monte Carlo simulation. For the first time, the values obtained by ED-XRF were regarded as certified ones for RMs.

XRF quantification contains many uncertainties, one of which originates from the subtraction procedure of the spectral background originating from both the X-ray spectrometer and X-ray scattering in the sample. Calibration procedures for the X-ray spectrometer, even in conventional laboratories, have been available. Further, a physical model for X-ray scattering was implemented to calculate the physical background of the XRF spectra.[58] The XRF spectra for representative sample matrixes were measured and calculated by physically modeling the X-ray scattering background. The physical model was well supported by Monte Carlo simulations, but the modeling and simulations showed some deviations from the measurement. If their procedure is more refined, it could be used to predict the detection limits of trace elements in XRF and real transmission of X-ray polycapillary optics or to determine the mean atomic number of a scattering matrix, particularly for light element matrixes.

For FP-based quantification, detailed knowledge of the characteristics of the detector, including the efficiency, energy resolution, and the precise shape of the response function, is essential. Currently, most calculations of the X-ray detector efficiency assume that the source is a point source on the axis of symmetry of the detector, but this is not always the case. A Monte Carlo program that can simulate photon transport in Si(Li), silicon drift detector (SDD), and planar Ge detectors and can handle finite, tilted, and off-axis sources was reported.[59] The Monte Carlo code was claimed to provide an accurate prediction of the efficiency as a function of the X-ray energy, which could be suitable for incorporation in XRF and PIXE packages. This program can be particularly helpful for describing annular SDD detectors, which are difficult to quantify using analytical models. On the other hand, the program does not consider hot electron transport or charge carrier losses and ignores the contribution to the overall detection efficiency of the supporting pulse processor. Therefore, the program needs to be refined more in the future.

The quantitative characterization of samples using ion beams, such as H^+ and He^{2+}, can be useful for examining new materials and new applications in material science. The simulation of X-ray yields of multilayered samples is possible using a PIXE simulation, publicly released, open-source library, LibCPIXE, which allows the simulation of the X-ray yields of fully customized multilayered samples induced by proton beams. The simulation library became more versatile because it could allow the simulation of X-ray yields induced by a He^{2+} ion beam.[60] The major changes made to the publicly released version of the LibCPIXE was in the calculation of the L X-ray production cross sections of He^{2+} ions using a polynomial approximation to the universal ionization cross sections. Further studies will be needed to simulate the K X-ray yields induced by He^{2+} ions. Nevertheless, the results showed that the new LibCPIXE was adapted successfully and could simulate the L X-ray yields of pure and compound samples, including multilayered samples irradiated with He^{2+} as well as H^+ ion beams.

XRF analysis, although applied extensively to painting examinations, provides, in most cases, a qualitative indication of the presence of typical chemical elements in a color pigment because quantitative analysis requires microscopic homogeneity of the sample composition. A new model for describing the X-ray absorption in painting layers was presented by assuming the painting layer of small pigment grains embedded in a low-Z binding medium.[61] A linear law for autoabsorption inside the grains was assumed (due to the small size), and X-ray absorption in the medium was completely disregarded. The developed model was based on FPM using the layer thickness, pigment grain volume, and pigment grain volume density (dilution) as characteristic parameters of the sample. Nevertheless, the method could be applied only to a sample consisting of a single pure chemical element.

The X-ray spectrum from an X-ray tube at various applied voltages is an important fundamental parameter for quantitative XRF analysis. For quantitative FPM analysis, it is important to know the changes in the X-ray spectrum of an X-ray tube periodically when there is a change in the analysis parameters such as the tube voltage, detector, or filter. For this purpose, Sasaki et al.[62] proposed the use of an acrylic plate instead of the sample in the sample holder of an XRF spectrometer, in which the incident X-ray tube spectra could be obtained easily without calculation. The incident X-rays were scattered inelastically by the acrylic slab and lost ~1 keV of their energy by Compton scattering, but the overall spectral shape from the X-ray tube might be conserved. The scattered X-ray spectra of the acrylic slab were used to reproducing the dependence of the Pb Lα/Lβ intensity ratio on the X-ray tube voltage and on the material of the primary filter. Using the acrylic spectra as the primary X-ray tube spectra, it was shown that the incident X-ray spectrum could be substituted approximately by the acrylic scattered spectrum.

The large solid angle of the new detector arrays presents great opportunities and challenges for quantitative SR-XRF and PIXE microanalysis and elemental imaging. The large solid angle collects far greater count rates and offers the potential of lower detection limits, high quality imaging, and 3D modalities such as fluorescence tomography and X-ray absorption near-edge structure (XANES) imaging. On the other hand, a detector array can span a large range of takeoff angles at the sample surface. Therefore, modeling of the X-ray yields from a sample based on FPM needs to consider a wide takeoff angle, various analysis depths, and variations of efficiency and absorption paths to the detectors across the array. Ryan et al.[23] extended an FPM for quantitative PIXE and SR-XRF analysis and imaging by modeling the change in X-ray yields and detector sensitivity across large detector arrays. The peak-to-background was controlled by mitigating charge-sharing between the detector pads through careful optimization of a patterned molybdenum absorber mask. A geological application demonstrated that the method can produce high definition elemental images up to ~100 M pixels in size.

A primary filter, a metallic thin film placed between the X-ray tube and sample, is often used with ED-XRF for trace element analysis of RoHS, regulated elements, such as Cd and Pb. Despite the widespread use of a primary filter, many factors, such as optimal materials, thickness of the filters, and low detection limits, remain unclear. Ogawa et al.[63] investigated primary filter materials with different thicknesses, and the theoretical intensities of the fluorescent and scattered X-rays using brass containing a known concentration of lead were calculated for them. The detection limits using the theoretical intensities for several filter materials were obtained and compared with the values calculated using the measured intensities. Both values were similar for a 125 μm zirconium filter: 128.0 ppm using the theoretical intensities and 147.7 ppm using the measured intensities.

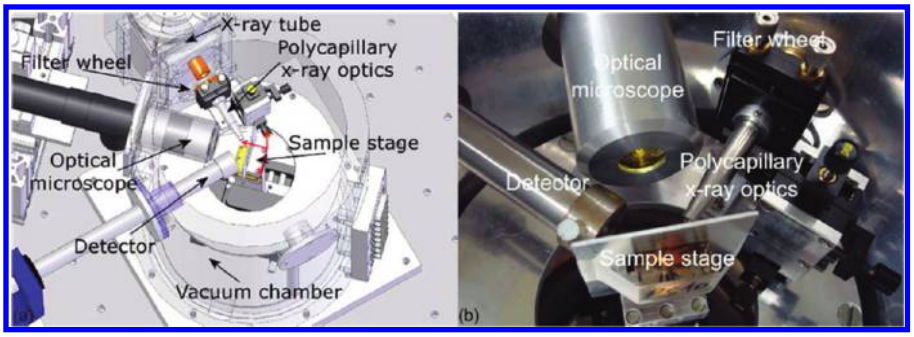

Figure 2. CAD design rendering and photograph of the interior of the spectrometer. The polycapillary is mounted on a five-axis adjustable stage; the microscope looks into the chamber through a 8 μm Kapton window, and the sample can be automatically moved in $x/y/z$. Reprinted with permission from Smolek, S.; Streli, C.; Zoeger, N.; Wobrauschek, P. *Rev. Sci. Instrum.* **2010**, *81*, 053707. Copyright 2010, American Institute of Physics.

This method was claimed to be effective in selecting the optimal filter for multiple samples and elements.

Quantitative SR-XRF measurements were carried out on naturally lead-contaminated samples.[64] The calibration procedure using the fluorescence to Compton scattered radiation ratio was evaluated using a Monte Carlo simulation. The experimental results with low-energy photons (14 keV) and simulations showed very good linearity of the fluorescence to Compton ratio as a function of the metal concentration, thereby assuring the reliable quantification of the elements. Lead, iron, and zinc were measured in samples of *Phaseolus vulgaris* (bean seeds), which had been grown using a nutritive solution with different levels of lead doping. For quantification of these naturally contaminated samples, the calibration must have been carried out for the fixed conditions of X-ray energy and scattering angle. The simulation allowed an evaluation of the matrix effect on the calibration curve and showed that linearity had been preserved, even in the presence of other heavy elements in the fluorescence spectrum. On the other hand, calibration must have been performed using samples with a similar matrix because the matrix affected the slope of the curve.

MICRO-XRF AND IMAGING

XRF imaging with micro- or nanometer resolution is a powerful tool for the acquisition of elemental distributions of a sample. Spatial resolution of an obtained elemental image critically depends on the size of the X-ray beam. Therefore, the development of superior X-ray focusing optics is a key technology for scanning-type XRF imaging. During the past decade, a nanofocusing X-ray beam ranging from submicrometer to several tens of nanometers has often been used for XRF imaging of actual samples using a specific beamline from a SR facility combined with KB mirror optics or a Fresnel zone plate. In addition, recent micro-XRF imaging has been performed in the laboratory using polycapillary X-ray focusing optics.

Smolek et al.[65] designed and developed a laboratory micro-XRF spectrometer, especially suitable for light element ($Z \geq 6$) analysis, which is shown in Figure 2. This spectrometer consists of an air-cooled 50 W Mo X-ray tube, polycapillary X-ray optics having a focal spot size of 32 μm at Mo Kα, motorized sample stage, high resolution CCD microscope, and a Si(Li) X-ray detector. The whole setup is placed inside a custom vacuum chamber to eliminate absorption of primary radiation including Mo L lines and low energy fluorescent radiation. By measuring a soda lime glass (NIST 621 standard reference material), the detection limits (DLs) with the proposed spectrometer were 878 ppm for Na, 115 ppm for Al, 95 ppm for Si, 22 ppm for K, and 15 ppm for Ca.

Matsuyama and Yamauchi et al.[66] developed a cryo-scanning XRF microscope (cryo-SXFM) to visualize the distributions of major and minor elements in biological samples such as tissues and cells. The SXFM system at BL29XUL of Spring-8 using KB mirror optics can create an X-ray nanobeam with a spatial resolution down to 30 $\times$ 50 nm^2. However, the actual experiments were performed with the focused beam at a resolution of 500 nm in order to measure entire cells quickly with a sufficiently large photon flux. The samples (NIH/3T3, mouse embryonic fibroblast cell line) were quickly cooled and frozen to a temperature of 126 K by a compact vibration-free refrigerator. The sample tissue, a sample holder (consisting of the refrigerator and a fine xy-stage), and a SDD were placed inside a custom vacuum chamber generating a high vacuum on the order of 10^{-5} Pa. Elemental distributions of Fe, Zn, Cu, Ca, and K were visualized at the NIH/3T3 single cell by measuring the cryo-SXFM system. A research group in Antwerp University, Belgium,[67] developed three types of mobile micro-XRF systems (Instruments A, B, and C) for in situ analysis of historical paintings. Instrument A is a conventional micro-XRF system equipped with a 60 W X-ray tube, a polycapillary X-ray lens, and a SDD. In contrast, Instruments B and C apply the unique configurations equipped with one microfocus X-ray tube and four SDDs. Primary X-rays were focused by a Pb pinhole collimator with a diameter of 0.8 mm (Instrument B) and a polycapillary X-ray lens (Instrument C). The SDDs were mounted at angles of 45, 51, 54, and 64° relative to the primary X-ray beam. The DL values were calculated from the XRF spectra of the glass standard reference material NIST SRM 611. As compared to the DL values of these instruments, the DL values of Instruments B and C showed a 3- to 10-fold improvement. The imaging capabilities of the developed instruments were demonstrated on three actual historical paintings. The first, entitled "Triptych of the Seven Sacraments", was measured by Instrument A. The second, entitled "Supper at Emmaus", was measured by Instrument C. The third, Vincent Van Gogh's "Patch of Grass", was measured by Instrument B. Yonehara et al.[68] developed a transportable micro-XRF instrument using polycapillary optics (half-lens type). The developed instrument consists of a microfocus X-ray tube (9.6 W Pd anode), two independent polycapillary half lenses, two compact lasers for visualization of the analytical position, and a Si-PIN X-ray detector. In the proposed configuration, the polycapillary half lens placed between the sample and the X-ray detector is

dx.doi.org/10.1021/ac202871b |*Anal. Chem.* 2012, 84, 636–668

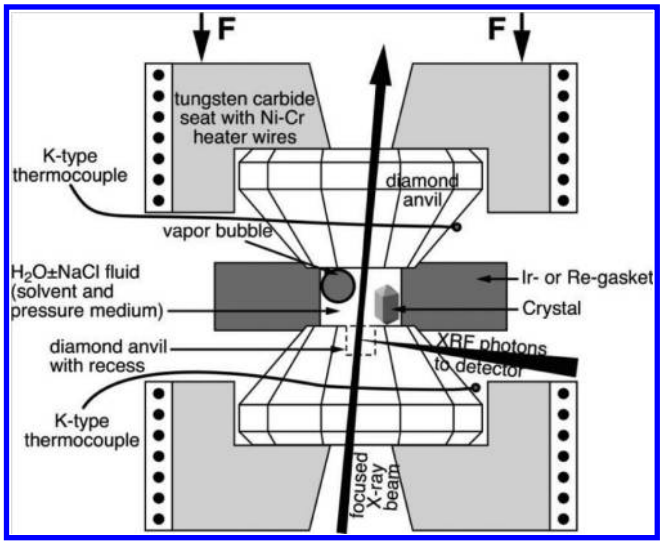

Figure 3. Schematic drawing showing the details of the hydrothermal diamond anvil cell designed for the in situ analysis of fluids at high pressures and temperatures using micro-XRF analysis. Figure 3 from *J. Synchrotron Rad.* (2010). 17, 669−675 [doi: 10.1107/S0909049510023654].

used to limit the size of the analytical region. The spatial resolutions of the spectrometer were 100 and 170 μm at Fe Kα, depending on the polycapillary lens applied. The DL values calculated from measuring the steel reference materials were 0.05% (V and Cr), 0.036% (Mn), and 0.059% (Ni).

Another important trend in XRF imaging is 3D elemental analysis. In particular, a confocal arrangement using two independent polycapillary optics for excitation and detection of XRF is a powerful tool for nondestructive 3D elemental imaging. Tsuji and Nakano[69] developed a tabletop confocal micro-XRF instrument with fine spatial resolution using a high-power fine-focus X-ray source, advanced polycapillary optics, and a SDD with a large sensitive area. To obtain the fine confocal volume, noble, advanced polycapillary full- and half-lenses were used on the excitation and detection sides with a working distance of less than 3 mm. Both polycapillary X-ray lenses were set in the optimum confocal geometry with the angle between the incident and detection beams adjusted to 90°. The focal spots of both lenses were precisely adjusted to be at one common point using a motorized *XYZ* stage with a precision of 0.5 μm. The depth resolution of the developed confocal XRF evaluated by thin layer scanning was varied from 22.6 to 13.7 μm for an energy range from 5.41 keV (Cr Kα) to 11.4 keV (Au Lβ), respectively. These depth resolutions were improved by a factor of 3−4 over that obtained by previous 3D-XRF instruments developed by the same research group. The confocal configuration was applied to the in situ analysis of fluids at high pressure and high temperature. Wilke et al.[70] performed confocal micro-XRF and XAFS experiments with a diamond anvil cell, which is a device capable of generating pressure almost as high as that at the center of the Earth. As shown in Figure 3, a hydrothermal diamond anvil cell (HDAC) optimized for their experiments was mounted on a motorized *XYZ* sample stage and can be rotated around the vertical axis. A detection side polycapillary half-lens with a long working distance of 50 mm was used for the experiment because the HDAC chamber was mounted in front of the polycapillary half lens. Therefore, the depth resolutions were not so small (225 μm at 8.0 keV and 108 μm at 16.6 keV). Additional information on the depth resolution under the conditions of the in situ experiments is confirmed by scans across the HDAC sample chambers that contained zircon ($ZrSiO_4$) and hafnon ($HfSiO_4$) crystals.

An interesting trend in 2D- and 3D-XRF imaging techniques is the combined use with micro computed tomography (micro-CT) that can provide morphological information of the sample. De Samber et al.[71] demonstrated 3D elemental imaging of Zn, Fe, and Ca in a crustacean *Daphnia magna* and an egg of *Daphnia magna* by combining confocal micro-XRF and absorption micro-CT. The author's research group reported similar experiments with 2D-XRF imaging in combination with micro-CT in 2008. The confocal micro-XRF experiment was performed at Beamline L of the DORIS III storage ring, HASYLAB (Germany). A quasi-monochromatic X-ray beam at 19.7 keV by a Ni/C monochromator is focused to 12 μm by polycapillary optics for excitation. The detection side polycapillary half-lens with a working distance of 2 mm was attached to a SDD. The depth resolution of the confocal XRF evaluated by scanning a multielement thin film standard was varied from 15 to 40 μm for an energy range from Pb L line to Pb M line. The use of a fast dynamic scanning approach could provide 3D distribution of major, minor, and trace elements in specific regions within *Daphnia magna*. Patterson et al.[72] demonstrated integrated 3D images using a laboratory-based micro-CT and a confocal micro-XRF instrument. The laboratory-based confocal micro-XRF spectrometer was constructed at Los Alamos National Laboratory. A laboratory X-ray source (25 W Ag anode) and a Si-PIN detector were used for the confocal micro-XRF spectrometer. The confocal volume of the instrument was evaluated by scanning a 10 μm thick Ta foil to be approximately 30 × 30 × 65 μm at energy of Ta Lα (8.15 keV). A micro-CT scanner was used for the observation of the sample morphology. A tungsten X-ray source was used to generate a broad X-ray spectrum from 40 to 150 kV, with a 5 μm spot on the target and 43° cone shaped X-rays. In addition, a thermoelectrically cooled CCD camera with a 2048 × 2048 pixel array was installed. The data obtained from the confocal micro-XRF and the X-ray CT scanner were imported into "MATLAB (matrix laboratory)" software for 3D rendering. Two X-ray techniques for 3D modeling were applied to two samples: an integrated circuit surface-mounted resistor and a machined piece of polystyrene foam. Pereira et al.[73] developed a transmission micro-CT system combined with an XRF micro-CT system to determine elemental distribution in biological samples (breast, prostate, and lung samples). The experiments were performed at the X-ray fluorescence beamline (D09B-XRF) of the Brazilian Synchrotron Light Laboratory. A quasi-monochromatic X-ray beam at 12 keV by a W/C monochromator was collimated to a 200 × 200 μm^2 area with a set of slits for excitation. The sample was placed on a high-precision goniometer and translation stages that enabled one to rotate as well as translate perpendicularly to the beam. The fluorescent X-rays were collected with an HPGe detector placed 90° to the incident beam, while the transmitted X-rays were detected with a fast Na(Tl) scintillation counter placed behind the sample. The transmission micro-CT images were reconstructed using a filtered back-projection algorithm. The XRF micro-CT images were reconstructed using a filtered back-projection algorithm with absorption corrections. The 3D images were reconstructed using 3D-DOCTOR software. The results obtained from the 3D

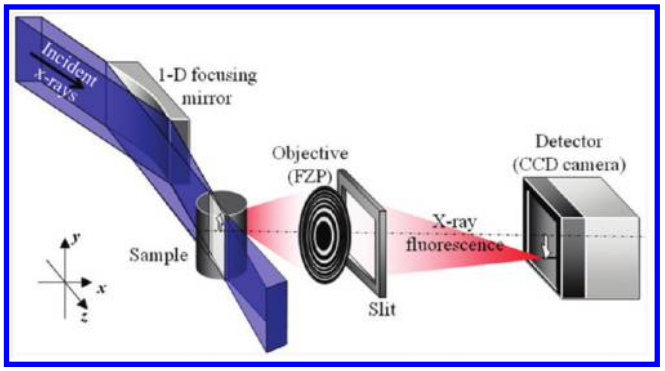

Figure 4. Schematic diagram of confocal full-field X-ray microscope at a SR facility (Spring-8). Reprinted from *Nucl. Instrum. Methods Phys. Res., Sect. A*, Vol. 616, Takeuchi, A.; Terada, Y.; Uesugi, K.; Suzuki, Y., Three-dimensional X-ray fluorescence imaging with confocal full-field X-ray microscope, 261−265, Copyright 2010, with permission from Elsevier.

visualization showed that the distributions of Fe, Cu, and Zn were different and heterogeneous.

Up to now, XRF imaging has mostly been available using a scanning method in which the sample is scanned with a fixed X-ray beam. The measurement by this scanning method becomes time-consuming as the scanning area under analysis increases. Another elemental imaging technique is a full-field method using an X-ray CCD detector. Tsuji et al.[74] developed a new WD-XRF imaging spectrometer equipped with a two-dimensional X-ray detector in the laboratory at Osaka City University. The configuration of the proposed spectrometer is similar to the conventional WD-XRF geometry. In the proposed configuration, straight-type polycapillary optics and an X-ray CCD detector with a Gd_2O_2S:Tb scintillator were applied instead of a Soller slit and a conventional X-ray detector, respectively. Fluorescent X-rays emitted from the sample were guided through the straight polycapillary to the exit of the optics by total external reflection of X-rays. The collimated X-ray beams were dispersed by the analyzing crystal (LiF(200)) in the same way as in the conventional WD-XRF spectrometer. This experimental setup enabled the analysis of X-ray fluorescence having positional information of elemental distribution on the surface of the sample, leading to 2D-XRF imaging. The energy resolution of the developed spectrometer was 130 to 152 eV at the Zn Kα peak. The X-ray images of Cu Kα and Ni Kα were differentiated by the X-ray CCD detector at the corresponding diffraction angles. The same research group proposed a different type of 2D-XRF imaging system using two independent straight polycapillary optics.[75] In the proposed system, the total reflections on the inner wall of each capillary in the straight polycapillary were used for energy filtering in XRF. The first straight polycapillary is placed in front of the sample, and the second straight polycapillary is attached to the CCD detector mounted on a circular stage. The second straight polycapillary, X-ray CCD detector, and samples were set in a single straight line. The first straight polycapillary collimates the fluorescent X-rays emitted from the sample and creates parallel X-ray beams. After the fluorescent X-rays pass through the first polycapillary, the X-ray beam is introduced into the second polycapillary. Then, the second polycapillary is inclined slightly by the circular stage less than 1°. The X-rays taken into the capillary at angles greater than the critical angle are absorbed in the capillary without total reflection. Only the X-rays obtained at less than the critical angle for total

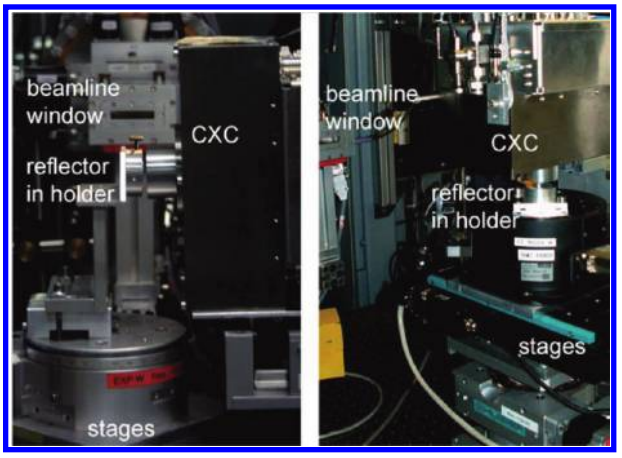

Figure 5. Photographs of setup 1 (left) and setup 2 (right), left photo is taken looking toward the exciting beam and right photo is taken from the side. Prototype of a color X-ray CCD camera (CXC) is applied for TXRF analysis. Kühn, A.; Scharf, O.; Ordavo, I.; Riesemeier, H.; Reinholz, U.; Radtke, M.; Berger, A.; Ostermann, M.; Panne, U. *J. Anal. At. Spectrom.* **2011**, *26*, 1986−1989. Reproduced by permission of The Royal Society of Chemistry.

reflection are guided into the polycapillary, and then, they are detected by the CCD detector. This XRF imaging gave an energy filtered X-ray image between Cu Kα (8.0 keV) and Fe Kα (6.4 keV) at specific angles; however, elementally selective XRF imaging was difficult. Takeuchi et al.[76] demonstrated 3D-XRF imaging using a confocal full-field X-ray microscope with sub-micrometer spatial resolution, of which a schematic diagram is shown in Figure 4. Their experiment was performed on undulator beamline 37XU of SPring-8. The proposed full-field X-ray microscope system consists of a Fresnel ZP fabricated with electron beam lithography and an X-ray CCD camera as an image detector. The arbitrary cross-sectional region of the sample was irradiated with a 10 keV X-ray sheet beam at a glancing angle. The XRF from the sample passed through the ZP object and was simultaneously imaged by the X-ray CCD detector. Therefore, a sliced image could be obtained with one-shot exposure.

TOTAL REFLECTION X-RAY FLUORESCENCE ANALYSIS

TXRF is a well-established analytical technique. Primary X-rays irradiate the surface of a flat sample support. The X-ray fluorescence emitted from the sample deposited on the sample support is detected by an EDS detector placed just above the sample. Impurities on a Si wafer can be directly measured by TXRF, and thus, TXRF has been routinely applied by Si semiconductor companies for the contamination control of Si wafers. The proceeding of the 13th conference on TXRF and related methods, which was held in Gothenburg, Sweden in 2009, was published in a special issue of *Spectrochim. Acta, Part B*.[77] Readers can learn of the TXRF research trends from this proceeding. In addition, a review article on synchrotron radiation induced TXRF (SR-TXRF) was published.[78] SR is an ideal X-ray source for high sensitivity TXRF analysis due to its high intensity, linear polarization, and small divergence. In this review article, after discussing a history of TXRF research, the fundamentals of TXRF analysis were described and recent applications of TXRF were introduced. One of the advantages of SR is that the energy

dx.doi.org/10.1021/ac202871b |*Anal. Chem.* 2012, 84, 636–668

of the X-rays can be changed, which enables XAS (EXAFS) analysis under a condition of total reflection. The authors reported on their recent results of SR-TXRF and XANES analysis of Fe contamination on a Si wafer. Fe oxidation states were determined by XANES analysis by comparison with the XANES spectra obtained from standards. They also summarized the results of the characterization of atmospheric aerosols by SR-TXRF and XANES.

In a conventional TXRF instrument, an EDS is applied for TXRF analysis. One of the recent trends in the detectors used in TXRF is a large area EDS because it is useful for highly sensitive XRF analysis. Another trend in XRF is to obtain an elemental distribution on the surface of the sample. Usually, the sample is scanned by a fixed EDS having a small pinhole, leading to surface-sensitive 2D-XRF mapping under a condition of total reflection. However, this process is time-consuming. Recently, a color X-ray CCD camera (CXC) was employed for fast TXRF mapping.[79] The prototype of a CXC camera chip consisted of 264 × 264 pixels with a single pixel size of 48 × 48 μm^2 and an energy resolution of 152 eV at 5.9 keV. The CXC was used with a straight polycapillary to provide a 1:1 image on the CCD. Each pixel recorded a full XRF spectrum by photon-counting analysis. The preliminary experiment was performed at a SR facility (BAM line at BESSY II, Berlin, Germany). Figure 5 is a photograph of the TXRF instrument with reflector and CXC at the SR facility. Residues of droplets of standard solutions with a single element mass of 50 ng were successfully imaged in 30 s. This new X-ray detector will open new TXRF application fields and related methods.

When the dried residue of the solution is measured by TXRF, the shape and inhomogeneity of the residue influence the quantitative result. Thus, the elemental distributions and homogeneity of the residues were investigated by the SR-induced micro-XRF method.[80] Multielement solutions of five microliters from four different standard solutions including V, Mn, Ni, and Ge were pipetted onto the Si reflector. An X-ray beam with a beam size of 2 × 6 μm^2 with excitation energy of 12.5 keV was applied to the residue (418 × 360 μm^2). SR-induced micro-XRF images of the multielement sample were measured. A good relationship between the Ni and V XRF intensities was obtained for the micro-XRF result with an R^2 value of 0.9625. This result indicates that both elements were distributed homogenously inside the sample, justifying an internal standard technique for TXRF quantification.

Sample preparation is critically important for quantitative TXRF analysis. Self-absorption in the dried residue of the TXRF sample is one of the problems in TXRF quantification. To solve this problem, a nanoliter (or picoliter) solution deposition technique has been studied. Sparks et al.[81] characterized the dried residues using SEM observation and Auger electron mapping. The authors confirmed a good linear relationship between the TXRF intensity of Ni Kα and the Ni amount in the deposited droplet with R^2 value of 0.990 for up to a 35 ng Ni level. A SEM image indicated that a 9 pL droplet gave a diameter of the dried residue from 6 to 14 μm depending on the concentration of Ni in the solution. A SEM image of a cross section of the 1 g/L Ni residue from a 9 pL deposit was observed. This image directly gave the height of the residue that was 1.48 μm. In addition, the crystalline structure of the residue was revealed from cross-sectional SEM. It was also confirmed that the Si matrix does not affect the detection of Ni from a Ni standard solution. Finally, the detection limit of Ni was evaluated to be 3.4 ppb in the deposition condition of 69 nL of Ni solution in an 88 × 87 array.

In conventional TXRF analysis, a small volume taken from the sample solution is dropped on the sample carrier (e.g., flat glass plate). In this case, preconcentration or speciation is not expected, although chemical speciation is an important procedure in other spectroscopic analytical methods such as ICP-OES and AAS. Hatzistavros and Kallithrakas-Kontos[82] proposed the application of an anion-selective membrane that was prepared on the surface of a TXRF quartz reflector. This anion-selective membrane concentrated perchlorate anions in drinking water. The membranes were prepared on the quartz reflector by mixing the membrane solution (EVA (polyethylene-*co*-vinyl acetate), plasticizer, and Aliquat-336 extractant in THF solvent) and the ligand solution. The equilibration time between the membrane and water sample was typically from 2 to 20 h. Then, the membrane on the glass reflector was directly measured by TXRF in the laboratory. The XRF intensity of Cl Kα gave the concentration of perchlorate in drinking water. The DL was 0.8 ng/mL (ppb) for 100 s measuring time. An anion-selective membrane with high selectivity on the reflector is a promising technique for expanding the applications of TXRF.

Trace analysis of contaminations on a Si wafer is one of the important applications of TXRF. To improve the sensitivity of TXRF analysis, vapor-phase treatment (VPT) is a useful technique. In VPT, the Si wafer surface is decomposed with hydrofluoric acid vapor (HF) and then analyzed by TXRF after being dried. The feasibility of the VPT-TXRF technique for detection of trace elements in a 10^9 atoms/cm^2 level was investigated.[83] It was found that the improvement of sensitivity varied with process conditions. The authors concluded that the optimum result was obtained under the VPT condition of condensation on the Si surface in a humid atmosphere at a cool stage temperature of around 10 °C.

Trace analysis of low-*Z* elements is difficult because of strong absorption of their low energy X-rays in air and the window material. Therefore, a vacuum chamber needs to be employed in the TXRF instrument. TXRF analysis of low-*Z* elements such as Na, Mg, and Al in a uranium matrix was performed with a Cr Kα excitation source in the vacuum chamber.[84] A Peltier cooled SDD with an ultrathin Kapton window gave the TXRF spectrum with low background intensity and with good energy resolution in the low energy region. The amount of low-*Z* elements was determined by the addition of the Sc internal standard. Bennun and Sanhueza[85] reported that chemical compounds of stoichiometric compositions and high purity, including at least two elements such as K and Mn in $KMnO_4$, could be used for alternative materials of certified standard materials in quantitative TXRF analysis.

Sanchez et al.[86] discussed the experimental setup of TXRF using polycapillary optics. Although applications of polycapillary optics have already been reported, the authors compared the analytical performance of the TXRF setups with a half polycapillary and beam guide optics, which were used for collimation of the primary X-rays in combination with a micro focus X-ray tube. It was mentioned that the X-ray intensity on the surface in TXRF using a half polycapillary was significantly lower than that in the conventional configuration, leading to poorer detection limits, especially for the low energy region. A planar X-ray waveguide resonator was employed for TXRF.[87] This X-ray optics coupled well with the sample holder, and the X-ray detector coupled with the collimator. A similar waveguide was employed

for a portable TXRF spectrometer.[88] This waveguide was placed between a small X-ray tube and the sample carrier to produce a sheet-type X-ray beam (10 μm height and 10 mm wide). A detection limit of 26 pg for Co was reported. The same portable TXRF instrument was employed for the detection of Cd in solution.[89] The detection limit of Cd was 1 ng with a measuring time of 1800 s. Three papers[87−89] showed that downsizing the TXRF instrument was effective in improving analytical performance even if a low power X-ray tube was applied.

Grazing incidence XRF (GIXRF) is a useful technique for elemental depth profiling. The XRF intensity emitted from the sample drastically changes as the incident angle changes and is especially sensitive for a surface layered structure. Pepponi et al.[90] studied GIXRF in combination with secondary ion mass spectrometry (SIMS) for characterization of ultrashallow As distribution in Si. The GIXRF spectrometer is shown elsewhere.[91] SIMS is also useful for depth profiling although the technique is destructive. In addition, it is known that SIMS is very sensitive for detecting trace elements; however, the quantitative analysis is not reliable. In the case of GIXRF, information on deeper layers can be obtained at large incident angles, and yet, it is difficult to get clear depth profiles. The authors proposed an algorithm which could fit the GIXRF experimental data using SIMS profile. The combination of both techniques was claimed to produce reliable quantitative depth profiles. Streeck et al.[92] studied elemental depth profiling of Cu(In, Ga)Se2 thin films by reference-free GIXRF. They calculated XRF intensities using fundamental atomic parameters. The calculations and the experimental data, obtained at SR facility (BESSY II, Germany), showed that this is a promising technique for distinguishing small differences in Ga/In profiles. Since preparation of reference material for elemental depth profiling is difficult, further development in this research field is desired.

Tiwari et al.[93] reported an application of a multilayer mirror as a sample carrier for TXRF. An X-ray field under the Bragg reflection condition was used for XRF analysis. X-ray field intensity distribution on the surface of a W/C multilayer was calculated as functions of incident angle and the height above the surface. Fe Kα intensities were shown for the particles with different particle sizes on the multilayer. This result indicates that the absorption effect by the particles in the total reflection region is dominant for the particles with a size larger than 1.5 μm. The authors proposed XRF analysis under strong Bragg reflection condition at an incident angle of about 0.5°. When XRF analysis of aerosol particles deposited on the multilayer was performed, the detection sensitivity improved by 15−18% was observed. The problem with this technique is the availability of the multilayer for routine analysis. The same authors developed CAT-GIXRF computer program for GIXRF and X-ray reflectivity (XRR) measurement.[94] The program was developed considering the multiple refraction and reflection of X-rays in a multilayered material on a flat substrate. GIXRF is useful for elemental depth profiling, but it is not very sensitive for determining surface roughness and density variation of layered materials. It was demonstrated that the combination of GIXRF and XRR was successfully applied for the total characterization of layered materials to determine thickness, roughness, density, and interface diffusion as well as the chemical composition of each layer.

X-ray total reflection has been applied for X-ray photo electron spectroscopy (XPS). Kawai[95] presented a review article on total reflection XPS (TRXPS). Fundamental TRXPS and its applications were described well, referring to almost all papers on TRXPS that had been published before the end of 2009. The most important aspect in TRXPS is the reduction of background intensity in the XPS spectrum, leading to improved surface sensitivity and detection limits.

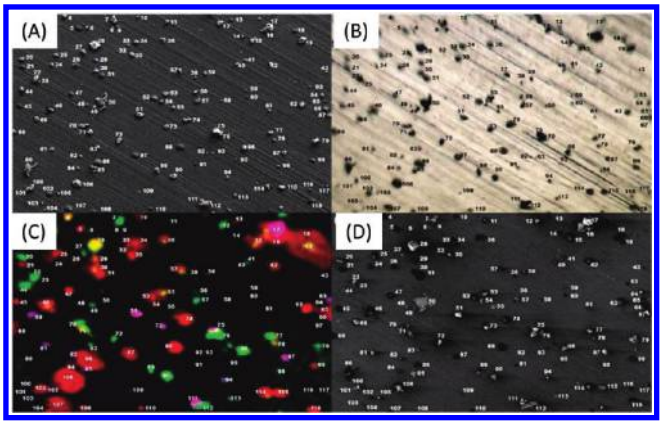

Figure 6. (A) Secondary electron image (SEI) before the ATR-FT-IR imaging measurement; (B) visible light optical image; (C) ATR-FT-IR image; and (D) SEI after the ATRFT- IR imaging measurement of the same 118 individual airborne particles on Al foil. Reprinted from ref 98. Copyright 2010 American Chemical Society.

ELECTRON PROBE MICROANALYSIS

A new quantitative single particle analytical approach using a transmission electron microscope (TEM) with thin-window energy-dispersive X-ray detector (EDX) was published.[96] For single particle analysis using TEM, airborne particles are commonly collected on Formvar/carbon-coated TEM grids containing carbon and oxygen. This carbon and oxygen of TEM grids interferes with quantitative EDX analysis of single particles containing carbon and oxygen such as organics, oxides, carbonates, and nitrates. Their work demonstrated that a Monte Carlo calculation could be used successfully to correct for the interference from TEM grids when the quantification procedure based on the Monte Carlo calculation was applied to a range of standard particles with known chemical compositions. This quantification procedure has great potential for the analysis of particles on substrates. On the other hand, this method has a limitation for electron beam-sensitive particles because TEM employs electron beams with a high voltage and current.

TEM/EDX was used for the spatially resolved quantitative chemical analysis of SiGe structures implemented into high performance complementary metal oxide semiconductor (CMOS) transistors.[97] For rapid and high-quality TEM target specimen preparation, a focused ion beam-based lift-out technique was developed to reduce the postspecimen scatter artifacts during EDX data collection. The initial EDX data acquisition with a quantification standard was performed at a fixed electron beam current, and the dwell time and sampling area were varied to examine the influence of electron irradiation on the microstructure and composition changes in SiGe alloys. Si and Ge signal intensities did not change for small electron irradiation. With the further increase in irradiation, initially, the Si signal then the Ge signal began to decrease, being in good accordance with the thickness variation of the SiGe layer. To avoid beam-induced specimen damage and ensure accurate quantitative chemical analysis, the electron irradiation needs to be kept below a critical

dx.doi.org/10.1021/ac202871b |*Anal. Chem.* 2012, 84, 636–668

value when the TEM is operated at the standard accelerating voltage.

SEM/EDX can provide morphological and elemental chemical compositional information on individual particles. Greater insight on the nature of atmospheric particles can be obtained if additional information on the molecular species of the same individual particles can be obtained. A new analytical methodology that employs SEM equipped with thin-window EDX and an attenuated total reflection FT-IR (ATR-FT-IR) imaging instrument for the analysis of the same individual particles in combination was proposed. These two single particle analytical techniques were claimed to provide complementary information on the physicochemical characteristics of the same individual particles, i.e., SEM/EDX to provide information on the morphology and elemental concentration, and ATR-FT-IR imaging on the functional groups, molecular species, and crystal structure. For example, Figure 6 shows secondary electron images (SEIs) before and after the ATR-FT-IR imaging measurement, visible light optical image, and ATR-FT-IR image of the same 118 individual airborne particles from an ambient aerosol sample.[98] Although the quality of the SEI and ATR-FT-IR images differ due to the inherently different spatial resolutions of the images, the same patterns of the particle location among the images ensures that the same particles of micrometer size can be observed. The morphologies and chemical compositions of all the particles on the image field were first obtained by SEM/EDX. Optical microcopy was used to locate the same image field for the ATR-FT-IR imaging measurements because it could provide an image of sufficient spatial resolution to help locate the same image field observed by SEM/EDX. All the pixels in the ATR-FT-IR image contain the full IR spectra, ranging from 4000 to 720 cm^{-1}. The X-ray and IR spectral data of each particle were used to identify the chemical species. $NaNO_3$-containing, Ca- and/or Mg-containing, silicate, and carbonaceous particles were found to be abundant, even though the internal mixing states of the individual particles were complicated. This study demonstrated that more detailed physiochemical properties of individual airborne particles can be obtained using this approach than when either SEM/EDX or ATR-FT-IR imaging is used alone. This analytical approach was applied to the identification of the mineral types of individual particles, particularly silicate particles, which have many different crystalline forms, such as quartz, feldspar, pyroxene, olivine, mica, and clay minerals.[99] In their study, individual particles from 24 mineral samples were examined to demonstrate that the mineral types of individual particles could be differentiated from their X-ray and ATR-FT-IR spectral data. This single-particle mineralogy has great potential for the unambiguous mineralogical speciation of mineral particles because individual particles with a micrometer size exist mainly as pure mineral forms. For example, six soil samples (two loess and four desert samples), collected from arid areas in China, were characterized using this single-particle mineralogical approach.[100] The most abundant minerals in the loess samples were montmorillonite and calcite, whereas quartz and feldspars were abundant in the desert soil samples, indicating that the source regions of the airborne particles, i.e., loess or desert, could be differentiated clearly by examining the contents of montmorillonite, calcite, quartz, and feldspars of airborne mineral particles collected at the downstream regions during Asian Dust storm events. It was reported that the almost ubiquitous presence of carbonate species in silicate minerals was one of the characteristics of loess soils, suggesting that the reactivity of Asian Dust particles during long-range transport can differ according to the Chinese source soil. This analytical approach will see more applications for the characterization of aerosol, soil, and powder particles in the future.

Since the understanding of the hygroscopic properties of airborne particles is important for examining the characteristic physicochemical changes in aerosol particles, many studies have investigated the deliquescence and efflorescence behavior of aerosol particles using a range of analytical techniques. A new analytical approach for characterizing the hygroscopic properties, chemical composition, and morphology of individual particles was introduced.[101] An optical microscopic technique was used to perform a visual observation of the phase transformation and hygroscopic growth of aerosol particles on a single particle level, and SEM/EDX was used to perform a quantitative chemical speciation of the same individual particles after measuring the hygroscopic properties. They validated the analytical methodology, which was claimed to be simple and easy to apply, by observing the hygroscopic properties of artificially generated, micrometer sized, NaCl, KCl, $(NH_4)_2SO_4$, and Na_2SO_4 aerosol particles, which showed results consistent with those by other studies. The preliminary results on ambient aerosol particles clearly demonstrated how practical this method was for characterizing the hygroscopic properties related to their chemical compositions and how complicated the ambient aerosols were in gaining a full understanding of their hygroscopic properties.

In a quantitative single particle analysis using SEM/EDX, called low-Z particle EPMA, atmospheric aerosols are collected on a substrate, typically a metallic foil, using a cascade impactor. The material used in the collecting substrate can alter the morphology (shape and size) and chemical composition of atmospheric particles through a surface interaction with atmospheric aerosols. This can result in an erroneous interpretation of the real nature of the aerosol particles. In addition, X-rays from the substrate can interfere with the quantitative determination of chemical elements by overlapping with the characteristic X-rays from atmospheric particles. As the choice of optimal substrate material is a critical issue for the successful application of single-particle analysis, three collecting substrates, Ag and Al foils and a TEM grid, were investigated.[102] The morphology and quality of the X-ray spectra for crystalline mineral particles were reported to be similar among the three substrates. On the other hand, water-soluble, CNO-rich aerosols showed different morphologies on the three substrates. The X-ray spectral quality of the CNO-rich particles was optimal for the TEM grid substrate. Appropriate data analysis was required to reliably assess the characteristic X-rays of the CNO-rich particles collected on Ag and Al foils. In particular, the X-ray spectra of the CNO-rich particles collected on the Al foil required a new background subtraction procedure.

In EPMA, surface ionization, $\Phi(0)$, which is a primary parameter for quantitative EPMA, appears explicitly in most analytical parametrizations of the ionization depth distribution, $\Phi(\rho z)$. For bulk samples, $\Phi(0)$ plays an important role particularly when X-ray absorption is important, whereas for thin films and multilayers, the evaluated compositions depend largely on the adopted $\Phi(0)$ values. Although many measurements of surface ionization have been reported, the body of available data is scarce and limited to relatively few tracer−substrate combinations and incident electron energies. In addition, most experimental data has been obtained indirectly due to the experimental difficulties,

which has resulted in a decrease in accuracy with decreasing incident electron energy. Recently, the surface ionization values for several tracer−substrate combinations and a wide range of incident electron energies were reported.[103] The measurements were performed in a direct manner using a tracer technique. Improvements in sample preparation and X-ray measurement methodology enabled $\Phi(0)$ values to be obtained with an uncertainty of ∼2%.

Quantitative X-ray microanalysis of thick samples is normally performed by measuring the characteristic X-ray intensities of each element in the samples and corresponding standards. Under optimal conditions, the quantification accuracy can approach 1%. On the other hand, all experimental conditions must remain the same during the sample and standard measurements, which is not possible with cold FE-SEM, where the beam current can fluctuate by ∼5% in its stable regime. To address this problem, a new method using a single spectral measurement was developed.[104] The proposed method employs the ratio of the intensity of a characteristic X-ray normalized by the sum of the X-ray intensities of all elements measured for the sample. The uncertainties in the physical parameters of X-ray generation were corrected using a calibration factor that must have been previously acquired or calculated. Relative accuracies better than 5% were obtained when this method was used to calculate the composition of the Au−Cu standards and measured by cold FE-SEM.

EPMA has been used to examine solid-state diffusion in materials. The concentration profiles measured by EPMA on a polished cross-section can be much smoother than the real profile when the diffusion distance is <1 μm, which is smaller than the analysis volume. This is due to the probe size effect, which can create difficulties in determining the diffusion coefficients. Christien et al.[105] reported a new methodology for a study of interdiffusion between two miscible metals. The technique, which was based on a modeling of interdiffusion kinetics, was applied to the Ni−Pd system where the change in apparent surface composition of a Pd substrate coated with an 800 nm Ni thin film during annealing at a given temperature was measured by ED-EPMA. The experimental data was processed using a model, allowing a determination of the mean interdiffusion coefficient at a given annealing temperature. The main advantage of the technique is the possible determination of interdiffusion coefficients in thin films and at very low temperatures (down to 430 °C), which is not achievable employing other techniques used conventionally for examining interdiffusion.

Quartz occurs in a wide range of geologic environments throughout the Earth's crust. The concentrations and distribution of trace elements in quartz, such as Ti and Al, provide information on the temperature and other physical conditions of quartz formation. Trace element analysis with modern WD-EPMA instruments can achieve ∼100 ppm detection for elements in oxides and silicates. On the other hand, detection limits below several tens ppm are needed for trace analysis in quartz. A newly developed technique was reported to improve the detection limits with good accuracy for WD-EPMA of many trace elements in quartz.[106] In their approach, models were implemented to fit the shape of the background, followed by the utilization of new quantitative "blank" correction routines to improve the background determination accuracy. In addition, a new counting method using multiple spectrometers improved the geometric efficiency for better detection limits, resulting in a detection limit of 2 to 3 ppm for Ti and 6 to 7 ppm for Al at the 99% confidence level.

The reliability of trace element analysis by WD-EPMA can be improved significantly using high quality secondary standards. In the case of Au residing in sulfides, such standards were not available because natural materials have a heterogeneous Au distribution and their synthesis is difficult. The benefits of the use of ion implants as trace-element RM for EPMA were assessed by characterizing grains of magnetite, pyrite, and galena implanted with Au atoms at energies from 1 to 3 MeV.[107] Good lateral micrometer-scale homogeneity of the Au levels across the implants was obtained. In addition, the Au X-ray intensities measured by EPMA showed a good correlation with those predicted for multilayered structures. These results suggest that ion implants might be used for the preparation of RM for EPMA, particularly in cases where natural and synthetic standards are unavailable.

Image acquisition by SEM and chemical characterization by EDX of samples with a low electrical conductivity can have the problem of charge build up, which affects the generation of secondary and backscattered electrons and the excitation of characteristic X-rays. In this case, it is normal to apply a conductive coating to avoid the charge effect and reduce the sample heating. The effects related to the attenuation and deflection suffered by an electron beam when it passed through a carbon conductive coating and an oxide film layer on the surface of the bulk samples were studied by Monte Carlo simulations, where the fraction of energy lost by the incident electrons in the surface layers, the fraction of transmitted electrons, and the mean deflection angle were evaluated.[108] From the simulated data, analytical expressions were obtained for the three parameters as functions of the incident beam energy, mass thicknesses, and atomic numbers involved. From these analytical expressions, corrections were proposed for the models, which were used to describe the contribution of the X-rays generated in the oxide and conductive films as well as the characteristic X-ray absorption occurring in those layers. The spectral modeling was tested with the experimental spectra of the Mg and Si standards. The measured spectra were fitted properly when all the discussed effects were considered.

With the advent of fast computers and affordable memory storage, the utilization of Monte Carlo simulations in quantitative EPMA has become a practical tool. Monte Carlo-based quantification methods can be used for samples with complex geometries, such as porous materials. Previous experimental studies reported that an increase in porosity led to a deficit in X-ray emission for a range of materials, such as graphite, Cr_2O_3, CuO, ZnS, Al_2O_3, and Ag. On the other hand, the mechanisms responsible for this decrease are unclear. As the porosity itself did not explain the loss of intensity, other mechanisms were proposed, such as extra energy loss by the diffusion of electrons by the surface plasmons generated at the pores−solid interfaces, surface roughness, extra charging at the pores−solid interface, or carbon diffusion in the pores. A new approach using Monte Carlo simulations was developed to better understand the effects of porosity on quantitative microanalysis, where the X-ray emission model was modified to include a random log-normal distribution of pores size in the simulated materials.[109] The simulation results showed that fewer X-rays were generated in the porous material if the energy loss at pore interfaces associated with the plasmon was added. When compared with the experimental results, the addition of a log-normal distribution of pores improved the simulated values. Nevertheless, further improvements in the model will be needed to obtain a proper match.

PARTICLE-INDUCED X-RAY EMISSION

PIXE experiments are performed using EDX, which has the advantage of high efficiency and simultaneous multielement detection. Recently developed SDDs work with Peltier cooling without the use of liquid N_2, leading to a compact EDX with easy maintenance. However, the energy resolution of EDX is on the order of 140 eV. This energy resolution is sufficient for distinguishing elements by measuring K peaks. However, the L peaks of high-Z elements overlap the K peaks of low-Z elements in which case the energy resolution of EDX is not sufficient. In contrast, a wavelength-dispersive spectrometer (WDS) has a high-energy resolution of about a few tens of eV. Thus, PIXE with WDS was studied.[110] The previously constructed Johansson-type WDS was applied for high-resolution PIXE analysis. The energy of the proton beam was set to 3 MeV with a current of 2.7 μA. A Si (111) crystal was used in Johansson geometry with a 500 mm Rowland circle radius. The diffracted X-rays were detected by an X-ray CCD camera with 22.5 × 22.5 μm^2 pixel size. The detection limits of Pd and Cd with the Ag matrix were 39.8 and 61.0 ppm, respectively, while the detection limit of Pd in Ag obtained by conventional (standard) PIXE was 1140 ppm. Another research group discussed various compact WDS-PIXE spectrometers based on the results obtained by a numerical X-ray tracing procedure.[111] The possible spectrometers in geometries with flat, Von Hamos, Johann, Johansson, and spherical crystals were evaluated under different geometrical values.

A high-energy resolution PIXE spectrum was obtained using a microcalorimeter-based EDS.[112] A POLARIS microcalorimeter (VeriCold Technologies GmbH, Germany) was applied at an operating temperature of 125−140 mK. A proton beam of 1.0 MeV was irradiated in an area of 3 mm in diameter on a polished agate sample. Using this setup, radiative auger emission (RAE) satellites were observed as well as Si K lines. Microcalorimeter will be useful not only for studies of RAE transition but also for studying chemical shifts observed in XRF spectra.

PIXE analysis was applied for the evaluation of the analytical performance of a polycapillary focusing X-ray lens.[113] PIXE measurement was performed using the external scanning microbeam facility of the 3MV Tandetron accelerator. A 3-MeV proton beam was focused to about a 30 μm spot size on the sample. The polycapillary lens (by IfG GmbH, Germany) was coupled to a SDD (10 mm^2 active area, 450 μm thick, PNSensor, GmbH, Germany). It was confirmed that the spot size for collection depended on the energy of the X-rays. Low energy X-rays were collected from a large area on the surface of the sample.

A confocal micro-PIXE has been developed using polycapillary optics for detection of characteristic X-rays.[114] 3 MeV protons were focused on a 1.5 × 1.5 μm^2 area. A polycapillary half-lens was mounted on the Si(Li) detector (10 mm^2 active area) and then arranged in a confocal configuration. 3D elemental images were successfully reconstructed for hematite particles in a volume measuring 100 × 40 × 100 μm^3. The authors pointed out that the limitation of the present setup originated from the properties of a polycapillary lens, which has a large spot size compared to the size of the proton beam. 3D imaging was performed by PIXE micro-CT.[115] The principle is the same as X-ray CT. A microbeam (3 MeV protons) was bombarded on a metal target such as Ti with a beam size of 1−4 μm. X-ray emission (Ti Kα) from the target was used for the CT. The sample (living Drosophila) was placed at the top of a rotating stage that is 1.57 mm away from the target. The CCD camera was placed 5.5 mm from the target. This configuration provided a magnification of 3.5×. The spatial resolution of the image was about 6 μm. Elemental images are expected with this resolution. In addition, comparison with conventional X-ray CT will be required.

PIXE analysis was performed at an incident angle of 87° for the proton beam, corresponding to a glancing angle of 3°.[116] The sample was rotated to adjust the incident angle of the proton beam. Characteristic X-rays were detected by a Si-PIN detector at a detection angle of 135°. This experiment is closely related to the previous study on total reflection PIXE (TPIXE), which is found in the following article: Vis, R. D.; van Langevelde, F. *Nucl. Instrum. Methods Phys. Res., Sect. B* **1991**, *61*, 515−521. Under the glancing incident condition, surface sensitivity was improved with a reduction of background intensity. Finally, the detection limit of As that existed on the surface of the Si wafer was improved to 1 × 10^{12} atoms cm^{-2}.

PIXE analysis has been used in combination with other related techniques. Pichon et al.[117] reported on recent activity at the AGLAE facility of the Louvre Laboratory. The recent experimental setup enables the simultaneous performance of PIXE, PIGE, and RBS on the same analyzed spot with a proton beam of about 20 μm in diameter. New software was developed to control the sample stage and acquisition of PIXE, PIGE, and RBS spectra to obtain elemental maps for the samples such as objects of cultural heritage. In this paper, PIXE and RBS mapping was performed to characterize the pigments on a prehistoric rock painting. Elemental maps of C and O as well as other typical elements such as Fe, Ca, P, and S were shown. At the Surry Ion Beam Centre in the UK, PIXE and RBS were used simultaneously with TOF-SIMS.[118] The multi-ion beam techniques were performed with a focused and scanning MeV primary ion beam to provide complete elemental and molecular information regarding the surface of the sample. PIXE and RBS gave elemental distribution and depth profiles, while TOF-SIMS provided molecular data relative to the surface of the sample. Although the combination of multianalytical methods will give detailed information for samples, we must remember that each technique has essentially different analyzing depths in the sample.

X-RAY ABSORPTION SPECTROMETRY

XAS or X-ray absorption fine structure (XAFS) spectroscopy is a method that provides physicochemical information on the target element, such as the oxidation state, coordination symmetry, and local structure around the atom (e.g., interatomic distance and coordination number to the neighboring atoms). XAS can be divided into two regions, namely, X-ray absorption near-edge structure (XANES) and extended X-ray absorption fine structure (EXAFS), which originate from different physicochemical mechanisms. However, the two structures can be simultaneously obtained in one spectrum, from which we can obtain abundant information from one XAS spectrum. Although the method has been used for more than 30 years, research fields utilizing XAS are still expanding from physics, chemistry, and material sciences to biology (mainly in metal protein studies), earth and environmental science, and art conservation sciences, as reviewed in a recent book,[119] special issues of journals,[120,121] and review articles in catalytic[122,123] and biological[124] sciences. This highly convenient method is useful because of (i) its

dx.doi.org/10.1021/ac202871b |*Anal. Chem.* 2012, 84, 636–668

applicability to any element (except for H, He, Li, and Be for practical reasons), (ii) element selectivity to obtain the spectra without interferences from other elements, (iii) its application potential to various types of samples (solid, liquid, and even to gas), (iv) its abundant information on the chemical species and local structure, and (v) its simple analytical principle, also aided by (vi) the recent increase in the number of SR facilities in the world, where most XAS experiments are conducted.

More than 1000 papers per year can be searched by the keyword EXAFS, XANES, or NEXAFS (the term often used for XANES in the soft X-ray region for lighter elements, such as C and N) in the Web of Knowledge (Thomson Reuters) in the past 10 years, and the number is still increasing. The high photon flux of the X-ray beam available in many recent SR beamlines has facilitated the potential of XAS in smaller spatial resolution, quicker time resolution, and new techniques such as 3D imaging, the pump−probe technique, and complex combination with other methods (e.g., various X-ray scattering and diffraction (XRD) methods). In this section, we review recent advances in XAS and related methods with some developments in the calculation of XAS and application studies.

XAFS theory has continuously advanced based on many-body effects, quantum field theory, single- and multiple-scattering theory with vibrational effects, inelastic losses, and multielectron excitations.[119] These advances in the theory, often driven by experimental demand, have been introduced into practical data interpretation through the development of computer programs. For example, FEFF9, a new version of the FEFF code widely used for EXAFS and XANES analyses, has been released. Its features were summarized in the study of Rehr et al.[125] A real-space Green's function approach has been developed for calculation of XAS spectra, focusing on parameter-free models for many-body effects, which improved the expression for inelastic losses, multielectron excitations, and Debye−Waller factors. The theoretical estimates of various parameters available in the code can contribute to the better simulation of EXAFS and XANES spectra. In addition, FEFF9 can be employed for calculations in nonresonant inelastic X-ray scattering (NRIXS) and electron energy-loss spectroscopy (EELS).

A program, called CTM4XAS or Charge Transfer Multiplet, was described by Stavitski and de Groot.[126] The program can be used for the analysis of transition metal L-edge XAS and EELS. The program is based on a semiempirical approach including the interactions of the core hole potential, core hole spin−orbit coupling, core hole-induced charge transfer effects, core hole −valence hole exchange interaction, and core hole−valence hole multipole interactions. The symmetry options are restricted to octahedral and tetrahedral, whereas the magnetic field direction is limited to the *z*-axis. Two electronic configurations, $3d^n$ and $3d^{n+1}\underline{L}$, are included, which cover most of the systems dealt with in the 2p XAS spectra of transition metal ions. This program has been frequently used in various studies and can be found in the Web site http://www.anorg.chem.uu.nl/CTM4XAS/index.html.

In experimental studies, major advances in XAS measurements have been the achievements in time and spatial resolution capabilities. In the time-resolved analysis, the ultrafast detection of XAS has been developed to understand the mechanism of chemical reactions, including the breaking, creation, and evolution of interatomic bonds. As summarized by Johnson and Milne,[127] the basic idea of the ultrafast method is to use the pump−probe method (mainly applied to reactions in solution), which consists of irradiation by an optical or infrared laser

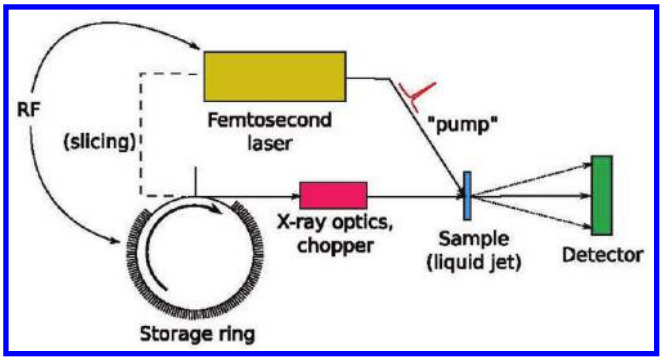

Figure 7. Schematic of synchrotron radiation beamline with ultrafast pump−probe method. A radiofrequency (RF) clock determines the pulse timing of both the storage ring and an optical laser system. A "pump" pulse generated by the laser system triggers some reproducible dynamics in a liquid-phase sample. To probe the dynamics of the sample at particular times after the pumping, short pulses of X-rays generated by SR are directed onto the sample. For femtosecond slicing beamlines, the X-ray pulse used is created by the interaction of a portion of the optical laser output with the electrons in the storage ring. Reprinted from *TrAC, Trends Anal. Chem.*, Vol. 29, Johnson, S. L.; Milne, C. J., Ultrafast X-ray scien structural transients in solution, 497−507, Copyright 2010, with permission from Elsevier.

pumping, followed by an X-ray pulse for XAS measurement used as a probe. Picosecond time resolution is achieved by the time difference between the initial pump pulse by lasers and probe pulse by X-rays. In a storage ring in the SR facility, the electrons which produce the SR travel in bunches which are typically tens of picoseconds long, so the SR is naturally pulsed. Special modes of operation in some rings allow shorter bunch lengths at the cost of reduced current. Another system with even higher temporal resolution is the femtosecond pump probe employed on the basis of the electron-beam slicing scheme, which is shown in Figure 7. A disadvantage of the slicing source is the reduced photon flux caused by the slicing. Thus, the use of FELs has been proposed to achieve high X-ray pulse flux and temporal resolution of 10−100 fs. Energy-recovery linacs (ERL) can be another possibility for short X-ray pulses with high brilliance and high repetition rate.

Ferri et al.[128] utilized time-resolved measurement coupled with modulation excitation, where periodic change was introduced, such as switching the gas flow between NO/He and CO/He in a heterogeneous catalytic system. In the system, the time-resolved spectra can be transformed into phase-resolved spectra for the element of interest in the catalyst. The advantage of this method, especially when employing energy-dispersive XAS, is its sensitivity to detect subtle changes during the switching of the gas between NO and CO, because other physicochemical conditions could be kept identical in the two conditions during the switching of the gas. Other parameters, such as temperature, pressure, and so on, can be changed as the modulation-excitation factors.

In catalysis studies, the term in situ spectroscopy is well established and widely used in the catalysis literature, but operando spectroscopic methodology has been introduced into the catalysis literature to express a methodology that combines simultaneous in situ spectroscopy and kinetic measurements on the same sample and time. There has been lots of effort to do operando measurements including preparation of gas lines at XAS beamlines in various SR facilities for the study of catalytic reactions. For example, Bauer et al.[129] developed a beamline combining time-resolved X-ray absorption spectroscopy with

UV/vis spectroscopy for the study of homogeneous reaction. For this purpose, they made a measurement cell which has variable path lenghs of the optical and X-ray beam to record simultaneously absorption spectra at UV−vis and X-ray regions. The technique was applied to various systems such as in situ reduction of cerium(IV) ammonium nitrate to cerium(III) by isopropanol.

Various types of 3D imaging with XAS have been tested, one of the methods was to use a confocal detection system. In the conventional 2D method of mapping and taking XRF and XAS data, the fluorescence detected comes from a cylindrical volume whose width is that of the probe beam and whose length is determined by the absorption depths of the incident and fluorescent radiation, which could be several micrometers. Thus, to confine the zone represented by the data, one usually makes thin sections of the sample. Confocal methods employ additional optics on the detection side to define a detection probe which intersects the incident probe beam, so that the detected signal comes from a specific depth in the sample. The detection probe may be defined using a single capillary or polycapillary feeding into the detector. In the study by Silversmit et al.,[130] the method was applied for Fe speciation in an inclusion in diamonds that are assumed to be transported from deep earth with the information of the redox state in the mantle. To keep the oxidation state of Fe in the diamonds, its speciation must be measured by keeping the Fe under the original condition. Thus, the 3D speciation of Fe by confocal detection is ideal for this purpose, achieved by mounting a polycapillary half-lens (focal distance: 2.1 mm) on the energy-dispersive detector. In the experiment, the dimensions for the ellipsoidal confocal detection volume were calculated to be $21 \times 26 \times 17\ \mu m^3$. This volume is not considered a very high spatial resolution, but this method is useful for ascertaining the chemical species in small materials incorporated into the light-element matrix, such as Fe particles in diamonds, as done in their study.

Cotte et al.[131] used a similar detection system using polycapillary optics for the micro-XRF measurement of various elements in artists' materials. The analysis was an inherently 3D imaging method but was noted as the WDS system for the quasi-parallel beam of XRF generated by the polycapillary optics. Such a WDS system is needed for XRF imaging between 2 and 13 keV because the L lines of heavier elements overlap with the K line of lighter elements, often encountered in multielement systems such as natural samples and artists' materials. In particular, the system in the study can choose either a single-crystal or a double-crystal setup for the XRF detection. Although the count rate can be reduced by a factor of 30−40 in the double-crystal mode, the system can provide better contrast for selective mappings of the element, as well as high-resolution XANES spectra. In this double-crystal system, the instrumental energy resolution is below the natural lifetime broadening, showing that this experiment is actually microresonant inelastic X-ray scattering (RIXS) analysis of the material.

A more conventional method in 3D-XAS is based on the measurement of transmission X-ray microscopy (TXM) using a high-resolution CCD to obtain tomographic images at different incident energies, which have submicrometer spatial resolution. Each 3D mapping image at a certain energy is collected as a series of transmission images over a 180° rotation range in 1° increments (exposure time duration at each point is several seconds). Nelson et al.[132] applied the method to 3D mapping of the nickel oxidation state in a solid oxide fuel cell, where the nanotomographic images were taken at 2 eV steps within the XANES region of the target element. This method is capable of mapping an element in different oxidation states incorporated into the material. By this technique, the redox change of metal ions in the solid oxide fuel cell, battery electrodes, and so on can be observed.

A similar object, a solid-state battery, was examined by depth-resolved XAS by Okumura et al.[133] This method is effective for samples in columnar dimension with a flat surface, where the surface of the sample is exposed perpendicular to the incident X-rays. The XRF emitted from different depths of the surface was measured by a 2D detector located beside the sample. The signals detected at lower angles (or close to the surface) are only from the vicinity of the surface because those from the deeper part of the sample are absorbed by the sample itself. The relative intensity of the signals from the deeper part is larger at higher angles. The depth resolution by the method can be submicrometer level. For this type of sample, a nondestructive and depth-resolved analysis is essential to observe the redox change during the discharge or recharge of the battery by the method shown here.

Depth-dependent information can also be obtained by grazing-incidence XRF combined with NEXAFS spectroscopy (GIXRF−NEXAFS), as shown by Pagels et al.[134] This method is applied to layered materials based on the total reflection at a buried layer. A beam with the angle of the incident beam higher than the critical angle of the surface layer can penetrate into the material. If the angle is also higher than the critical angle for the buried layer, the XRF is emitted both from the surface and from the buried layers. However, if the angle is lower than the critical angle of the buried layer, the XRF information is limited to the first layer and the interface of the buried layer. The present study applied the method to a ZnO sample overlaid by a Si layer. In this case, the two XAS measurements at the Zn $L_{III,II}$ edges above and below the critical angle revealed selective chemical change of Zn at the surface of the buried layer. This method can be applied to layered materials when the density of the upper layer is less than that of the second (buried) layer.

Combining various methods often opens new fields in analytical sciences. In particular, Polte et al.[135] combined two methods, XANES and small-angle X-ray scattering (SAXS), which are practically available at SR facilities. Compared with XANES or XAS containing atomic-scale speciation information, SAXS yields information about larger (nm−μm) length scales, such as (i) the shape and size of the particles and macromolecules and (ii) the polydispersity and the number of particles formed. The current study used the method to clarify the formation process of gold nanoparticles (GNP) in a classical synthesis method; that is the reduction of tetrachloroauric acid by trisodium citrate. For this purpose, in situ and time-resolved data of SAXS and XANES were simultaneously obtained using an acoustic levitator to hold the sample in a micro-X-ray beam. A four-step mechanism for the formation was proposed for the GNP in the present study: fast initial formation of small nuclei, coalescence of the nuclei into bigger particles, slow growth of particles, and fast reduction ending with the consumption of the precursor species. The acoustic levitator was important in the study as a sample holder to keep the sample in droplet form, but such an elaborate sample holder is not always necessary for more general use of this technique. The combination of SAXS and XAS is powerful and can be applied to various fields because the two methods provide complementary information for macromolecule and particle samples.

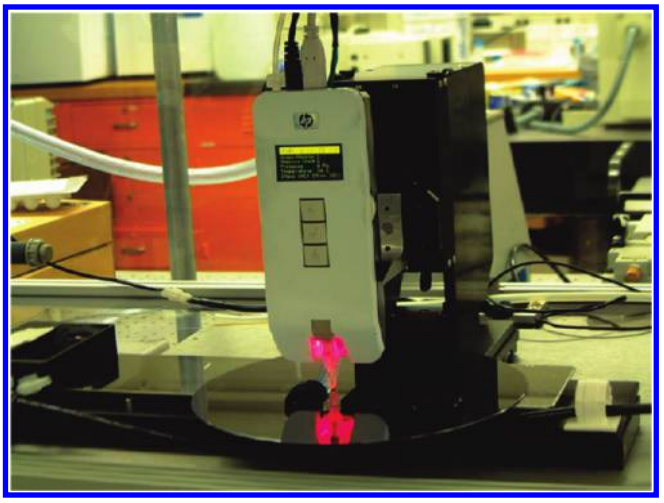

Figure 8. Thermal inkjet pico-fluidic system (TIPS) jetting on a 200 mm Si wafer. The system is mounted on an *X*, *Y*, and *Z* stage inside of a humidity controlled chamber. This photograph shows the printer head, which is also the reservoir (150 μL) for the standard solutions and can be exchanged easily. Reprinted from ref 136. Copyright 2010 American Chemical Society.

APPLICATIONS

Sample Preparation. One of the great advantages of XRF is that it enables nondestructive and direct measurement for screening without complicated sample preparation procedures. However, suitable sample preparation with a sample matrix of actual samples can allow performance of an accurate quantitative analysis of trace elements at less than ppm levels.

The small-volume droplet technique is a recent trend for preparing liquid samples for micro-XRF or TXRF analysis. For application in micro-XRF analysis based on thermal inkjet technology, Fittschen and Havrilla[136] studied dried deposits of picoliter droplets using a prototype picoliter pipet, as shown in Figure 8. The "thermal inkjet picofluidic system" (TIPS) generates small-volume droplets ranging from 1 to 300 picoliters and 1 to 2000 pg elemental deposits with a precision of less than 10%. Characterization of the dried residues evaluated by light microscopy and AFM showed diameters from 5 to 50 μm and heights from 100 nm to 3 μm for a Ni amount from 2 pg to 2000 pg. The diameter of the dried residue showed a logarithmic relationship with the deposited amount.

Yonezawa et al.[137] developed a sample preparation method for the XRF analysis of trace elements in suspended particulate matter. Calibrating standards for the suspended particulate matter were prepared as follows. A 47 mm diameter polycarbonate filter was leached with a diluted surfactant solution and dried at 50 °C for a few minutes. The dried filter was cut into a 10 mm diameter for XRF measurements. A 100 to 200 μL volume of aqueous standard solution containing specific amounts of 15 elements was dropped on the center of the filter. The calibration curves measured by a 3D-polarizing ED-XRF spectrometer showed good linearity with the correlation coefficient (R^2) of 0.9491 to 0.9999 for S, K, Ca, Cr, Mn, Fe, Xu, Zn, and Pb. The DL values for S, Zn, and Pb were found to be 3.6, 1.0, and 3.5 ng/cm^{-2}, respectively. Good matches were observed between the obtained calibration curves and those prepared from air particulate standard reference materials (NIST SRM 2783).

A preconcentration technique is often used for quantitative determination by XRF of environmental water because the detection limits for metals by a typical XRF spectrometer are levels of approximately several ppm to several tens of ppm, whereas many toxic elements in environmental water are regulated at concentration levels of ppb. Heiden et al.[138] investigated a preconcentration procedure using Amberlite IRC748 ion-exchange resin for transportable XRF analysis of environmental water samples. Optimum recovery conditions of the ion-exchange resin including flow rate, resin amount, and resin chemical form were investigated for the suitable preconcentration conditions. The recoveries of elements obtained under the optimum conditions (a flow rate of 4.0 mL/min, 15 mL of elute, and 4.0 g NH_4-form resin) were 96.2% for Zn, 93.3% for Pb, 84.9% for Cu, 72.2% for Ni, and 68.1% for Fe. The method was tested with extracts from landfill soil and surface water from a derelict base metal mine. The method recovered Cu, Zn, and Pb accurately, and Ni and Fe at concentrations satisfactory for screening purposes.

Inui et al.[139] developed a simultaneous preconcentration method of Cr(III) and Cr(VI) in water samples using an ion-exchange resin disk for WD-XRF measurement. In the proposed method, a 100 mL water sample was first adjusted to pH = 3 with nitric acid and then passed through an anion-exchange resin disk placed on top of a cation-exchange resin disk at a flow rate of 1 mL min^{-1} to separate Cr(III) and Cr(VI). Anionic Cr(VI) was preconcentrated on the upper anion-exchange resin disk, whereas cationic Cr(III) was preconcentrated on the lower cation-exchange resin disk. Each ion-exchange resin disk was dried at 100 °C for 30 min in an electric oven and coated with a commercially available laminate film in order to prevent damage from X-ray irradiation with a WD-XRF spectrometer. The calibration curves of Cr(III) and Cr(VI) showed good linearity in the range of 1−10 μg. The DL values corresponding to three times the standard deviation (n = 5) of blank values were 0.17 μg for Cr(III) and 0.16 μg for Cr(VI). The results indicate that, if a 1 L water sample is used, these limits would be subppb levels. A spike test for 50 μg L^{-1} Cr(III) and Cr(VI) in tap water and river water showed quantitative recoveries (94−114%).

Standards. Standard materials are essential tools for quantification in XRF analysis. Various standard materials in steels, metals, ceramics, rocks, water, and environmental samples are used for XRF analysis. Recently, the list of certified standards for hazardous trace elements for XRF analysis has grown since the European Union (EU) enforced the RoHS directive as set out in Directive 2002/95/EC.

The Japan Society for Analytical Chemistry (JSAC; Japan) has developed a series of four certified reference materials (CRMs) for XRF analysis of Ag, Cu, Pb, and Cd in lead-free solder alloys formulated from Sn, Cu, and Ag, named JSAC 0131-0134.[140] Candidate reference samples were prepared by adding appropriate amounts of Ag, Cu, Pb, and Cd to a molten tin or molten solder and then casting the mixture in a box-shaped stainless mold. In order to prevent oxidations within the process of fusion, the surfaces of the samples were covered by a reducing agent of carbon powder. In addition, in order to make a fine metallographic structure, the samples at fusion were quickly cooled by water. Both surfaces of the prepared alloy plates were removed from the mold and ground and polished by a milling machine to a thickness of 2.0 mm. Finally, the plated samples were clipped into a 30 mmϕ × 2.0 mm cylindrical disk. The homogeneity of the prepared alloy disks was shown to be excellent. The certified

dx.doi.org/10.1021/ac202871b |*Anal. Chem.* 2012, 84, 636–668

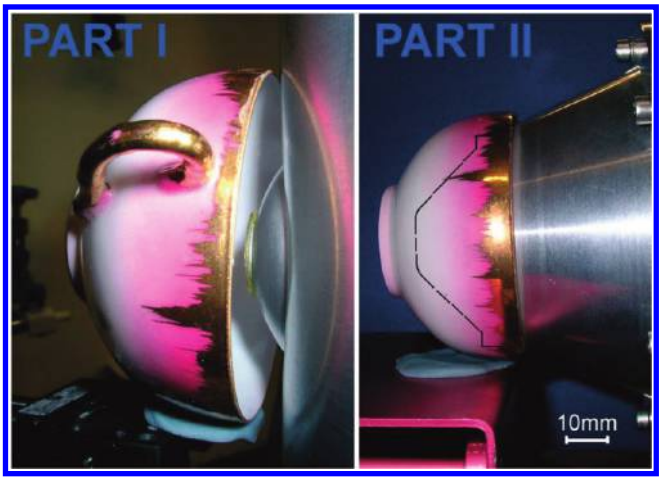

Figure 9. Accessibility of the previous (called PART I) and new (PART II) instruments showing the spectrometers in front of a tea cup and a sketch overlaid with the shape from PART II. Reprinted with permission from Buzanich, G.; Wobrauschek, P.; Streli, C.; Markowicz, A.; Wegrzynek, D.; Chinea-Cano, E.; Griesser, M.; Uhlir, K. *X-ray Spectrom.* **2010**, *39*, 98−102. Copyright 2010 John Wiley & Sons, Inc.

values were evaluated by statistical analyses of the results of an interlaboratory comparison study from 20 laboratories. The certified values evaluated by the interlaboratory comparison study ranged from 0.488 to 3.91 wt % for Ag, 0.102 to 1.01 wt % for Cu, 13.9 to 2007 mg/kg for Pb, and 0 to 1530 mg/kg for Cd.

Patterson and Hamilton[141] prepared a dimensional standard for the X-ray micro-CT. Dry borosilicate glass microspheres having a diameter of 20 μm embedded in polystyrene were used as the raw material for the 3D size standard. The 20 μm microspheres have a certificate of analysis (NIST traceable); they are 17.3 $\pm$ 1.4 μm in diameter with a 12% relative standard deviation. The standard was prepared as follows. Approximately 100 mg of the glass microspheres dispersed in 8 mL of water containing $K_2S_2O_8$ was mixed into a polymerization solvent. The mixture was polymerized at 60 °C overnight. Then, water, catalyst, and emulsifier were removed by Soxhlet extraction. The prepared standards were evaluated by a micro-CT instrument. A 10 W tungsten X-ray source can generate broad-spectrum X-rays from 40 to 150 kV, with a 5 μm spot on a target and a 43° cone-shaped X-ray. The total number of radiographs collected included data sets of 181, 361, 721, and 1261 images. The diameter of the microspheres as a function of the number of radiographs was calculated using a commercial software package, AvizoFire. The prepared dimensional standards showed good homogeneity, and the calculated diameter of the microsphere by 3D micro-CT was in good agreement with the certificate value. Tsuji and Nakano[69] proposed a 3D-structured standard material for evaluating 3D-imaging performance. This 3D-standard pattern consists of two Au cylindrical patterns, which were made by an electroplating technique on SiN film in a diameter of 95 μm and a height of 29 μm. These dimensions were measured by a surface profiler. Then, the Au cylinders were embedded in a polymer resin with a thickness of 100 μm. The lateral distance separating the two Au patterns was 182 μm, and the vertical distance was 71 μm. This 3D structured material was evaluated by nondestructive depth analysis of the cross section using two confocal 3D-XRF spectrometers having different depth resolutions. The Au elemental maps obtained by two instruments showed clear and blurred maps caused by the difference in depth resolution of the two instruments. This indicates that this kind of 3D-standard pattern is useful for checking the imaging performance of 3D-XRF instruments.

EDS. A previously developed portable XRF spectrometer (called PART I) that enables in situ analysis of nontransportable, highly valuable objects without any restrictions on the object size was improved into another portable XRF spectrometer (called PART II) to better meet the special requirements of various types and shapes of artworks.[142] The new spectrometer was equipped with a vacuum chamber enclosed with a Kapton-window that allowed the detection of chemical elements from Na upward, thereby enabling the characterization of glass and enamel objects. Two low-power X-ray tubes, one with a Mo-anode and the other with a Cr-anode were used as the excitation source. A polycapillary lens with a spot size of 150 μm was used to focus the primary beam to access the small details of different objects, e.g., fine brush strokes in paintings. The spectrometer was designed to maximize the accessibility to all parts of the objects investigated through the use of translation stages and an innovative design of the detection head. Figure 9 shows the capability of the PART II spectrometer to reach the measuring positions in the concave parts of objects, and the PART II instrument has higher accessibility than the PART I instrument.

Migliori et al.[143] reported a portable ED-XRF instrument with high efficiency for a wide range of elements from Na upward. For the instrument equipped with two different X-ray tubes, a continuous helium flow in front of the tubes and detector was used to enhance the transmission of both the primary and characteristic X-rays. Efficiency curves were obtained from an analysis of thin standards, and minimum detection limits were obtained for some elements in a thick target of medium-low density matrix, showing a good performance. The range of elements that could be detected efficiently was extended and low-Z elements (down to Na) could be identified with a good sensitivity.

In situ micro-EDXRF analyses of several glazed ceramic pieces, originally produced in Coimbra (Portugal), were carried out to obtain some chemical and physical data on the manufacture of faiences in Coimbra.[144] A portable micro-XRF unit equipped with a capillary X-ray lens, a new generation low power microfocus X-ray tube, and a drift chamber detector with a few tens of μm lateral resolution enabled proximal different pigmented areas and the glaze itself to be distinguished. The pigment analysis of the collection of faiences indicated the presence of a unique production center with its own techniques and raw materials, which were inferred from the identification of blue and yellow pigments with Mn, Fe, Co, and As and Pb and Sb, respectively. The use of a polycapillary lens in the EDXRF portable equipment was demonstrated to be useful for a study of the colors, ornaments, and contours in these glazed ceramic pieces. A portable EDXRF was used as a screening tool to determine and compare the pigment use in a large series of paintings by the Belgian artist, James Ensor.[145] A large number of paintings were analyzed, allowing a systematic and comparative study of the pigments used by a single artist over his entire career. The establishment of a large database of inorganic pigments became possible, which can be expected to open new prospects in the field of (technical) art history and painting conservation. Regardless of the many restrictions due to the setup and/or the analytical method, it appears feasible to document the evolution

with time in Ensor's use of inorganic pigments and to correlate this technical evolution with stylistic developments.

In the late nineteenth and early twentieth century, photographers experimented, adapted, and combined different techniques using a wide array of chemicals to produce a vast range of commercial and self-made photographs. Museum professionals, experts, and collectors typically rely on visual and microscopic examinations to identify different photographic processes, but a visual identification alone can be misleading. Portable and hand-held XRF spectrometers were used to determine the metallic elements in photographic images, with particular focus on the Alfred Stieglitz photographic collections.[146] A protocol was developed for the two types of XRF spectrometers and was validated using standard replicas of known photographic techniques. Qualitative XRF identification of the metallic salts allowed an unambiguous identification of the process used for each photograph. The correct identification of these photographs is expected to have a significant impact on the aspects of preventive conservation, exhibition, and scholarly research.

A portable EDXRF spectrometer was used for the in situ analysis of rock art pigments from the Saltadora rock shelters (Valltorta gorge, Castellon, Spain).[147] The results revealed the presence of calcium in all the locations analyzed due to the contribution of the underlying calcareous bedrock and overlying crust. Iron and manganese were the main elements detected in the red and black pigments, respectively. The iron to calcium ratio was found to be indicative of the degree of preservation of the pictorial layer. Traces of manganese were detected in some red pigments, indicating the use of iron oxides from different sources as well as the probable intentional addition in one of the figures. EDXRF spectrometry proved to be a useful technique for detecting the chemical elements present in prehistoric rock art pigments and identifying the different raw materials used in their production process. Approximately 50 metal objects from the Moche civilization were analyzed using a portable EDXRF.[148] The Moche civilization flourished on the north coast of present-day Peru between approximately 50 and 700 AD and was a highly developed culture that produced sophisticated metal objects. Standard samples of gold and silver alloys were employed for calibration and quantitative determination. The artifacts analyzed were mainly gold, silver, and copper alloys, gilded copper, and tumbaga. The composition of the gold, silver, and copper alloys was determined using standard alloys. In the case of gilded copper and tumbaga, the Cu−Kα/Cu−Kβ and Au-Lα/Cu−Kα ratios, respectively, were determined, first to clearly distinguish gilded copper from tumbaga and then to determine the gilding thickness or "equivalent gilding thickness" in the case of tumbaga. A combination of the two ratios was a clear indication of the nature of the alloy (gold, gilded Cu, or tumbaga) and allowed accurate measurements of the gilding thickness.

An evaluation of a portable XRF for the quantitative elemental analysis of siliciclastic soils and sediments was performed.[149] A calibration scheme, which employed RMs as the calibration standards and least-squares regression techniques, produced significant improvement in the data quality over the manufacturer's calibration. On the basis of repeated analyses of the RMs, the instrument response showed a good correlation with the concentrations of the majority of elements. Long-term (~1 year) repeated analyses of the RMs revealed significant changes in the instrument response for several chemical elements, indicating the need for a user-performed dynamic calibration or factory recalibration. It was claimed that the results were in good agreement with independent laboratory analyses when the portable XRF was well calibrated.

When dealing with complex stratigraphies (several superimposed layers with a total thickness up to a few millimeters) by EDXRF, the information related to the inner layers is limited. Bonizzoni et al.[150] reported the potentials and limits of an investigation of complex polychrome stratigraphies using portable EDXRF. XRF cannot determine the thickness with satisfactory precision when it deals with real samples, for which the dilution factor is not known and also the sequence of the layers is based on the hypothesis regarding the historical use of the pigments. The dilution ratio and oil absorption of the different pigments affect the calculation of the layer thickness through XRF measurements. A determination of the layer thickness cannot be performed using EDXRF only because it is unclear which layer the signals originate from. For this reason, a tool to recognize the composition of the external layer (superficial pigments) is needed using other molecular spectroscopic techniques.

An analytical method for the rapid detection of toxic metals, particularly Pb on contaminated oyster shells by a portable XRF was reported.[151] Since the methodology was applied to non-destructive shells, it provided toxic metal contamination on both the inner and outer shells. XRF analysis of the uncrushed samples showed that Pb had accumulated on the surface. This would also eliminate the procedures associated with sample treatment/digestion. Portable EDXRF was found to be suitable for rapid screening, field testing, and the rapid identification of oyster shell metal contamination.

Brake wear from automotive vehicles contains trace metals, which tend to pollute roadside soils, drain water from roads, and ambient air. Quantitative knowledge on the compositions of brake linings is important to legal agencies to comply with environmental policies. In situ measurements of solid brake pad samples using a hand-held EDXRF were performed as a preliminary evaluation of its potential as a screening method.[152] As no RM for brake pads was available, they developed two extraction procedures for the elements present in automotive brake linings, determined their concentrations by ICP-OES, and then compared them with those from the hand-held EDXRF. The comparison indicated hand-held EDXRF analysis to be an efficient and reliable screening tool for the trace metal contents in automotive brake pads with respect to the legal standards.

Conventional XRF bone Pb measurement system employs Pb K X-rays. Although bone Pb data has been found to be a better biomarker for predicting many health effects related to long-term Pb exposure than the blood Pb level, only a few research institutions possess this technology. A more accessible technology to measure the bone Pb level would have important benefits for examining the health effects of lead exposure. An in vivo bone lead quantification methodology by a portable XRF technology was proposed.[153] The correlation of the in vivo bone lead concentrations between standard XRF and their portable XRF method was significant, and the detection limit for the portable XRF method was quite good, approximately 8.4 ppm for a 2 mm soft tissue thickness. The entrance skin dose delivered to a human subject would pose minimal radiation risk, demonstrating that the portable XRF method can be used for in vivo bone Pb measurements with sensitivity comparable to that of a conventional XRF bone Pb measurement system.

X-ray reflectometry (XRR) is a nondestructive technique used to assess the multilayer structure properties, which measures the

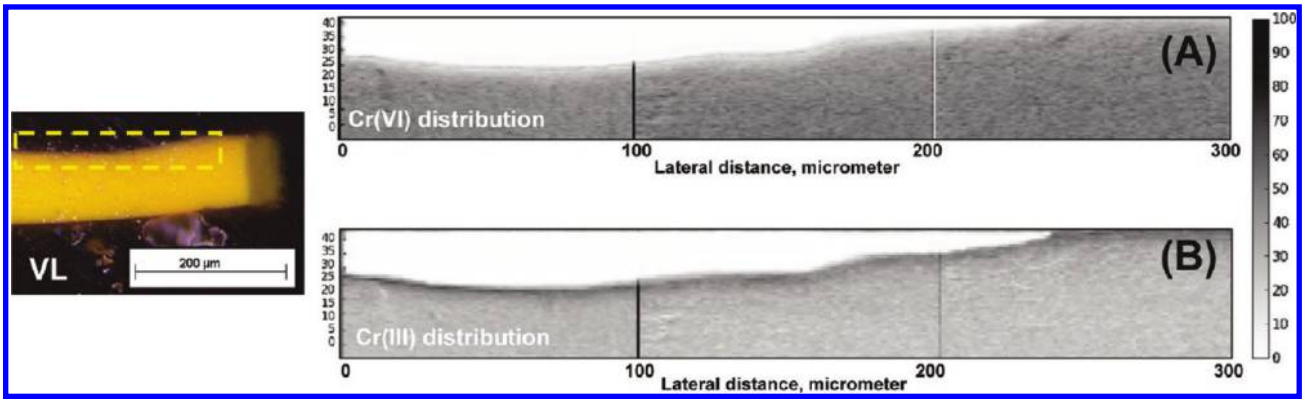

Figure 10. Cr chemical-state maps of aged sample. (Left panel) Visible light microscopy image (VL) of embedded aged model sample and (right panels) species-specific distribution in the indicated area of (A) Cr(VI) and (B) Cr(III) maps obtained by micro-XRF scanning at 5.993 and 6.086 keV. Map size: 42 × 300 μm^2, pixel size: 0.25 × 1 μm^2, dwell time: 0.1 s. Reprinted from ref 156. Copyright 2011 American Chemical Society.

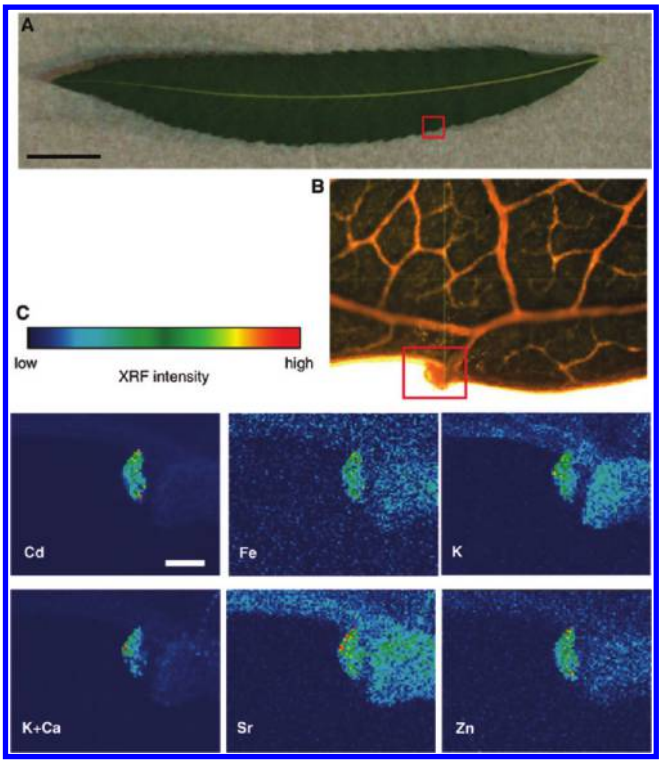

Figure 11. Micro-XRF imaging of a leaf of *S. gilgiana*. (A) Photograph of the whole leaf of *S. gilgiana*. Bar = 1 cm. The imaging area is shown in the red square. (B) The serrations of a *S. gilgiana* leaf. The imaging area is shown in the red square. (C) The two-dimensional distribution of Cd, Fe, K, K + Ca, Sr, and Zn. The XRF signal intensity is shown as a color scale. Beam size: 0.65 μm × 1.1 μm. Step size: 5 μm × 5 μm. Bar = 100 μm. Harada, E.; Hokura, A; Takada, S.; Baba, K.; Terada, Y.; Nakai, I.; Yazaki, K. Characterization of Cadmium Accumulation in Willow as a Woody Metal Accumulator Using Synchrotron Radiation-Based X-ray Microanalyses. *Plant Cell Physiol.* **2010**, *51*, 848−853, by permission of Japanese Society of Plant Physiologists.

film thickness, interfacial roughness, and film density. No portable XRR instrument was available until a new portable XRR apparatus, which measures the thickness of multilayers on the nanoscale range, was developed.[154] The reflectometer apparatus was set up by aligning the X-ray tube, sample holder, and Si-PIN detector in a single plane. The spectrum was measured as a function of the X-ray energy for the continuum X-rays used in the measurement, whereas the spectrum was measured as a function of the glancing angle for monochromatic X-rays. A Mo/Si (9.98 nm) multilayer sample was used to validate this instrument, and its feasibility for multilayer nanothickness measurements was confirmed.

Micro-XRF. As described in the section on Micro-XRF and Imaging, micro-XRF analysis is a powerful tool for obtaining 2D or 3D mapping images of elemental distribution in samples. The micro-XRF technique has become customary using micro- or nano-X-ray beams produced by the recent rapid progress in hard X-ray focusing technology. Numerous investigations of micro-XRF measurements were performed on various sample types such as biological samples, plants, alloys, geological samples, and archeological objects.

In the past few years, an international research group, mostly in Delft University of Technology and Antwerp University, has published many articles relating to the study of art and archeology using micro-X-ray techniques, e.g., micro-XANES, micro-XRD, X-ray micro-CT, and micro-XRF. In particular, one of their famous efforts with art samples was to visualize a woman's head hidden under Vincent Van Gogh's "*Patch of Grass*" painting using SR-micro-XRF and XANES techniques. This work, published in *Analytical Chemistry* in 2008, is considered a hot topic for the application of micro-XRF measurements and was introduced in our previous review in *Analytical Chemistry*. In addition, in 2010, the research group wrote a review article concerning the non-destructive analysis of painted cultural heritage artifacts in *Accounts of Chemical Research* involving their works.[155] Herein, we introduced two of their research articles on the analysis of art samples among the literature published by the research group, which are related to the analysis of the degradation process of chrome yellow in Van Gogh's paintings, *Bank of the Seine* and *View of Arles with Irises*.[156,157] The SR micro-XRF and micro-XANES experiments were performed at the ESRF on beamline ID21. Their measurements were performed under vacuum conditions (10^{-6} mbar) to eliminate absorption of low energy fluorescent radiation. The irradiation submicro X-ray beams are focused on a 0.95 × 0.25 μm^2 spot (horizontal × vertical) using a FZP. The DLs of the micro-XRF system are around 10 ppm for elements with the atomic numbers between 15 (P) and 26 (Fe). The authors obtained Cr chemical-state maps of the aged sample, as shown in Figure 10. Micro-XRF−XAFS spectroscopy coupled

with Raman and FT-IR spectroscopies showed that the darkening is caused by the reduction of $PbCrO_4$ to $Cr_2O_3 \cdot 2H_2O$, possibly accompanied by the presence of another Cr(III) compound. The presence of Cr(III) due to the alteration is sometimes correlated with the presence of Ba and/or aluminosilicates. As the alteration specifically proceeds at the surface layer on the painting, this finding was obtained using the microscopic X-ray spectroscopic methods.

In many cases, the SR micro-XRF technique is often used in combination with other spectroscopic methods, especially SR-XANES or SR-EXAFS analysis. Yamaoka et al.[158] investigated the mechanism of a Cd accumulation in the stem of rice plants (Nipponbare) and (Milyang 23) using SR micro-XRF and SR micro-XANES analysis. A monochromatic X-ray (30 keV) was focused into a micro X-ray beam ($1.1 \times 0.65\ \mu m^2$) with a KB mirror on BL37XU at Spring8. The chemical forms of Cd in the roots, stems, and leaves of the plants were analyzed by SR micro-XANES to reveal the mechanisms of Cd transport in rice. The rice samples were cultivated for 21 and 75 days with a special solution including 3 ppm of Cd. The micro-XRF results showed that the Cd concentration of "Nipponbare" was higher than that of "Milyang 23" at the root, although there was no difference between those in the stem. The micro-XANES analysis indicated that Cd was bound to sulfur in the roots of both rice plants. The amount of Cd combining with S (Cd−S) in the stem of "Nipponbare" became 1.5 times greater after being exposed to Cd, while only a slight change in the stem of "Milyang 23" was found. The authors concluded that differences in the chemical forms of Cd at the stems affected the different accumulation behavior of Cd between "Nipponbare" and "Milyang 23". The same research group also investigated the characterization of Cd accumulation in six willow (*Salix*) species using the same SR micro-XRF and SR micro-XANES setup.[159] Figure 11 shows a 2D micro-XRF image of Cd, Fe, K, Ca, Sr, and Zn in the serrations of a *Salix gilgiana* leaf measured by SR micro-XRF with approximately 1 μm X-ray beams. Obtained micro-XRF images revealed the accumulation of Cd at the tips of the serrations in leaves and the phellogen and/or the phelloderm under the stem surface. In addition, SR micro-XANES spectra of Cd in all the accumulation sites were similar to those of the Cd ion coordinated by O ligands in *Salix gilgiana*.

Pinakidou et al.[160] investigated the distribution and local coordination of Fe and Ni in a Fe−Ni composite with Al matrix by means of micro-XRF and micro-EXAFS. The Al matrix Fe−Ni composite was prepared by dissolving a Fe−Ni rod in liquid Al with a 5% mixture of K_2TiF_6 and KBF_4 at 1060 °C. The micro-XRF, micro-EXAFS experiments were performed at KMC2 beamline at the BESSY-II. The focusing X-ray beam produced by a double-crystal monochromator and capillary optics was 5 μm. Micro-XRF maps of Fe and Ni revealed that the ratio of concentration of Fe/Ni in Fe-rich region was 2.3 times greater than that in Fe-poor region. The micro-EXAFS results in both regions revealed that Fe and Ni were bonded only to Al. In Fe-rich region, Fe and Ni formed $FeAl_3$ and intermetallic NiAl, respectively. In contrast, in Fe-poor region, Fe formed intermetallic FeAl and Ni atoms belonged to an fcc (face-centered cubic) matrix.

SR-XRF performed the desirable micro-XRF analysis with high sensitivity and high spatial resolution. In contrast, recently developed mobile or benchtop micro-XRF spectrometers employing capillary optics and air-cooled X-ray detectors are suitable tools for in situ analysis of major and minor elements. Genna et al.[161] used a benchtop micro-XRF instrument for elemental mapping of volcanogenic massive sulfide deposits related to hydrothermal alteration. The micro-XRF experiment was performed using an EDAX Eagle-III micro-XRF spectrometer equipped with a Rh target and a polycapillary X-ray lens. The excitation setting was 20 kV and 200 μA, and the counting time for each pixel was 800 ms in the mapping area of 1.7×1.3 mm^2 (64×50 pixels). The DLs for major elements calculated by synthetic glasses with known concentrations were 13% for Na_2O, 2.3% for Al_2O_3, and about 0.1% for TiO_2, Cr_2O_3, MnO, and Fe_2O_3.

Confocal micro-XRF is a powerful nondestructive technique for the analysis of 3D elemental distribution in light matrix samples, such as paint, plants, and biological samples. Nakano et al.[162] used a tabletop confocal micro-XRF spectrometer having high spatial resolution to analyze forensic samples such as multilayered automotive paint fragments and leather sheets.[69] Elemental depth profiling at a single point as well as elemental depth imaging in a large area were successfully obtained by the confocal micro-XRF. The structures of some leather sheets showed heterogeneous distribution, and thus, the authors concluded that elemental depth imaging in a large area is more suitable for forensic samples as forensic analysis requires repeatability and reproducibility. Mantouvalou et al.[163] demonstrated depth profiling in elemental analysis of historical glass objects using a compact 3D confocal micro-XRF spectrometer having a depth resolution of 30 to 50 μm. The aim of their study was to discover the manufacturing technique of several medieval reverse paintings on glass. In order to differentiate between cold painting and stained glass, two handmade reference samples were manufactured by two different manufacturing techniques in which glass slides painted with black enamel were fired or not. The depth profiles at single spots on the front and back of the not-fired sample and on the back of the fired sample were similar, while the measurements on the front of the fired sample showed significant change. In addition quantitative measurements with a confocal micro-XRF setup were performed. It was claimed that 3D micro-XRF data must be carefully interpreted because depth resolution and absorption effect are dependent on the energy of fluorescence X-rays. Mihucz et al.[164] studied the removal process of As, Cd, Cu, Mn, Ni, and Ti from washed and cooked rice samples by confocal micro-XRF and laser ablation ICPMS (LA-ICPMS).

A confocal micro-XRF experiment was performed at Beamline L of the DORIS-III of HASYLAB. A quasi-monochromatic X-ray beam at 16.3 keV using a Ni/C monochromator was focused to a spot of 12 μm by a polycapillary with a working distance of 5 mm. The detection side polycapillary half-lens with a working distance of 2 mm was attached to a SDD. The probing volume at 12 keV is about $12 \times 12 \times 12\ \mu m^3$. For confocal micro-XRF analysis, raw and cooked Chinese and Hungarian rice grains were analyzed. Elemental distributions of Mn, As, and Zn in the rice grains revealed that a surface layer having a thickness of about 80 μm is the richest region. In contrast, Ti was detectable only in the so-called skin region. Patterson et al.[165] performed the characterization of Cu-doped Be capsules using confocal micro-XRF. Four Cu-doped sputtered Be capsules were used for the measurement. One capsule was not pyrolyzed with the CH mandrel remaining in the interior, but the other three capsules were pyrolyzed at 425 °C for 40 h. A precision theta stage was mounted in the confocal micro-XRF instrument, in order to perform the line scan through the capsule walls without changing the measurement geometry during the analysis. Perez et al.[166,167] applied a

theoretical approach based on FPM to quantify intermediate thin layer samples with confocal micro-XRF analysis. The proposed procedure assumes that the sample is a homogeneous film. Then, XRF intensities measured in a linear scan of an unknown layered sample were interpreted to obtain information on elemental densities, where a fitting of the fluorescence X-ray intensities was done using the new iterative FPM algorithm to calculate the thickness of the layer and the elemental volumetric densities. An exemplar application of the new procedure for the analysis of a test sample with a paint layer on a glass substrate showed that the accurate quantification by confocal micro-XRF can be performed.

TXRF. TXRF has been used by semiconductor manufacturing companies for the analysis of contaminations on Si wafers. Besides this application, there are reports on the application of TXRF for the trace elemental analysis of environmental and biological samples. In this case, samples in various forms (particles, sliced sheets, solutions, etc.) are placed on a reflector (sample carrier), which is usually an optically flat glass. For this research, commercially available tabletop TXRF instruments such as Picofox (Bruker AXS, Germany), Extra II (Atomika Instruments, Germany), and Nanohunter (Rigaku, Japan) are used as well as laboratory-made instruments.

The bioaccumulation process of Cr(VI) in bacterium was studied by TXRF.[168] Cr(VI) is well-known as an element that is toxic to humans. The time dependence of the Cr concentration in three kinds of bacteria was investigated by TXRF after they were doped in $K_2Cr_2O_7$ solution. It was found that the ANCR (*Acinetobacter beijerinckii* type) bacterium reduced Cr(VI) in the environment during the bioaccumulation process with a yield of ~21%. TXRF will be a useful method for this type of trace analysis.

Marguí et al.[169] studied the procedure for determination of Hg in wastewater samples. The authors paid attention to avoid Hg volatilization during the analysis. The sample preparation was performed by forming a Hg complex with thiourea at pH = 10 and then depositing a 10 μL volume of the sample solution on the TXRF reflector. A detection limit of 7 pg of Hg was achieved with a TXRF 8030C spectrometer (Atomika Instruments GmbH). It was demonstrated that this technique was useful for determining the level of Hg in various wastewaters such as industrial effluents and municipal wastewater. The same research group reported a direct TXRF analysis of Se in environmental and geochemical sample solutions.[170] Yttrium and germanium were added to an environmental water sample and an acid rain extraction solution, respectively, as internal standards. It was demonstrated that the matrix effect of Br affected the detection of Se. Such matrix effect could be reduced by additional sample preparation using a cation exchange column. The direct TXRF analysis was claimed to be fast and relatively simple, and this analytical approach will be important in future applications of TXRF.

TXRF has been applied to the quality control of water samples.[171,172] The water in the Toledo River in Brazil was measured by SR-TXRF (Brazilian Light Synchrotron Laboratory)[171] with a Y-internal standard. Another TXRF analysis was performed for deionized water in the CENA (Center for Nuclear Energy in Agriculture/University of Sao Paulo) water production plant.[172] Quantitative TXRF analysis was performed with a Ge internal standard. TXRF application for water quality control would have the advantages of low-cost operation and multielemental and simultaneous techniques. The preconcentration of As with alumina for the water samples was studied for the TXRF analysis of As.[173] Artificial water samples of As(III) and As(V) were analyzed. As was adsorbed on the alumina, which was placed on a quartz reflector, and then, it was directly measured by TXRF. Quantification of As was performed with an internal standard of Co or Al. A recovery test was performed, resulting in 98% recovery for As(III) and 95% for As(V). A detection limit of 0.7 $\mu g L^{-1}$ for As was reported.

TXRF was applied for the quantitative determination of Ni, Cu, Zn, Br, and Pb in wines produced at two vineyards.[174] A 5 μL volume of wine was dropped on a glass reflector and a Se internal standard was used for quantification, because Se is normally present in wine. It was demonstrated that two types of wine could be distinguished on the basis of elemental compositions as determined by TXRF. TXRF was also used for direct determination of trace elements in petrochemical products.[175] An 8 μL volume of petrochemical solution was deposited on the quartz with a Ga internal standard, and then, it was dried on a hot ceramic plate at 90−100 °C. Fifteen elements were determined in the matrixes such as paraffines, *n*-olefins, etc. The typical contents were below 1 $\mu g\ g^{-1}$. It was confirmed that TXRF analysis had a precision comparable to that of ICP-OES.

The surfaces of plastic (metallic) toys and accessories might contain toxic elements. Thus, TXRF was applied to analyze an acid leaching solution used to treat the toys.[176] A plastic toy (mini car) was put into a HCl solution (0.7 mol L^{-1}) at 37 °C. A 10 μL volume of the HCl solution was dropped on a glass reflector for TXRF analysis with a Ga internal standard. To investigate the leaching process, the time-dependent TXRF intensities of Ca, Cr, Fe, Zn, and Pb were measured in a time range up to 180 min. The increasing rates of TXRF intensity depended on the elements that were present. The result suggests that TXRF analysis will be a powerful tool to monitor the progress of chemical reactions.

A slurry sampling TXRF was applied for a direct determination of trace elements in BN powders.[177] After the slurries were homogenized in an ultrasonic bath for 30 min, three aliquots of 5 μL of slurries were pipetted on a quartz reflector, and then, they were dried on a hot plate at 95 °C. The authors compared the quantitative results of the slurries with other spectroscopic methods such as ETV-ICP-OES and GFAAS. The detection limits obtained by TXRF were basically poorer than those by other methods although TXRF showed better sensitivity for some elements such as Ca, Cu, and Fe. Particle size in slurries strongly affects the sensitivity and quantification by TXRF. A direct TXRF analysis was also performed for glass microspheres which were functionalized with organometallic compounds including Zr.[178] It was found that the particle size of the sample showed strong correlation with the results of direct TXRF concerning quantification, accuracy, uncertainty, and detection limits. The authors believe that ultrasound treatment will optimize the TXRF analytical parameters and open a new sample preparation for TXRF analysis.

Direct TXRF was applied for the analysis of aerosol particles.[179] Atmospheric aerosols were collected on silicon oxide filters for PM_{10} (particulate matter with an aerodynamic diameter less than 10 μm). A small section of the filter was placed on a quartz reflector. Compared with the conventional procedure employing the digestion of aerosol particles by nitric acid, the direct measurement of filters shortened the preparation time from a few hours to a few minutes. Although the background intensity in the direct TXRF spectrum of the filter was higher than that after the digestion procedure, the low detection limits ($<ng/cm^2$) were obtained for many elements. Direct TXRF will be a promising

method for fast measurements and monitoring of trace elements in environmental and biological samples. For this purpose, further study on the quantification of direct TXRF is required. Another direct TXRF analysis of a solid suspension of 20 mg of fine soil granules (<50 μm) was reported by Marguí et al.[180] In this case, the detection limit of Se was 1 mg/kg due to high background intensity at the energy of Se Kα. Thus, a dispersive liquid−liquid microextraction procedure was developed to improve the detection limit, which finally reached 0.05 mg/kg for Se.

TXRF applications for biological samples are increasing. TXRF was applied for the quantification of DNA binding to lipid monolayer at an air−water interface.[181] DNA obtained from salmon was labeled by covalently bound Br. TXRF measurement was performed with a photon energy of 22 keV at a SR facility (ESRF). The grazing incident angle to the liquid surface was 0.04°, which was about 70% of the critical angle for total reflection. The authors found that higher salt concentrations led to an increased amount of adsorbed DNA. This experiment showed a new interesting application of TXRF analysis.

TXRF analysis of biological samples is important for developing feasible medical diagnoses. Magalhaes et al.[182] studied the behavior of trace elements in cancerous and healthy tissues of colon, breast, and stomach. Using a microtome, frozen tissues were cut into thin sections between 5 and 10 μm thick. A thin section was positioned on the quartz glass reflector. Ga, Se, and Y were used as the internal standard. The authors paid careful attention to the sample preparation processes of drying and warming the samples from around −20 °C to room temperature. A statistical data analysis was performed for the quantitative data obtained by TXRF. The result suggests the important roles played by trace elements in cancer. Further experiments will be necessary for reliable medical diagnoses.

Borgese et al.[183] analyzed the trace elements in the hair of a patient who took a traditional Indian medicine. One centimeter of the patient's hair was placed on a quartz reflector, and then, 10 μL of 65% nitric acid solution was added. After being dried in the air, the sample was measured by a commercial TXRF instrument (Picofox). A high concentration of Pb of 17.2 ppm was obtained by the direct TXRF analysis of the hair. This result could be strongly related to the high Pb content in the drug. As the authors mentioned, this result supports that TXRF is useful for a fast, simultaneous analysis with a high probability for a correct and fast diagnosis. The relationship between the elemental composition of oral fluids such as saliva and smoking was studied.[184] Saliva samples were taken from the floor of the mouth, and gingival fluid samples were taken from the upper front teeth. The samples were deposited on an acrylic reflector with the addition of Ga internal solution. The most significant differences between the smoker and nonsmoker were found for S, K, and Ca levels in the saliva samples and for Cl in the gingival crevice fluid.

The trace elements in muscles and fish caught in the Sao Francisco River (Brazil) were measured by SR-based TXRF.[185] The collected samples were treated by acid digestion using HNO_3 and H_2O_2 solution. The TXRF results showed the accumulation of a high concentration of Cr in muscle tissue. Fish and oysters from Sepetiba bay in Brazil were measured by SR-TXRF.[186] The concentrations of most of the metals (e.g., Cr, Zn, Se) were higher in oysters than they were in the fish samples. The results indicate that TXRF analysis of these samples would be useful in environmental monitoring. TXRF was also applied for analyzing forensic ink samples.[187] A commercially available ink product was tagged with rare earths such as La, Pr, Nd, Sm, etc. Manuscripts printed with tagged and untagged inks were tested. A small amount of ink was removed from the printed documents using a clean blade. TXRF could be used for the quantification of the rare earths in the ink, in a manner that is nearly nondestructive.

EPMA. During the review period, a substantial number of applications for the quantitative light element analysis of atmospheric individual particles using SEM/EDX were reported. This technique can identify the chemical species of individual airborne particles without special treatment of the sample. Geng et al.[188] demonstrated its capability of obtaining detailed information on individual particles collected at Ny-Ålesund, Svalbard, Norway, in July, 2007. Thirteen particle types were identified on the basis of their X-ray spectral and SEI data of individual particles, in which particles of marine origin were most abundant, followed by carbonaceous and mineral dust particles. Many aged (reacted) sea salt (and mixture) particles produced by an atmospheric reaction of genuine sea-salts, particularly with NO_x and/or HNO_3, were encountered in almost all aerosol samples. These aged particles greatly outnumbered genuine sea-salt particles, suggesting that the summertime Arctic atmosphere, which was generally regarded as a clean background environment, was disturbed by anthropogenic air pollutants.

By the application of low-Z particle EPMA, the aerosol samples collected at King George Island, Chile, which is located 120 km off the coast of Antarctica, were examined to understand the impact of marine biogenic sulfur species on sea-salt aerosols.[189] Among 2900 individual particles analyzed, four types of particles were identified with sulfur-containing sea-salt particles being the most abundant, followed by genuine sea-salt particles without sulfur species, iron-containing particles, and other species. Internal mixture particles of sea-salt/$CH_3SO_3^-$/SO_4^{2-} were frequently encountered. As nitrate-containing particles were not encountered and the air-masses for all the samples originated from the Pacific Ocean, the oxidation of dimethylsulfide (DMS) emitted from phytoplanktons in the ocean was considered the most likely cause of the formation of mixed sea-salt/$CH_3SO_3^-$/SO_4^{2-} particles.

A total of 3600 individual aerosol particles, collected in Incheon, Korea, on haze and nonhaze days, were analyzed by low-Z particle EPMA.[190] The particles analyzed were classified according to their X-ray spectral data together with their SEIs. The major particle types included organic carbon (OC), elemental carbon (EC), sea-salt, mineral dust, $(NH_4)_2SO_4$/NH_4HSO_4-containing, K-containing, Fe-rich, and fly ash particles. Their relative number abundance showed that, when haze occurred, the number of OC particles had increased significantly, whereas the number of sea-salt and mineral dust particles had decreased significantly (particularly in the $PM_{1.0-2.5}$ fraction). For the other types of particles, except for Fe-rich particles in the $PM_{2.5-10}$ fraction, there were no significant differences in relative abundance between the haze and nonhaze samples. The emission of air pollutants from motor vehicles and stagnant meteorological conditions, such as low wind speed and high relative humidity, might have been responsible for the elevated level of OC particles on haze days.

Aerosol particles collected at an underground shopping area in Seoul, Korea, were characterized.[191] Fourteen particle types were identified on the basis of the SEIs and X-ray spectral data of the individual particles, in which primary soil-derived particles were the most abundant, followed by carbonaceous, Fe-containing, secondary soil-derived, and secondary sea-salt particles. Carbonaceous particles existed in three types: organic carbon, carbon-rich,

and CNO-rich. A significant number of textile particles containing C, N, and O were encountered in some of the aerosol samples, which originated from the textile shops and/or from the clothes of passersby. The primary soil-derived particles showed seasonal variations, with the peak values in spring samples, reflecting the higher air-exchange between the indoor and outdoor environments in spring. Secondary soil-derived, secondary sea-salt, and ammonium sulfate particles were encountered frequently in winter samples. Fe-containing particles, which are believed to have originated from a nearby subway station, were in the range of approximately 19% relative abundance for all samples. Recently, there has been increasing awareness of Fe-containing particles being the major particulate contaminant in the underground subway microenvironment. To clearly identify the indoor sources of subway particles, four sets of samples collected in tunnels, at platforms, near ticket offices, and outdoors at four underground subway stations in Seoul, Korea, were investigated using low-Z particle EPMA.[192] For the samples collected in tunnels, Fe-containing particles predominated with relative abundances of 75−91% at the four stations. The amounts of Fe-containing particles decreased with increasing distance of the sampling locations from the tunnel. Samples collected at the platform in subway stations with platform screen doors (PSDs), which limited air-mixing between the platform and tunnel, showed significant decreases in the relative abundances of Fe-containing particles. These results clearly show that Fe-containing particles originating in tunnels predominated in the indoor microenvironment of subway stations and PSDs play a significant role in reducing Fe-containing particles at platforms and near ticket offices.

Tobacco smoke is one of the greatest sources of indoor particles and has been linked to serious health effects. Consequently, there has been widespread interest in analyzing tobacco-related indoor PM (particulate matter). The majority of studies focused on the bulk chemical composition of tobacco-related PM, and the knowledge of individual tobacco smoke particles is still limited. Slezakova et al.[193] examined the influence of tobacco smoke on the chemical and morphological characteristics of PM_{10} and $PM_{2.5}$ collected at a single site influenced by smoking as well as at a reference (nonsmoking) site. The chemical and morphological characteristics of 4000 individual particles were determined by SEM/EDX, and cluster analysis was used to classify the different particle groups. The results showed that tobacco smoke affected the characteristics of both fine and coarse particles with the influence being stronger for the fine fraction. It was claimed that SEM/EDX was a useful complementary technique for characterizing $PM_{2.5}$ and $PM_{2.5-10}$ and identifying the respective emission sources. Their work would be more desirable if carbonaceous and nitrate particles could be characterized by designing their sampling and experimental setups for the unambiguous detection of carbon and nitrogen.

The PM concentrations measured in Italy can be affected by the advection of Saharan dust. From a period characterized by two episodes of Saharan dust outbreaks in Italy, PM samples were collected at two locations (urban and suburban) in Rome.[194] Some samples were selected and analyzed by SEM/EDX to characterize the PM, focusing on the mineral contribution. Cluster analysis was used to classify approximately 67 000 analyzed particles into one of the seven main statistical groups based on their composition. The characteristics of the particulate components identified by SEM/EDX analysis were validated by PIXE analysis carried out on filters collected in a suburban area. The contribution of crustal particles was consistently high, highlighting the importance of local and regional mineral contributions as well as those of Saharan origin.

The size, morphology, and chemical composition of 8405 particles on moss surfaces (*Hylocomium splendens*) were examined by SEM/EDX.[195] Two moss samples from three locations in Southern Norway and two sampling years (1977 and 2005) each were selected, leading to a total of 12 samples. The major particle groups encountered included silicates, iron-rich silicates, metal oxides/hydroxides, iron oxides/hydroxides, carbonates, carbon-rich particles, silicate fly ashes, iron-rich silicate fly ashes, and iron oxide fly ashes. Between 1977 and 2005, the relative number abundance of the three fly ash groups had decreased substantially. This decrease in the number of fly ash particles with time was overlooked in previous reports on the atmospheric input of pollutants into ecosystems in Southern Norway. In general, the presence of fly ash particles was ignored in most source apportionment studies based on bulk chemical analysis. The high abundance of fly ash demonstrated the need to complement source apportionment based on the bulk chemistry by single particle analysis to avoid misclassifications of this important anthropogenic aerosol component.

Research was performed to gain insight into the heterogeneous reaction of Cr(VI) reduction by zerovalent iron.[196] WD-EPMA was used to clarify the relevant aspects of the reaction with consequences for the conception of interpretative kinetic models. Spherical iron particles with controlled grain sizes were used after being subjected to previous washing with diluted acid to remove the oxidation products. These spheres were immersed in Cr(VI) solutions using different operating procedures. The iron particles were photographed to establish the time evolution of the grain size distribution. A sample of iron balls after the reaction, samples of the raw material, and the precipitates of the reaction products were analyzed by backscattering electron images and elemental mapping produced by WD-EPMA. The spatial distribution of iron, oxygen, and chromium indicated three distinct mechanisms for the reaction with different limiting steps.

SEM/EDX provides a nondestructive microscopic morphological examination of forensic samples. The analytical performance of SEM/EDX equipped with a transition edge sensor (TES) microcalorimeter in forensic analysis was examined.[197] The TES microcalorimeter showed much better energy resolution than the conventional solid-state detectors (SSDs), which overcame some of the identification problems caused by peak overlap when forensic samples were analyzed using a conventional SEM/EDX system based on SSDs. The microcalorimeter EDX spectrum could reveal the coexistence of Ba and S in a paint layer of an automotive white paint fragment containing TiO_2 as the pigment. The coexistence of K, Mg, Al, Si, and Ti in the surface layer suggested the use of titanium dioxide (TiO_2)-coated mica as a pearlescent pigment in paint. Gunshot residue (GSR) particles were also discriminated successfully by detecting Ba, Sb, Pb, and S. Elemental mapping using the TES microcalorimeter system revealed the accumulation of Pb- and Sb-rich particles in GSR. The microcalorimeter SEM/EDX system could offer an analysis with a high-energy resolution and high-spatial resolution at low-excitation voltages, which could be utilized fully as a powerful analytical tool in forensic laboratories.

The role of inorganic particles, particularly asbestos fibers, in the onset of important respiratory diseases and neoplasias is of particular interest. Many experiments have been performed in

vitro to investigate the reaction of the cell organelles when they are in contact with the inorganic phases. On the other hand, the necessary sample preparation destroys the tissue structure, resulting in the loss of all information on intra- and extra-cellular location of the inorganic phases as well as their relationship with the biological system. A study of histological thin sections obtained from the bronchoalveolar lavage (BAL) of a patient affected by an unknown pneumoconiosis was performed using micro-Raman and variable pressure SEM/EDX.[198] Both techniques could be applied directly to routine cytology specimens without the need to digest the organic matter. The sections were analyzed first by optical microscopy to identify the presence of incorporated inorganic particles with particular attention to the fibrous ones. The particles/fibers were then studied both by micro-Raman spectroscopy and variable pressure SEM/EDX. Micro-Raman spectroscopy could identify the mineral phase associated with crystalline inorganic grain preserved by the biological system. SEM/EDX characterization, which defines the elemental chemical composition of the analyzed particle/fiber, confirmed the mineral phase by Raman spectroscopic data or provided identification with certainty when the Raman spectroscopic data was not exhaustive.

U−Th−Pb geochronological dating of monazite using EPMA, a method developed in the past decade, has attracted considerable attention owing to its speed, low cost, and relatively high reliability. In addition, it has a very high spatial resolution that is superior to other in situ techniques for analyzing the compositions of zoned monazite crystals of <50 μm in size. Therefore, this method has been applied widely to determine the timing of multistage tectono-metamorphism. Sanislav[199] examined emplacement of the Mooselookmeguntic pluton, located in the western Maine region of the northern Appalachians, which was believed to have formed toward the end of the Acadian deformation at approximately 370 Ma. The crystallization ages from different parts of the pluton suggested a more sequential emplacement history over a period of ∼20 Myr. The thermal structure of the orogen evolved progressively to enable pluton emplacement and continued to develop afterward with magmatic fluids still forming at depth. The in situ Th−U−Pb dating of monazite with EPMA was used to unravel the Neoproterozoic tectono-thermal history of the "Erinpura Granite" terrane in the foreland of the Delhi Fold Belt in the NW Indian craton.[200] These granitoids were variably deformed and showed the effects of shearing activity. Monazites from the Erinpura granitoids recorded two main events: (i) protolith crystallization at 863 ± 23 Ma and (ii) recrystallization and formation of new Th-poor monazite at 775 ± 26 Ma during a shear overprint. Some components of the Erinpura granitoids, such as Siyawa Granite and exposed granites near Sirohi town, provided evidence for migmatization. This migmatization event was documented by anatexis and the associated monazite crystallization at 779 ± 16 Ma. The age data indicated some overlap in timing between the anatectic event and ductile shear deformation.

PIXE. PIXE has been applied to various samples including biological, medical, industrial, historical, and environmental samples, which have also been analyzed by micro-XRF and EPMA (SEM/EDS). In the case of PIXE analysis, a small-diameter proton beam of a few micrometers and high sensitivity would be an advantage over micro-XRF in the laboratory. An in-air micro-PIXE system, which is useful for many kinds of samples, has become an easily available method.

One of the important applications of PIXE is the analysis of atmospheric aerosols. Lucarelli et al.[201] discussed the PIXE technique compared with other competitive techniques such as ICP-AES, ICPMS, and micro-XRF. PIXE is a nondestructive technique without requiring sample preparation. The advantage of PIXE over XRF is that it can be performed at the same time with other ion beam analyses such as RBS and PIGE and, as a result, the light elements (H, C, N, and O) can be measured. The authors measured marine aerosols and Saharan-dust by external PIXE using the 3-MV Tandetron accelerator. Positive matrix factorization was applied to the PIXE data. Finally, source apportionment identified into several source types such as sea-salt, secondary sulfate, traffic, biomass burning, etc. Similarly, PIXE was used to provide source characterization of Shanghai urban atmospheric aerosols.[202] PM_{10} was collected at the center of Shanghai using polytetrafluoroethylene filters. Principal component analysis applied to the PIXE data indicated that the particles were divided into two categories: those with soil elements (Ca, Fe, K, and Ti) and industrial pollution elements (S, Zn, Pb, Cl, and Se).

Micro-PIXE was applied to the quantitative analysis of cisplatin in esophageal squamous cancer cell lines.[203] Cell morphology was determined by the distribution of P and K, while nuclei were determined by Br. The distribution of cisplatin was visualized by the presence of Pt. The authors concluded that micro-PIXE could be a useful quantitative method for evaluating the cisplatin sensitivity of individual cells. The same in-air micro-PIXE system in the TIARA facility of the Japan Atomic Energy Agency was applied for a study on the relationship between asbestos and disease.[204] Asbestos lung tissue was measured by micro-PIXE. Harmful levels of silica, ferrous iron, and magnesium deposition were estimated. PIXE was also applied to the analysis of minor and trace elements in gallstones of Nigerian patients.[205] It was suggested that the concentrations of P, S, K, and Pb in gallstones depend on the mechanism of the formation of different gallstones.

Preoteasa et al.[206] performed micro-PIXE mapping for Ca, Zr, Ba, and Yb of dental composites using 3.1 MeV protons focused to a 3.0 μm spot and at 3.9 μm pixel size. The PIXE mapping showed evidence of heterogeneous lateral distributions of mineral particles with diameters of 3.2−32 μm for Ca, 20−60 μm for Zr, <4 μm for Ba, and 10−50 μm for Yb. Rautray et al.[207] also measured human teeth by external PIXE. They found that the respective concentrations of elements such as P, Ca, Fe, Zn, and Pb in enamel were greater than those in cementum. In addition, it was suggested that trace elements from food are deposited on the enamel.

Micro-PIXE was used for screening the elemental composition of buckwheat grains.[208] Some elements such as Mg, P, S, K, Fe, Ni, Cu, and Zn were found in the cotyledons and embryo, while K and Fe were also found at high concentrations in the pericarp. PIXE was also applied for elemental characterization of wines produced in different regions of Brazil.[209] The samples (wine) were dried to a solid residue at a temperature of 77° below the boiling point of wine. Compared with European wines, the investigated Brazilian wines contained Cu and Zn with relatively low concentrations and Rb with a high concentration. The PIXE result suggested that the elemental composition of wine is related to the winemaking process as well as to the soil in which the grapes are grown.

A review article on metal hyperaccumulation from soil to plants and insects was published.[210] The cross sections of freeze-dried leaves were measured by micro-PIXE as well as SEM/EDS, indicating high concentrations of Ni in leaf veins and the mesophyll. The most hyperaccumulated metals seemed to be

stored in physiologically inactive tissues. It was also reported that several insects fed exclusively on Ni-hyperaccumulating plants. The study on the hyperaccumulation of metals in plants has been also reported using micro-XRF technique. A discussion on a comparison of both techniques will be required. Ants were measured as bioindicators for assessing metal contamination.[211] Samples of a monomorphic ant species (*Crematogaster. scutellaris*) were collected at different places such as an urban site, an ophiolitic site, and a site far from sources of pollution. Sections of the frozen samples were prepared by an ultramicrotome and then measured by micro-PIXE. Metal concentrations in the gut tissue and body fat were obtained for the samples collected from the different sites. In the ants from the urban site, high concentrations of Zn and Fe were found in the gut tissue and body fat, respectively. Micro-PIXE was also applied in a study of the larval otolith of the Japanese eel (*Anguilla japonica*).[212] Elemental maps of Ca and Sr were obtained with 1 μm resolution. From the analysis of the Sr/Ca intensity ratios, two groups of eels were differentiated, probably because of their different growth environment.

As a typical example of PIXE application in the research field of geochemistry, the laminated carbonate deposited on the side walls of Roman aqueducts was measured by PIXE.[213] It was found that the thick and clear laminae of the carbonate layers were enriched with Sr, while Fe and Si were depleted in the thin and dark laminae. The authors considered that the layered structure was caused by seasonal variations of rainy and dry seasons. In addition, the distribution of Sr suggested that the water in the aqueducts originated from two springs.

Dupuis et al.[214] reported the preliminary results of a high-energy alpha PIXE for archeological research with the advantage of being nondestructive and having a weak Bremsstrahlung background. The experiment was performed in air on the direct beamline of the cyclotron in the Liege Center with high-energy alpha particles from 6 to 12 MeV. Despite a small penetration of the alpha beam, the authors concluded that a high-energy alpha PIXE would be useful for the analysis of objects of cultural heritage with the help of the increased yield of characteristic X-rays as the energy of the alpha beam increased. Roumie et al.[215] showed the possibility of the use of PIXE and RBS for quality control in minting coins. PIXE was useful for investigating the components of the coins, while RBS was helpful in revealing depth profiles. It was confirmed that the Fe substrate was coated with Cu and Ni for 100 and 500 Lebanese lira (LL), respectively.

The characterization of glass fragments is important in forensic science. Several types of glass fragments were measured by PIXE.[216] Trace elements of Ti, Cr, Mn, Cu, Zn, Sr, and Zr as well as Ca and Fe elements were quantitatively analyzed, which were useful for differentiating the samples. The sensitivity of LA-ICPMS is higher than that of PIXE, whereas the nondestructive fast technique is a big advantage of PIXE. The trace elements in single textile fibers (0.1−1 mm thick) as forensic samples were also analyzed by PIXE.[217] The nondestructive PIXE analysis was performed, and yet the radiation damage changed the mechanical and optical properties of the sample. The authors attempted two unique normalization procedures which utilized X-ray intensities of Ar in air and Ti emitted from a Ti wire chopper of 0.25 mm thick with a frequency of 2 Hz. The characteristic X-ray signals could be normalized using either the Ar or Ti X-rays, and yet actual normalization was performed using Ar X-ray intensity. Quantification was performed for trace elements such as Ti, Ca, Fe, Cr, Ma, Co, and Zn. The authors mentioned that results of comparable quality might be also obtained by micro-XRF in a helium atmosphere (or in a vacuum).

XAS. The applications of XAS cover the fields of physics, chemistry, material sciences, biology, earth and environmental sciences, archeology, cultural-heritage science, and more. In all of these areas, chemical and structural information should be elucidated as much as possible from each XAS spectrum. While the theoretical understanding of EXAFS has been so well achieved that one can often analyze and interpret data without the need for experimental models, the same cannot be said for XANES. However, the theory for XANES is good enough to provide useful guides. For instance, pre-edge features contain valuable information. Cabaret et al.[218] reported first-principle calculations of the pre-edge peaks in K-edge XANES of 3d transition metals. Five edges for the electronic states of Ti^{4+}, Fe^{2+} LS (low-spin), Cr^{3+}, V^{3+}, and Fe^{3+} LS were selected for the simulation of their pre-edges in the K-edge XANES by first-principle calculations based on density functional theory (DFT) with the local density approximation (LDA). In most cases, the DFT−LDA methods can reproduce experimental pre-edge structures, from which more information on the electronic states and symmetry around the element can be extracted from the pre-edge analysis.

X-ray magnetic circular dichroism (XMCD) reflects the magnetic properties of the target atom, such as its spin and orbital magnetic moment. The spectrum can be obtained as the difference of two XAS spectra measured using left- and right-circularly polarized incident X-rays in a magnetic field. Van der Laan et al.[219] measured XMCD for ferromagnetic spinel $MnCr_2O_4$ films and found (i) a marked angular dependence of XMCD for Mn^{2+} and Cr^{3+} at their $L_{III,II}$-edges and (ii) the presence of XMCD signals with distinct spectral features even in the transverse geometry. The results can be simulated by atomic multiplet calculations, taking into account the reduced symmetry of the crystal lattice induced by the strain. The change in electronic properties with structural parameters suggested in the present study is of great interest in the fabrication of a functional nanoelectronic system.

Warm dense matter (WDM) is the nonequilibrium state observed during the phase transition from solid to plasma. Describing the properties of WDM is important in various studies, such as those on the cores of some large planets and thermonuclear fusion compressions. Mančić et al.[220] applied a laser-accelerated proton beam to heat Al metal samples to achieve isochoric heating in a short time in the order of 10 ps. The change in the local structure around Al after the heating was examined by an ultrafast broadband X-ray probe beam to measure the time-resolved XANES spectra. The detection system is similar to that of differential XAS measured around the Al K-edge using an imaging plate as a detector, which can simultaneously measure incident and transmission spectra for the normalization. Within the about 10 ps time window, the loss of short-range ordering in Al was detected by time-resolved XANES spectroscopy.

Actinide chemistry is a frontier field in chemistry because of difficulties in handling and the short half-lives of some nuclides. In particular, actinide chemistry is important, especially in the chemistry of nuclear fuels and radioactive wastes. Nishi et al.[221] employed XAFS to study americium, one of the actinides, to characterize the sesquioxide (Am_2O_3) and dioxide (AmO_2) with A-type rare earth oxide and fluorite structures, respectively. Structural data obtained by EXAFS were consistent with the

crystallographic data. Americium L_{III}-edge XANES (18.2 keV) was simulated by the all-electron full potential linearized augmented plane wave (FP−LAPW) method. The results revealed that the white line peak and the second broad peak can be explained by the interaction of the Am-d component with the O-p and O-d components, respectively. In particular, the reactivity of Am(IV), a strong oxidizing agent, is important in understanding the reactions that can be caused by Am(IV) in advanced fuels.

In the European Synchrotron Radiation Facility (ESRF), there is a beamline, named as the Rossendorf Beamline, specially dedicated to actinide chemistry. Most of the studies are on uranium, but some XAS studies have been done for other actinides such as protoactinium, curium, and californium (Cf). Galbis et al.[222] studied on hydration of Cf^{3+} by EXAFS coupled with Monte Carlo simulation. They measured Cf L_{III}-edge EXAFS for 1 mM aqueous solution of Cf^{3+}. The distance of Cf−O is of interest, related to actinide contraction as was analogously known for lanthanide. It is expected that the contraction can be readily seen in the heavier actinide elements from americium to curium, berkelium, and Cf, since they are dissolved as trivalent as the most stable oxidation state in water. The comparison of the experimental EXAFS spectra with two computed structures obtained from two different intermolecular potentials, BP86 and MP2, led to the conclusion that the actinide contraction is supported by the structural information of the heaviest actinide aqua ion studied so far.

Hybrids of 3D porous media with metallic clusters in the pore have been studied for the formation of thermally and chemically stable materials for gas storage, gas separation, and catalytic purposes. Among various possible systems, metallic nodes linked by long organic spacers were investigated by Masciocchi et al.,[223] where they synthesized cubic octanuclear Ni(II) clusters in porous polypyrazolyl-based materials. The determination of the structure of the Ni cluster is a subject to which XAS can contribute. The XANES and EXAFS spectra at the Ni K-edge showed the symmetry information and interatomic distances for Ni−O, Ni−N, and Ni−Ni shells to reveal the network of the Ni cluster. In this type of work, interpreting the data with other information, such as elemental analyses, UV/vis and IR spectra, and XRD data is critical.

XAS in the soft X-ray region has been widely used in polymer sciences. In particular, scanning transmission X-ray microscopy (STXM) is useful to obtain topographic and chemical information for polymers. Watts and McNeill[224] conducted an STXM analysis on thin-film polymer blends of semiconducting polymers, which have various applications in organic solar cells, light-emitting diodes, and nonvolatile memories. They employed two detection systems, conventional transmission and total electron yield modes, in their STXM system. The latter detects photoelectrons from the near surface of the materials, which provides the composition of the first few nanometers of the film. By combining the two modes, the mixing state of two polymers was clearly understood, i.e., the penetration of one phase into the other and the formation of droplets of one phase in the other. The characterization, including the chemical information obtained by STXM, can improve our understanding of the relationship between the structure and function of organic thin films.

The interaction of metal ions and macromolecules is important in biological activities, as one-third of all proteins bind to metal ions. The combination of electrophoresis with XRF and XAS analyses has become an important analytical method to understand the role of metal ions in proteins. Finney et al.[225] provided two examples: the in vitro system of Cr in serum and the in vivo experiment for Fe in the cell lysate system. These methods generally employ the separation of metalloproteins by polyacrylamide gel electrophoresis, followed by rapid XRF scanning of the gel on a plastic substrate. Subsequent XAS analysis on the spot found in the XRF image can provide chemical information of the metal ions in the proteins. The study showed (i) the oxidation state of Cr exposed to the serum proteins related to the biochemistry of Cr dietary supplement and (ii) the influence of oxygen depletion on Fe species in *Shewanella oneidensis*.

The concentrations of trace elements in seawater are controlled by adsorption reactions on oxide surfaces, such as iron and manganese oxides present in water columns in seawater. Kashiwabara et al.[226] showed that the isotopic ratio of Mo in seawater is also controlled by adsorption reactions on such oxides in seawater. Selective incorporation of the light isotope of Mo into ferromanganese oxides was suggested, which became a basis for the use of the Mo isotopic ratio to clarify the paleoredox record on the history of the earth. Molybdenum K-edge EXAFS and L_{III}-edge XANES showed that Mo adsorbed on manganese oxide is in an octahedral symmetry site in contrast to the tetrahedral molybdate ion, the main species of Mo dissolved in seawater. The symmetry change from tetrahedral to octahedral during the adsorption on manganese oxide is responsible for the large isotopic fractionation found for Mo in the ocean. The results were consistent with that of the Mo species in natural ferromanganese oxides examined by XAS analyses. The speciation of various heavy elements by XAS will contribute to the understanding of isotopic fractionation of heavy elements in the future.

Manganese oxide is formed by oxidation of Mn(II) to Mn(III) and Mn(IV), mainly by bacterial activities at the earth's surface. Subsequently, manganese oxide can oxidize organic materials and also water with the aid of light. Hocking et al.[227] reported water-oxidation catalysis by manganese in a Nafion matrix. Although the initial Mn species impregnated in the matrix is a tetranuclear-manganese cluster, it was shown that the water-oxidation reaction is catalyzed by nanoparticles of Mn(III/IV) oxides secondarily formed on the Nafion. In addition, the activity is recovered by the oxidation of Mn(II) in the Nafion film on an electrode. In this study, the cycles of oxidation into solid Mn(III/IV) oxides followed by photoreduction to Mn(II) were characterized by XANES and EXAFS analyses. They emphasized that the Mn oxides are ubiquitous minerals found on the earth's surface and that the redox cycle of Mn on the electrode resembles the biogeochemical cycling of manganese in nature.

The speciation of toxic elements in the environment is of great importance in environmental sciences. Nakazawa et al.[228] identified mercury species in various tissues of a striped dolphin by micro-XRF-XRD. Moreover, Hg species were determined by XAS for an insoluble fraction after enzyme digestion of the nuclear and mitochondrial fractions of all the tissues examined (liver, kidney, lung, spleen, pancreas, muscle, and brain). The analysis identified tiemannite (HgSe) in the liver and other tissues. Marine mammals detoxify mercury by forming mercury selenide, mainly in the liver. The results in the study suggested that the detoxification process can proceed in various tissues aside from the liver.

The report of the Intergovernmental Panel on Climate Change indicated that aerosols contribute to global cooling by direct and indirect effects. The latter effect is caused by

cloud-forming effect of hygroscopic aerosols, such as sulfate and organic acid aerosols in the atmosphere. Their high hygroscopicity can induce cloud formation, which in turn reflects sunlight and causes global cooling. Oxalic acid, the main component of organic aerosols in the atmosphere, greatly contributes to the indirect cooling effect. Furukawa and Takahashi[229] employed XAS to determine Ca and Zn species in aerosols collected by size-fractionation air samplers in Japan. As a result, considerable amounts of Ca and Zn were found to be present as metal−oxalate complexes in the aerosols. Taking into account the total amount of oxalate and the possible contributions of other metal ions to the metal−oxalate complex formation, most oxalates turn out to form insoluble metal complexes in the aerosols. This result suggests that the hygroscopic property of oxalic acid may be much smaller than expected. The formation of metal−oxalate complexes is important for the evaluation of the hygroscopic property of oxalic acid in aerosols that can be related to the global cooling effect.

AUTHOR INFORMATION

Corresponding Author

*E-mail: tsuji@a-chem.eng.osaka-cu.ac.jp.

BIOGRAPHIES

Kouichi Tsuji graduated in 1992 at Tohoku University, Japan, and received his Ph.D. in metallurgy. After that, he became research associate in the Analytical Science Division of the Institute for Materials Research (IMR), Tohoku University, Japan. Since 2002, he has studied at Osaka City University, Japan. At present, he is a Full Professor in the Department of Applied Chemistry & Bioengineering. His research activities involve the development and improvement of analytical X-ray methods, such as TXRF, Micro(3D)-XRF, ED-XRF, PIXE, EPMA, and their applications.

Kazuhiko Nakano graduated in the field of industrial chemistry from Meiji University in Tokyo, Japan, in 2000. He received his Ph.D. from Meiji University in 2005. At present, he is a Visiting Researcher at the Department of Applied Chemistry & Bioengineering at Osaka City University, Osaka. His research interests include the development of a novel 3D microregion XRF spectrometer, quantitative analysis of trace elements in environmental samples, and development of environmental reference materials.

Yoshio Takahashi graduated in 1997 from The University of Tokyo, Japan, and received his Ph.D. in environmental radiochemistry. After that, he became a research associate in Department of Earth and Planetary Systems Science, Hiroshima University, Japan. At present, he is a Full Professor in the same department in Hiroshima University. His research interest is primarily in the speciation studies in environmental chemistry and geochemistry to understand fates of contaminants, geochemical cycles, and evolution of the earth.

Kouichi Hayashi graduated in 1996 at Kyoto University, Japan, and received his Ph.D. in electronics science. After that, he became Assistant Professor at Kyoto University. Since 2003, he has been Associate Professor at the Institute for Materials Research, Tohoku University, Japan. His research activities involve methodological developments such as X-ray holography and total reflection X-ray fluorescence and related techniques and their applications to advanced materials.

Chul-Un Ro received his M.Sc. in chemistry from the Korean Advanced Institute of Science and Technology in Seoul, Korea, in 1981. He carried out his Ph.D. work at the University of North Carolina at Chapel Hill, USA, dealing with surface analysis using XPS and SIMS. At present, he is a Full Professor in the Department of Chemistry at Inha University in Korea. His research interest is primarily in the application of quantitative single particle analysis, known as low-*Z* particle EPMA, for the characterization of diverse atmospheric aerosol particles, and he is involved in the development of various single particle analytical techniques based on FT-IR imaging, micro-Raman, and optical microscopy.

ACKNOWLEDGMENT

The authors would like to thank Mrs. Yukiko Kokudo of Osaka City University for her continuous support for the preparation for this review article. We wish to thank Dr. Matthew A. Marcus (Advanced Light Source) and Dr. Hajime Tanida (Kyoto University) for their helpful comments in the XAS-related chapters.

REFERENCES

(1) West, M.; Ellis, A. T.; Potts, P. J.; Streli, C.; Vanhoof, C.; Wegrzynek, D.; Wobrauschek, P. *J. Anal. At. Spectrom.* **2010**, *25*, 1503–1545.

(2) West, M.; Ellis, A. T.; Potts, P. J.; Streli, C.; Vanhoof, C.; Wegrzynek, D.; Wobrauschek, P. *J. Anal. At. Spectrom.* **2011**, *26*, 1919–1963.

(3) Als-Nielsen, J.; McMorrow, D. *Elements of Modern X-ray Physics*, 2nd ed.; Wiley: Chichester, UK, 2011.

(4) Denecke, M. A.; Walker, C. T. *AIP Conference Proceedings: X-ray Optics and Microanalysis: Proceedings of the 20th International Congress Conference*; Springer: New York, 2010.

(5) Lee, J.; Nam, C. H.; Janulewicz, K. A. *X-ray Lasers 2010: Proceedings of the 12th International Conference on X-ray Lasers*; Springer: New York, 2011.

(6) *X-ray Spectrom.: Spec. Issue: European Conference on X-ray Spectrometry*, 20−25 June 2010, Figueira da Foz, Coimbra, Portugal; 2011, Vol. 40 (1,2,4).

(7) *X-ray Spectrom.: Spec. Issue: PIXE 2010*; 2011, Vol. 40 (3).

(8) Janssens, K.; de Nolf, W.; van der Snickt, G.; Vincze, L.; Vekemans, B.; Terzano, R.; Brenker, F. E. *TrAC, Trends Anal. Chem.* **2010**, *29*, 464–478.

(9) Sakdinawat, A.; Attwood, D. *Nat. Photonics* **2010**, *4*, 840–848.

(10) Ukibe, M.; Shiki, S.; Kitajima, Y.; Ohkubo, M. *X-ray Spectrom.* **2011**, *40*, 297–300.

(11) Jach, T. *Surf. Int. Anal.* **2010**, *42*, 1646–1649.

(12) Beiersdorfer, P.; Brown, G. V.; Clementson, J.; Dunn, J.; Morris, K.; Wang, E.; Kelley, R. L.; Kilbourne, C. A.; Porter, F. S.; Bitter, M.; Feder, R.; Hill, K. W.; Johnson, D.; Barnsley, R. *Rev. Sci. Instrum.* **2010**, *81*, 10E323.

(13) Meidinger, N.; Andritschke, R.; Ebermayer, S.; Elbs, J.; Hälker, O.; Hartmann, R.; Herrmann, S.; Kimmel, N.; Schächner, G.; Schopper, F.; Soltau, H.; Strüder, L.; Weidenspointner, G. *Nucl. Instrum. Methods Phys. Res., Sect. A* **2010**, *624*, 321–329.

(14) Tomás, A.; Aune, S.; Dafni, T.; Fanourakis, G.; Ferrer-Ribas, E.; Galán, J.; Gardikiotis, A.; García, J. A.; Geralis, T.; Giomataris, I.; Gómez, H.; Iguaz, F. J.; Irastorza, I. G.; Luzón, G.; Morales, J.; Papaevangelou, T.; Rodríguez, A.; Ruz, J.; Seguí, L.; Vafeiadis, T.; Yildz, S. C. *X-ray Spectrom.* **2011**, *40*, 240–246.

(15) Strüder, L.; Epp, S.; Rolles, D.; Hartmann, R.; Holl, P.; Lutz, G.; Soltau, H.; Eckart, R.; Reich, C.; Heinzinger, K.; Thamm, C.; Rudenko, A.; Krasniqi, F.; Kühnel, K.-U.; Bauer, C.; Schröter, C.-D.; Moshammer, R.; Techert, S.; Miessner, D.; Porro, M.; Hälker, O.; Meidinger, N.;

Kimmel, N.; Andritschke, R.; Schopper, F.; Weidenspointner, G.; Ziegler, A.; Pietschner, D.; Herrmann, S.; Pietsch, U.; Walenta, A.; Leitenberger, W.; Bostedt, C.; Möller, T.; Rupp, D.; Adolph, M.; Graafsma, H.; Hirsemann, H.; Gärtner, K.; Richter, R.; Foucar, L.; Shoeman, R. L.; Schlichting, I.; Ullrich, J. *Nucl. Instrum. Methods Phys. Res., Sect. A* **2010**, *614*, 483–496.

(16) Philipp, H. T.; Koerner, L. J.; Hromalik, M. S.; Tate, M. W.; Gruner, S. M. *IEEE Trans. Nucl. Sci.* **2010**, *57*, 3795–3799.

(17) Ponchut, C.; Rigal, J. M.; Clément, J.; Papillon, E.; Homs, A.; Petitdemange, S. *J. Instrum.* **2011**, *6*, C01069.

(18) Scharf, O.; Ihle, S.; Ordavo, I.; Arkadiev, V.; Bjeoumikhov, A.; Bjeoumikhova, S.; Buzanich, G.; Gubzhokov, R.; Günther, A.; Hartmann, R.; Kühbacher, M.; Lang, M.; Langhoff, N.; Liebel, A.; Radtke, M.; Reinholz, U.; Riesemeier, H.; Soltau, H.; Strüder, L.; Thünemann, A. F.; Wedell, R. *Anal. Chem.* **2011**, *83*, 2532–2538.

(19) Shinohara, Y.; Imai, R.; Kishimoto, H.; Yagi, N.; Amemiya, Y. *J. Synchrotron Radiat.* **2010**, *17*, 737–742.

(20) Matsuo, T.; Yagi, N. *J. Synchrotron Radiat.* **2011**, *18*, 601–604.

(21) Freed, M.; Park, S.; Badano, A. *Med. Phys.* **2010**, *37*, 2593–2605.

(22) Weber, G.; Bräuning, H.; Hess, S.; Märtin, R.; Spillmann, U.; Stöhlker, Th. *J. Instrum.* **2010**, *5*, C07010.

(23) Ryan, C. G.; Kirkham, R.; Hough, R. M.; Moorhead, G.; Siddons, D. P.; de Jonge, M. D.; Paterson, D. J.; De Geronimo, G.; Howard, D. L.; Cleverley, J. S. *Nucl. Instrum. Methods Phys. Res., Sect. A* **2010**, *619*, 37–43.

(24) Kishimoto, S.; Taniguchi, T.; Tanaka, M.; Mitsui, T.; Seto, M. *Nucl. Instrum. Methods Phys. Res., Sect. A* **2010**, *623*, 608–609.

(25) Prokesch, M.; Bale, D. S.; Szeles, C. *IEEE Trans. Nucl. Sci.* **2010**, *57*, 2397–2399.

(26) Sato, E.; Abderyim, P.; Enomoto, T.; Watanabe, M.; Hitomi, K.; Takahasi, K.; Sato, S.; Ogawae, A.; Onagawa, J. *Nucl. Instrum. Methods Phys. Res., Sect. A* **2010**, *619*, 262–265.

(27) Herrmann, C.; Engel, K.-J.; Wiegert, J. *Phys. Med. Biol.* **2010**, *55*, 7697–7713.

(28) Destefano, N.; Mulato, M. *Nucl. Instrum. Methods Phys. Res., Sect. A* **2010**, *624*, 114–117.

(29) Yong, G. J.; Kolagani, R. M.; Adhikari, S.; Drury, O. B.; Gardner, C.; Bionta, R. M.; Friedrich, S. *Rev. Sci. Instrum.* **2010**, *81*, 113906.

(30) Chen, F.; Wang, K.; Fang, Y.; Allec, N.; Belev, G.; Kasap, S.; Karim, K. S. *IEEE Sens. J.* **2011**, *11*, 505–509.

(31) Li, Z.; Jiang, X.; Liu, S.; Huang, T.; Zheng, J.; Yang, J.; Li, S.; Guo, L.; Zhao, X.; Du, H.; Song, T.; Yi, R.; Liu, Y.; Jiang, S.; Ding, Y. *Rev. Sci. Instrum.* **2010**, *81*, 073504.

(32) Kingsley, J. W.; Weston, S. J.; Lidzey, D. G. *IEEE J. Sel. Top. Quantum Electron.* **2010**, *16*, 1770–1775.

(33) Pantazis, T.; Panatazis, J.; Huber, A.; Redus, R. *X-ray Spectrom.* **2010**, *39*, 90–97.

(34) Shvyd'ko, Y. V.; Stoupin, S.; Cunsolo, A.; Said, A. H.; Huang, X. *Nat. Phys.* **2010**, *6*, 196–199.

(35) Durbin, S. M.; Colella, R. *Nat. Phys.* **2010**, *3*, 163–164.

(36) Mimura, H.; Handa, S.; Kimura, T.; Yumoto, H.; Yamakawa, D.; Yokoyama, H; Matsuyama, S.; Inagaki, K.; Yamamura, K.; Sano, Y.; Tamasaku, K.; Nishino, Y.; Yabashi, M.; Ishikawa, T.; Yamauchi, K. *Nat. Phys.* **2010**, *6*, 122–125.

(37) Mimura, H.; Kimura, T.; Yumoto, H.; Yokoyama, H.; Nakamori, H.; Matsuyama, S.; Tamasaku, K.; Nishino, Y.; Yabashi, M.; Ishikawa, T.; Yamauchi, K. *Nucl. Instrum. Methods Phys. Res., Sect. A* **2011**, *635*, S16–S18.

(38) Morawe, C.; Osterhoff, M. *Nucl. Instrum. Methods Phys. Res., Sect. A* **2010**, *616*, 98–104.

(39) Terada, Y.; Yumoto, H.; Takeuchi, A.; Suzuki, Y.; Yamauchi, K.; Uruga, T. *Nucl. Instrum. Methods Phys. Res., Sect. A* **2010**, *616*, 270–272.

(40) Takano, H.; Tsuji, T.; Hashimoto, T.; Koyama, T.; Tsusaka, Y.; Kagoshima, Y. *Appl. Phys. Express* **2010**, *3*, 076702.

(41) Kagoshima, Y.; Takano, H.; Koyama, T.; Tsusaka, Y.; Saikubo, A. *Jpn. J. Appl. Phys.* **2011**, *50*, 022503.

(42) Vila-Comamala, J.; Gorelick, S.; Färm, E.; Kewish, C. M.; Diaz, A.; Barrett, R.; Guzenko, V. A.; Ritala, M.; David, C. *Opt. Express* **2011**, *19*, 175–184.

(43) Ezoe, Y.; Mitsuishi, I.; Takagi, U.; Ishizu, K.; Moriyama, T.; Mitsuda, K. *IEEE J. Quantum Electron.* **2010**, *46*, 1295–1300.

(44) Nazmov, V.; Reznikova, E.; Mohr, J.; Saile, V.; Vincze, L.; Vekemans, B.; Bohic, S.; Somogyi, A. *J. Micromech. Microeng.* **2011**, *21*, 015020.

(45) MacDonald, C. A. *X-ray Opt. Instrum.* **2010**, *2010*, 867049.

(46) Zhou, W.; Mahato, D. N.; MacDonald, C. A. *Thin Solid Films* **2010**, *518*, 5047–5056.

(47) Castoldi, A.; Ozkan, C.; Guazzoni, C.; Bjeoumikhov, A.; Hartmann, R. *IEEE Trans. Nucl. Sci.* **2010**, *57*, 2564–2570.

(48) Nakazawa, T.; Nakano, K.; Yoshida, M.; Tsuji, K. *Powder Diffr.* **2011**, *26*, 163–167.

(49) Yamamoto, T.; Nanbu, F.; Tanaka, T.; Kawai, J. *Anal. Chem.* **2011**, *83*, 1681–1687.

(50) Wolff, T.; Malzer, W.; Mantouvalou, I.; Hahn, O.; Kanngießer, B. *Spectrochim. Acta B* **2011**, *66*, 170–178.

(51) Czyzycki, M.; Wegrzynek, D.; Wrobel, P.; Lankosz, M. *X-ray Spectrom.* **2011**, *40*, 88–95.

(52) Elam, W. T.; Scruggs, B.; Nicolosi, J. *Powder Diffr.* **2010**, *25*, 182–186.

(53) Gazulla, M. F.; Rodrigo, M.; Vicente, S.; Orduña, M. *X-ray Spectrom.* **2010**, *39*, 321–327.

(54) Gazulla, M. F.; Vicente, S.; Orduña, M. *X-ray Spectrom.* **2011**, *40*, 265–272.

(55) Mino, L.; Agostino, A.; Codato, S.; Lamberti, C. *J. Anal. At. Spectrom.* **2010**, *25*, 831–836.

(56) Sharanabasappa; Kerur, B. R.; Anilkumar, S.; Hanumaiah, B. *Appl. Radiat. Isot.* **2010**, *68*, 76–83.

(57) Radtke, M.; Vincze, L.; Gorner, W. *J. Anal. At. Spectrom.* **2010**, *25*, 631–634.

(58) Hodoroaba, V.-D.; Radtke, M.; Vincze, L.; Rackwitz, V.; Reuter, D. *Nucl. Instrum. Methods Phys. Res., Sect. B* **2010**, *268*, 3568–3575.

(59) Taylor, S. M.; Andrushenko, S. M.; O'Meara, J. M.; Campbell, J. L. *X-ray Spectrom.* **2010**, *39*, 191–201.

(60) Taborda, A.; Chaves, P. C.; Reis, M. A. *Nucl. Instrum. Methods Phys. Res., Sect. B* **2010**, *268*, 1802–1805.

(61) Bertucci, M.; Bonizzoni, L.; Ludwig, N.; Milazzo, M. *X-ray Spectrom.* **2010**, *39*, 135–141.

(62) Sasaki, N.; Okada, K.; Kawai, J. *X-ray Spectrom.* **2010**, *39*, 328–331.

(63) Ogawa, R.; Ochi, H.; Nishino, M.; Ichimaru, N.; Yamato, R. *X-ray Spectrom.* **2010**, *39*, 399–406.

(64) Camarillo-Ravelo, D.; Kaftandjian, V.; Duvauchelle, P. *X-ray Spectrom.* **2010**, *39*, 391–398.

(65) Smolek, S.; Streli, C.; Zoeger, N.; Wobrauschek, P. *Rev. Sci. Instrum.* **2010**, *81*, 053707.

(66) Matsuyama, S.; Shimura, M.; Fujii, M.; Maeshima, K.; Yumoto, H.; Mimura, H.; Sano, Y.; Yabashi, M.; Nishino, Y.; Tamasaku, K.; Ishizaka, Y.; Ishikawa, T.; Yamauchi, K. *X-ray Spectrom.* **2010**, *39*, 260–266.

(67) Alfeld, M.; Janssens, K.; Dik, J.; de Nolf, W.; van der Snickt, G. *J. Anal. At. Spectrom.* **2011**, *26*, 899–909.

(68) Yonehara, T.; Orita, D.; Nakano, K.; Komatani, S.; Ohzawa, S.; Bando, A.; Uchihara, H.; Tsuji, K. *X-ray Spectrom.* **2010**, *39*, 78–82.

(69) Tsuji, K.; Nakano, K. *J. Anal. At. Spectrom.* **2011**, *26*, 305–309.

(70) Wilke, M.; Appel, K.; Vincze, L.; Schmidt, C.; Borchert, M.; Pascarelli, S. *J. Synchrotron Radiat.* **2010**, *17*, 669–675.

(71) De Samber, B.; Silversmit, G.; De Schamphelaere, K.; Evens, R.; Schoonjans, T.; Vekemans, B.; Janssen, C.; Masschaele, B.; Van Hoorebeke, L.; Szalóki, I.; Vanhaecke, F.; Rickers, K.; Falkenberg, G.; Vincze, L. *J. Anal. At. Spectrom.* **2010**, *25*, 544–553.

(72) Patterson, B. M.; Campbell, J.; Havrilla, G. J. *X-ray Spectrom.* **2010**, *39*, 184–190.

(73) Pereira, G. R.; Rocha, H. S.; Calza, C.; Anjos, M. J.; Lima, I.; Pérez, C. A.; Lopes, R. T. *X-ray Spectrom.* **2011**, *40*, 260–264.

(74) Tsuji, K.; Ohmori, T.; Yamaguchi, M. *Anal. Chem.* **2011**, *83*, 6389–6394.
(75) Yonehara, T.; Yamaguchi, M.; Tsuji, K. *Spectrochim. Acta, Part B* **2010**, *65*, 441–444.
(76) Takeuchi, A.; Terada, Y.; Uesugi, K.; Suzuki, Y. *Nucl. Instrum. Methods Phys. Res., Sect. A* **2010**, *616*, 261–265.
(77) A Selection of Papers Presented at the 13th Conference on Total Reflection X-ray Fluorescence Analysis and Related Methods (TXRF 2009), *Spectrochim. Acta, Part B* **2010**, *65*, 427−508.
(78) Meirer, F.; Singh, A.; Pepponi, G.; Streli, C.; Homma, T.; Pianetta, P. *Trends Anal. Chem.* **2010**, *29*, 479–496.
(79) Kühn, A.; Scharf, O.; Ordavo, I.; Riesemeier, H.; Reinholz, U.; Radtke, M.; Berger, A.; Ostermann, M.; Panne, U. *J. Anal. At. Spectrom.* **2011**, *26*, 1986–1989.
(80) Horntrich, C.; Smolek, S.; Maderitsch, A.; Simon, R.; Kregsamer, P.; Streli, C. *Anal. Bioanal. Chem.* **2011**, *400*, 2649–2654.
(81) Sparks, C. M.; Fittschen, U. E. A.; Havrilla, G. J. *Spectrochim. Acta, Part B* **2010**, *65*, 805–811.
(82) Hatzistavros, V. S.; Kallithrakas-Kontos, N. G. *Anal. Chem.* **2011**, *83*, 3386–3391.
(83) Takahara, H.; Mori, Y; Shimazaki, A.; Gohshi, Y. *Spectrochim. Acta, Part B* **2010**, *65*, 1022–1028.
(84) Misra, N. L.; Dhara, S.; Óvári, M.; Záray, G.; Aggarwal, S. K.; Varga, I. *Spectrochim. Acta, Part B* **2010**, *65*, 457–460.
(85) Bennun, L.; Sanhueza, V. *Anal. Sci.* **2010**, *26*, 331–335.
(86) Sanchez, H. J.; Perez, R. D.; Carvalho, M. L.; Rubio, M. N *Nucl. Instrum. Methods Phys. Res., Sect. B* **2010**, *268*, 3478–3481.
(87) Egorov, V. K.; Egorov, E. V. *Meas. Tech.* **2010**, *53*, 510–517.
(88) Kunimura, S.; Kawai, J. *Analyst* **2010**, *135*, 1909–1911.
(89) Kunimura, S.; Tee, D, P.; Kawai, J. *Tetsu-to-Hagané* **2011**, *97*, 81–84.
(90) Pepponi, G.; Giubertoni, D.; Bersani, M.; Meirer, F.; Ingerle, D.; Steinhauser, G.; Streli, C.; Hoenicke, P.; Beckhoff, B. *J. Vac. Sci. Technol., B* **2010**, *28*, C1C59–C1C64.
(91) Ingerle, D.; Meirer, F.; Zoeger, N.; Pepponi, G.; Giubertoni, D.; Steinhauser, G.; Wobrauschek, P.; Streli, C. *Spectrochim. Acta, Part B* **2010**, *65*, 429–433.
(92) Streeck, C.; Beckhoff, B.; Reinhardt, F.; Kolbe, M.; Kanngiesser, B.; Kaufmann, C. A.; Schock, H. W. *Nucl. Instrum. Methods Phys. Res., Sect. B* **2010**, *268*, 277–281.
(93) Tiwari, M. K.; Sawhney, K. J. S.; Lodha, G. S. *Spectrochim. Acta, Part B* **2010**, *65*, 434–440.
(94) Tiwari, M. K.; Lodha, G. S.; Sawhney, K. J. S. *X-ray Spectrom.* **2010**, *39*, 127–134.
(95) Kawai, J. *J. Electron Spectrosc. Relat. Phenom.* **2010**, *178−179*, 268–272.
(96) Geng, H.; Kang, S.; Jung, H.-J.; Choel, M.; Kim, H.; Ro, C.-U. *J. Geophys. Res.* **2010**, *115*, D15306.
(97) Hubner, R.; Engelmann, H.-J.; Zschech, E. *Thin Solid Films* **2010**, *519*, 203–209.
(98) Song, Y.-C.; Ryu, J.; Malek, M. A.; Jung, H.-J.; Ro, C.-U. *Anal. Chem.* **2010**, *82*, 7987–7998.
(99) Jung, H.-J.; Malek, M. A.; Ryu, J.; Kim, B.; Song, Y.-C.; Kim, H.; Ro, C.-U. *Anal. Chem.* **2010**, *82*, 6193–6202.
(100) Malek, M. A.; Kim, B.; Jung, H.-J.; Song, Y.-C.; Ro, C.-U. *Anal. Chem.* **2011**, *83*, 7970–7977.
(101) Ahn, K.-H.; Kim, S.-M.; Jung, H.-J.; Lee, M.-J.; Eom, H.-J.; Maskey, S.; Ro, C.-U. *Anal. Chem.* **2010**, *82*, 7999–8009.
(102) Maskey, S.; Choel, M.; Kang, S.; Hwang, H.; Kim, H.; Ro, C.-U. *Anal. Chim. Acta* **2010**, *658*, 120–127.
(103) Merlet, C.; Llovet, X. *X-ray Spectrom.* **2011**, *40*, 47–54.
(104) Horny, P.; Lifshin, E.; Campbell, H.; Gauvin, R. *Microsc. Microanal.* **2010**, *16*, 821–830.
(105) Christien, F.; Pierson, J. F.; Hassini, A.; Capon, F.; Le Gall, R.; Brousse, T. *Appl. Surf. Sci.* **2010**, *256*, 1855–1860.
(106) Donovan, J. J.; Lowers, H. A.; Rusk, B. G. *Am. Mineral.* **2011**, *96*, 274–282.
(107) Thibault, Y.; Pratt, A. R. *Am. Mineral.* **2011**, *96*, 53–59.
(108) Limandri, S. P.; Carreras, A. C.; Trincavelli, J. C. *Microsc. Microanal.* **2010**, *16*, 583–593.
(109) Poirier, D.; Gauvin, R. *Scanning* **2011**, *33*, 126–134.
(110) Kavčič, M. *Nucl. Instrum. Methods Phys. Res., Sect. B* **2010**, *268*, 3438–3442.
(111) Tadić, T.; Božičević, I.; Jakšić, M. *X-ray Spectrom.* **2011**, *40*, 147–152.
(112) Reis, M. A.; Chaves, P. C.; Taborda, A. *X-ray Spectrom.* **2011**, *40*, 141–146.
(113) Grassi, N.; Guazzoni, C.; Alberti, R.; Klatka, T.; Bjeoumikhov, A. *Nucl. Instrum. Methods Phys. Res., Sect. B* **2010**, *268*, 1945–1948.
(114) Žitnik, M.; Grlj, N.; Vaupetič, P.; Pelicon, P.; Bučar, K.; Sokaras, D.; Karydas, A. G.; Kanngiesser, B. *J. Anal. At. Spectrom.* **2010**, *25*, 28–33.
(115) Ohkura, S.; Ishii, K.; Matsuyama, S.; Terakawa, A.; Kikuchi, Y.; Kawamura, Y.; Catella, G.; Hashimoto, Y.; Fujikawa, M.; Hamada, N.; Fujiki, K.; Hatori, E.; Yamazaki, H. *X-ray Spectrom.* **2011**, *40*, 191–193.
(116) Shibata, S.; Kamiyanagi, H.; Okano, T.; Kitamura, A. *IEEE Trans. Semicond. Manuf.* **2010**, *23*, 423–428.
(117) Pichon, L.; Beck, L.; Walter, Ph.; Moignard, B.; Guillou, T. *Nucl. Instrum. Methods Phys. Res., Sect. B* **2010**, *268*, 2028–2033.
(118) Jones, B. N.; Palitsin, V.; Webb, R. *Nucl. Instrum. Methods Phys. Res., Sect. B* **2010**, *268*, 1714–1717.
(119) Bunker, G. *Introduction to XAFS: a practical guide to X-ray absorption fine structure spectroscopy*; Cambridge University Press: Cambridge, UK, 2010.
(120) Lombi, E.; Hettirachchi, G. M.; Scheckel, K. G. *J. Environ. Qual.* **2011**, *40*, 659–666.
(121) van Bokhoven, J. *Phys. Chem. Chem. Phys.* **2010**, *12*, 5502–5502.
(122) Cuenya, B. R. *Thin Solid Films* **2010**, *518*, 3127–3150.
(123) Singh, J.; Lamberti, C.; van Bokhoven, J. A. *Chem. Soc. Rev.* **2010**, *39*, 4754–4766.
(124) Ortega, R. *J. Anal. At. Spectrom.* **2011**, *26*, 23–29.
(125) Rehr, J. J.; Kas, J. J.; Vila, F. D.; Prange, M. P.; Jorissen, K. *Phys. Chem. Chem. Phys.* **2010**, *12*, 5503–5513.
(126) Stavitski, E.; de Groot, F. M. F. *Micron* **2010**, *41*, 687–694.
(127) Johnson, S. L.; Milne, C. J. *TrAC, Trends Anal. Chem.* **2010**, *29*, 497–507.
(128) Ferri, D.; Kumar, M. S.; Wirz, R.; Eyssler, A.; Korsak, O.; Hug, P.; Weidenkaff, A.; Newton, M. A. *Phys. Chem. Chem. Phys.* **2010**, *12*, 5634–5646.
(129) Bauer, M.; Heusel, G.; Mangold, S.; Bertagnolli, H. *J. Synchrotron Radiat.* **2010**, *17*, 273–279.
(130) Silversmit, G.; Vekemans, B.; Appel, K.; Schmitz, S.; Schoonjans, T.; Brenker, F. E.; Kaminsky, F.; Vincze, L. *Anal. Chem.* **2011**, *83*, 6294–6299.
(131) Cotte, M.; Szlachetko, J.; Lahlil, S.; Salomé, M.; Solé, V. A.; Biron, I.; Susini, J. *J. Anal. At. Spectrom.* **2011**, *26*, 1051–1059.
(132) Nelson, G. J.; Harris, W. M.; Izzo, J. R., Jr.; Grew, K. N.; Chiu, W. K. S.; Chu, Y. S.; Yi, J.; Andrews, J. C.; Liu, Y.; Pianetta, P. *Appl. Phys. Lett.* **2011**, *98*, 173109.
(133) Okumura, T.; Nakatsutsumi, T.; Ina, T.; Orikasa, Y.; Arai, H.; Fukutsuka, T; Iriyama, Y.; Uruga, T.; Tanida, H.; Uchimoto, Y.; Ogumi, Z. *J. Mater. Chem.* **2011**, *21*, 10051–10060.
(134) Pagels, M.; Reinhardt, F.; Pollakowski, B.; Roczen, M.; Becker, C.; Lips, K.; Rech, B.; Kanngiesser, B.; Beckhoff, B. *Nucl. Instrum. Methods Phys. Res., Sect. B* **2010**, *268*, 370–373.
(135) Polte, J.; Ahner, T. T.; Delissen, F.; Sokolov, S.; Emmerling, F.; Thünemann, A. F.; Kraehnert, R. *J. Am. Chem. Soc.* **2010**, *132*, 1296–1301.
(136) Fittschen, U. E. A.; Havrilla, G. J. *Anal. Chem.* **2010**, *82*, 297–306.
(137) Yonezawa, S.; Hokura, A.; Matsuda, K.; Kimoto, T.; Nakai, I. *Bunseki Kagaku* **2010**, *59*, 23–33.
(138) Heiden, E. S.; Gore, D. B.; Stark, S. C. *X-ray Spectrom.* **2010**, *39*, 176–183.
(139) Inui, T.; Abe, W.; Kitano, M.; Nakamura, T. *X-ray Spectrom.* **2011**, *40*, 301–305.

(140) Noro, J.; Korenaga, T.; Kozaki, M.; Kawada, S.; Kurusu, K.; Mizuhira, M.; Ono, A.; Katsumi, K.; Kakita, K.; Takimoto, K.; Sakata, M. *Bunseki Kagaku* **2010**, *59*, 107–116.
(141) Patterson, B. M.; Hamilton, C. E. *Anal. Chem.* **2010**, *82*, 8537–8543.
(142) Buzanich, G.; Wobrauschek, P.; Streli, C.; Markowicz, A.; Wegrzynek, D.; Chinea-Cano, E.; Griesser, M.; Uhlir, K. *X-ray Spectrom.* **2010**, *39*, 98–102.
(143) Migliori, A.; Bonanni, P.; Carraresi, L.; Grassi, N.; Mandò, P. A. *X-ray Spectrom.* **2011**, *40*, 107–112.
(144) Guilherme, A.; Pessanha, S.; Carvalho, M. L.; dos Santos, J. M. F.; Coroado, J. *Spectrochim. Acta B* **2010**, *65*, 328–333.
(145) Van der Snickt, G.; Janssens, K.; Schalm, O.; Aibéo, C.; Kloust, H.; Alfeld, M. *X-ray Spectrom.* **2010**, *39*, 103–111.
(146) Grieten, E.; Casadio, F. *X-ray Spectrom.* **2010**, *39*, 221–229.
(147) Roldán, C.; Murcia-Mascarós, S.; Ferrero, J.; Villaverde, V.; López, E.; Domingo, I.; Martíinez, R.; Guillem, P. M. *X-ray Spectrom.* **2010**, *39*, 243–250.
(148) Cesareo, R.; Bustamante, A.; Fabian, J.; Calza, C.; Dos Anjos, M.; Lopes, R. T.; Alva, W.; Chero, L.; Espinoza, M.; Gutierrez, R.; Rodriguez, R.; Seclen, M. *X-ray Spectrom.* **2011**, *40*, 37–46.
(149) Kenna, T. C.; Nitsche, F. O.; Herron, M. M.; Mailloux, B. J.; Peteet, D.; Sritrairat, S.; Sands, E.; Baumgarten, J. *J. Anal. At. Spectrom.* **2011**, *26*, 395–405.
(150) Bonizzoni, L.; Colombo, C.; Ferrati, S.; Gargano, M.; Greco, M.; Ludwig, N.; Realini, M. *X-ray Spectrom.* **2011**, *40*, 247–253.
(151) Chou, J.; Clement, G.; Bursavich, B.; Elbers, D.; Cao, B.; Zhou, W. *Environ. Pollut.* **2010**, *158*, 2230–2234.
(152) Figi, R.; Nagel, O.; Tuchschmid, M.; Lienemann, P.; Gfeller, U.; Bukowiecki, N. *Anal. Chim. Acta* **2010**, *676*, 46–52.
(153) Nie, L. H.; Sanchez, S.; Newton, K.; Grodzins, L.; Cleveland, R. O.; Weisskopf, M. G. *Phys. Med. Biol.* **2011**, *56*, N39–N51.
(154) Alshehabi, A.; Kunimura, S.; Kawai, J. *Anal. Methods* **2010**, *2*, 1555–1558.
(155) Janssens, K.; Dik, J.; Cotte, M.; Susini., J. *Acc. Chem. Res.* **2010**, *43*, 814–825.
(156) Monico, L.; Van der Snickt, G.; Janssens, K.; De Nolf, W.; Miliani, C.; Verbeeck, J.; Tian, H.; Tan, H.; Dik, J.; Radepont, M.; Cotte, M. *Anal. Chem.* **2011**, *83*, 1214–1223.
(157) Monico, L.; Van der Snickt, G.; Janssens, K.; De Nolf, W.; Miliani, C.; Dik, J.; Radepont, M.; Hendriks, E.; Geldof, M.; Cotte, M. *Anal. Chem.* **2011**, *83*, 1224–1231.
(158) Yamaoka, W.; Takada, S.; Takehisa, H.; Hayashi, Y.; Hokura, A.; Terada, Y.; Abe, T.; Nakai, I. *Bunseki Kagaku* **2010**, *59*, 463–475.
(159) Harada, E.; Hokura, A; Takada, S.; Baba, K.; Terada, Y.; Nakai, I.; Yazaki, K. *Plant Cell Physiol.* **2010**, *51*, 848–853.
(160) Pinakidou, F.; Katsikini, M.; Paloura, E. C.; Vourlias, G.; Stergouidis, G. *Nucl. Instrum. Methods Phys. Res., Sect. B* **2010**, *268*, 356–360.
(161) Genna, D.; Gaboury, D.; Moore, L.; Muellera, W. U. *J. Geochem. Explor.* **2011**, *108*, 131–142.
(162) Nakano, K.; Nishi, C.; Otsuki, K.; Nishiwaki, Y.; Tsuji, K. *Anal. Chem.* **2011**, *83*, 3477–3483.
(163) Mantouvalou, I.; Lange, K.; Wolff, T.; Grötzsch, D.; Lühl, L.; Haschke, M.; Hahn, O.; Kanngießer, B. *J. Anal. At. Spectrom.* **2010**, *25*, 554–561.
(164) Mihucz, V. G.; Silversmit, G.; Szalóki, I.; de Samber, B.; Schoonjans, T.; Tatár, E.; Vincze, L.; Virág, I.; Yao, J.; Záray, G. *Food Chem.* **2010**, *121*, 290–297.
(165) Patterson, B. M.; Obrey, K. A.; Havrilla, G. J. *Fusion Sci. Technol.* **2011**, *59*, 121–125.
(166) Perez, R. D.; Sánchez, H. J.; Rubio, M.; Perez, C. A. *X-ray Spectrom.* **2011**, *40*, 19–23.
(167) Perez, R. D.; Sánchez, H. J.; Perez, C. A.; Rubio, M. *Radiat. Phys. Chem.* **2010**, *79*, 195–200.
(168) Fernández-Ruiz, R.; Malki, M.; Morato, A. I.; Marin, I. *J. Anal. At. Spectrom.* **2011**, *26*, 511–516.
(169) Marguí, E.; Kregsamer, P.; Hidalgo, M.; Tapias, J.; Queralt, I.; Streli, C. *Talanta* **2010**, *82*, 821–827.
(170) Marguí, E.; Floor, G. H.; Hidalgo, M.; Kregsamer, P.; Roman-Ross, G.; Streli, C.; Queralt, I. *Spectrochim. Acta, Part B* **2010**, *65*, 1002–1007.
(171) Espinoza-Quiñones, F. R.; Palácio, S. M.; Módenes, A. N.; Szymanski, N.; Zacarkim, C. E.; Zenatti, D. C.; Fornari, M. M. T.; Rizzutto, M. A.; Tabacniks, M. H.; Added, N.; Kroumov, A. D. *J. Radioanal. Nucl. Chem.* **2010**, *283*, 465–470.
(172) Tavares, G. A.; Almeida, E.; de Oliveira, J. G. G.; Bendassolli, J. A.; Nascimento Filho, V. F. *J. Radioanal. Nucl. Chem.* **2011**, *287*, 377–381.
(173) Barros, H.; Marcó Parra, L.-M.; Bennun, L.; Greaves, E. D. *Spectrochim. Acta, Part B* **2010**, *65*, 489–492.
(174) Pessanha, S.; Carvalho, M. L.; Becker, M.; von Bohlen, A. *Spectrochim. Acta, Part B* **2010**, *65*, 504–507.
(175) Cinosi, A.; Andriollo, N.; Pepponi, G.; Monticelli, D. *Anal. Bioanal. Chem.* **2011**, *399*, 927–933.
(176) Kawamata, M.; Imanishi, Y.; Nakano, K.; Tsuji, K. *Adv. X-ray Chem. Anal., Japan* **2010**, *41*, 185–193.
(177) Amberger, M. A.; Höltig, M.; Broekaert, J. A. C. *Spectrochim. Acta, Part B* **2010**, *65*, 152–157.
(178) Fernández-Ruiz, R.; Andrés, R.; de Jesús, E.; Terreros, P. *Spectrochim. Acta, Part B* **2010**, *65*, 450–456.
(179) Bontempi, E.; Zacco, A.; Benedetti, D.; Borgese, L.; Colombi, P.; Stosnach, H.; Finzi, G.; Apostoli, P.; Buttini, P.; Depero, L. E. *Environ. Technol.* **2010**, *31*, 467–477.
(180) Marguí, E.; Floor, G. H.; Hidalgo, M.; Kregsamer, P.; Román-Ross, G.; Streli, C.; Queralt, I. *Anal. Chem.* **2010**, *82*, 7744–7751.
(181) Shapovalov, V. L.; Dittrich, M.; Konovalov, O. V.; Brezesinski, G. *Langmuir* **2010**, *26*, 14766–14773.
(182) Magalhaes, T.; Carvalho, M. L.; Von Bohlen, A.; Becker, M. *Spectrochim. Acta, Part B* **2010**, *65*, 493–498.
(183) Borgese, L.; Zacco, A.; Bontempi, E.; Pellegatta, M.; Vigna, L.; Patrini, L.; Riboldi, L.; Rubino, F. M.; Depero, L. E. *J. Pharm. Biomed. Anal.* **2010**, *52*, 787–790.
(184) Abraham, J. A.; Sánchez, H. J.; Valentinuzzi, M. C.; Grenón, M. S. *X-ray Spectrom.* **2010**, *39*, 372–375.
(185) Espinoza-Quiñones, F. R.; Módenes, A. N.; Palácio, S. M.; Szymanski, N.; Welter, R. A.; Rizzutto, M. A.; Borba, C. E.; Kroumov, A. D. *Appl. Radiat. Isot.* **2010**, *68*, 2202–2207.
(186) Carneiro, C. D.; Mársico, E. T.; de Jesus, E. F. O.; Ribeiro, R. D. R.; Barbosa, R. D. *Chem. Ecol.* **2011**, *27*, 1–8.
(187) Dhara, S.; Misra, N. L.; Maind, S. D.; Kumar, S. A.; Chattopadhyay, N.; Aggarwal, S. K. *Spectrochim. Acta, Part B* **2010**, *65*, 167–170.
(188) Geng, H.; Ryu, J.; Jung, H.-J.; Chung, H.; Ahn, K.-H.; Ro, C.-U. *Environ. Sci. Technol.* **2010**, *44*, 2348–2353.
(189) Maskey, S.; Geng, H.; Song, Y.-C.; Hwang, H.; Yoon, Y.-J.; Ahn, K.-H.; Ro, C.-U. *Environ. Sci. Technol.* **2011**, *45*, 6275–6282.
(190) Geng, H.; Ryu, J.; Maskey, S.; Jung, H.-J.; Ro, C.-U. *Atmos. Chem. Phys.* **2011**, *11*, 1327–1337.
(191) Maskey, S.; Kang, T.; Jung, H.-J.; Ro, C.-U. *Indoor Air* **2011**, *21*, 12–24.
(192) Jung, H.-J.; Kim, B.; Ryu, J.; Maskey, S.; Kim, J.-C.; Sohn, J.; Ro, C.-U. *Atmos. Environ.* **2010**, *44*, 2287–2293.
(193) Slezakova, K.; Pires, J. C. M.; Martins, F. G.; Pereira, M. C.; Alvim-Ferraz, M. C. *Atmos. Environ.* **2011**, *45*, 863–872.
(194) Matassoni, L.; Pratesi, G.; Centioli, D.; Cadoni, F.; Lucarelli, F.; Nava, S.; Malesani, P. *J. Environ. Monit.* **2011**, *13*, 732–742.
(195) Weinbruch, S.; Ebert, M.; Gorzawski, H.; Dirsch, T.; Berg, T.; Steinnes, E. *J. Environ. Monit.* **2010**, *12*, 1064–1071.
(196) Vega, A.; Fiuza, A.; Guimaraes, F. *Langmuir* **2010**, *26*, 11980–11986.
(197) Nakai, I.; Ono, Y.; Li, Q.; Nishiwaki, Y.; Tanaka, K.; Nakayama, S. *Surf. Interface Anal.* **2010**, *42*, 402–410.
(198) Rinaudo, C.; Allegrina, M.; Fornero, E.; Musa, M.; Croce, A.; Bellis, D. *J. Raman Spectrosc.* **2010**, *41*, 27–32.

(199) Sanislav, I. V. *J. Metamorph. Geol.* **2011**, *29*, 251–273.
(200) Just, J.; Schulz, B.; de Wall, H.; Jourdan, F.; Pandit, M. K. *Gondwana Res.* **2011**, *19*, 402–412.
(201) Lucarelli, F.; Nava, S.; Calzolai, G.; Chiari, M.; Udisti, R.; Marino, F. *X-ray Spectrom.* **2011**, *40*, 162–167.
(202) Waheed, A.; Zhang, Y.; Bao, L.; Cao, Q.; Zhang, G.; Li, Y.; Li, X. *J. Radioanal. Nucl. Chem.* **2010**, *283*, 427–432.
(203) Tanaka, N.; Kimura, H.; Faried, A.; Sakai, M.; Sano, A.; Inose, T.; Sohda, M.; Okada, K.; Nakajima, M.; Miyazaki, T.; Fukuchi, M.; Kato, H.; Asao, T.; Kuwano, H.; Satoh, T.; Oikawa, M.; Kamiya, T.; Arakawa, K. *Cancer Sci.* **2010**, *101*, 1487–1492.
(204) Matsuzaki, S.; Shimizu, Y.; Dobashi, K.; Nagamine, T.; Satoh, T.; Ohkubo, T.; Yokoyama, A.; Ishii, Y.; Kamiya, T.; Arakawa, K.; Makino, S.; Utsugi, M.; Ishizuka, T.; Tanaka, S.; Shimizu, K.; Mori, M. *Int. J. Immunopathol. Pharmacol.* **2010**, *23*, 1–11.
(205) Alatise, O. I.; Obiajunwa, E. I.; Lawal, O. O.; Adesunkanmi, A. R. K. *Biol. Trace Elem. Res.* **2010**, *134*, 13–24.
(206) Preoteasa, E. A.; Preoteasa, E.; Harangus, L.; Moldovan, A.; Dinescu, M.; Grambole, D.; Herrmann, F. *X-ray Spectrom.* **2010**, *39*, 208–215.
(207) Rautray, T. R.; Das, S.; Rautray, A. C. *Nucl. Instrum. Methods Phys. Res., Sect. B* **2010**, *268*, 2371–2374.
(208) Pongrac, P.; Vogel-Mikuš, K.; Regvar, M.; Vavpetič, P.; Pelicon, P.; Kreft, I. *J. Agric. Food Chem.* **2011**, *59*, 1275–1280.
(209) dos Santos, C. E. I.; da Silva, L. R. M.; Boufleur, L. A.; Debastiani, R.; Stefenon, C. A.; Amaral, L.; Yoneama, M. L.; Dias, J. F. *Food Chem.* **2010**, *121*, 244–250.
(210) Mesjasz-Przybyłowicz, J.; Przybyłowicz, W. J. *X-ray Spectrom.* **2011**, *40*, 181–185.
(211) Gramigni, E.; Calusi, S.; Chelazzi, G.; Del Greco, F.; Delfino, G.; Gelli, N.; Giuntini, L.; Massi, M.; Santini, G. *X-ray Spectrom.* **2011**, *40*, 186–190.
(212) Zheng, Y.; Guo, H.; Wei, K.; Tang, W.; Satoh, T.; Ohkubo, T.; Yamazaki, A.; Takano, K.; Kamiya, T.; Shen, H.; Yang, M.; Mi, Y. *Nucl. Instrum. Methods Phys. Res., Sect. B* **2010**, *268*, 2152–2155.
(213) Bobée, C.; Huon, S.; Guendon, J.-L.; Salomon, J.; Gébara, C.; Michel, J.-M.; Regert, M. *Archaeometry* **2011**, *53*, 241–260.
(214) Dupuis, T.; Chene, G.; Mathis, F.; Marchal, A.; Philippe, M.; Garnir, H.-P.; Strivay, D. *Nucl. Instrum. Methods Phys. Res., Sect. B* **2010**, *268*, 1911–1915.
(215) Roumie, M.; Nsouli, B.; Chalhoub, G.; Hamdan, M. *Nucl. Instrum. Methods Phys. Res., Sect. B* **2010**, *268*, 1916–1919.
(216) DeYoung, P. A.; Hall, C. C.; Mears, P. J.; Padilla, D. J.; Sampson, R.; Peaslee, G. F. *J. Forensic Sci.* **2011**, *56*, 366–371.
(217) Jezeršek, D.; Jakomin, S.; Šmit, Ž. *Surf. Interface Anal.* **2010**, *42*, 423–428.
(218) Cabaret, D.; Bordage, A.; Juhin, A.; Arfaoui, M.; Gaudry, E. *Phys. Chem. Chem. Phys.* **2010**, *12*, 5619–5633.
(219) van der Laan, G.; Chopdekar, R. V.; Suzuki, Y.; Arenholz, E. *Phys. Rev. Lett.* **2010**, *105*, 067405.
(220) Mančić, A.; Lévy, A.; Harmand, M.; Nakatsutsumi, M.; Antici, P.; Audebert, P.; Combis, P.; Fourmaux, S.; Mazevet, S.; Peyrusse, O.; Recoules, V.; Renaudin, P.; Robiche, J.; Dorchies, F.; Fuchs, J. *Phys. Rev. Lett.* **2010**, *104*, 035002.
(221) Nishi, T.; Nakada, M.; Suzuki, C.; Shibata, H.; Itoh, A.; Akabori, M.; Hirata, M. *J. Nucl. Mater.* **2010**, *401*, 138–142.
(222) Galbis, E.; Hernández-Cobos, J.; den Auwer, C.; Le Naour, C.; Guillaumont, D.; Simoni, E.; Pappalardo, R. R.; Marcos, E. S. *Angew. Chem., Int. Ed.* **2010**, *49*, 3811–3815.
(223) Masciocchi, N.; Galli, S.; Colombo, V.; Maspero, A.; Palmisano, G.; Seyyedi, B.; Lamberti, C.; Bordiga, S. *J. Am. Chem. Soc.* **2010**, *132*, 7902–7904.
(224) Watts, B.; McNeill, C. R. *Macromol. Rapid Commun.* **2010**, *31*, 1706–1712.
(225) Finney, L.; Chishti, Y.; Khare, T.; Giometti, C.; Levina, A.; Lay, P. A.; Vogt, S. *ACS Chem. Biol.* **2010**, *5*, 577–587.
(226) Kashiwabara, T.; Takahashi, Y.; Tanimizu, M.; Usui, A. *Geochim. Cosmochim. Acta* **2011**, *75*, 5762–5784.
(227) Hocking, R. K.; Brimblecombe, R.; Chang, L.-Y.; Singh, A.; Cheah, M. H.; Glover, C.; Casey, W. H.; Spiccia, L. *Nat. Chem.* **2011**, *3*, 461–466.
(228) Nakazawa, E.; Ikemoto, T.; Hokura, A.; Terada, Y.; Kunito, T.; Tanabe, S.; Nakai, I. *Metallomics* **2011**, *3*, 719–725.
(229) Furukawa, T.; Takahashi, Y. *Atmos. Chem. Phys.* **2011**, *11*, 4289–4301.